CISLUNAR MISSION DESIGN: TRANSFERS LINKING NEAR RECTILINEAR HALO ORBITS AND THE BUTTERFLY FAMILY

A Thesis

Submitted to the Faculty

of

Purdue University

by

Matthew J. Bolliger

In Partial Fulfillment of the

Requirements for the Degree

of

Master of Science in Aeronautics and Astronautics

August 2019

Purdue University

West Lafayette, Indiana

THE PURDUE UNIVERSITY GRADUATE SCHOOL
STATEMENT OF THESIS APPROVAL

Professor Kathleen C. Howell, Chair

School of Aeronautics and Astronautics

Professor Carolin Frueh

School of Aeronautics and Astronautics

Professor David A. Spencer

School of Aeronautics and Astronautics

Approved by:

Professor Weinong Chen

Aeronautics and Astronautics Associate Head for Graduate Education

ACKNOWLEDGMENTS

If the measure of one's worth is the quality if one's company, I have unwittingly become the richest person in the world. Croesus himself would be jealous. I owe so much to my friends, family, peers, and advisors that I could probably write more pages thanking them for their support than the number of pages I have written for this very document. Instead, though, I will keep it brief.

First, I would like to thank my advisor, Professor Kathleen C. Howell. Without her support and guidance, this work would not have been possible. I feel so lucky to have had the opportunity to learn from someone who is so dedicated to the field and to the university. I would also like to thank my committee members, Professor Carolin Frueh and Professor David Spencer. In addition to their advice and feedback, I have had the pleasure of taking exciting and rewarding courses with each of them throughout my undergraduate and graduate education here at Purdue.

Next, I would like to thank everyone in the Multi-Body Dynamics Research Group. It is an exceptional treasure to have been surrounded by peers who are so brilliant and so intelligent, yet so easy to get along with. They have offered me not only extraordinary guidance and advice throughout the course of my research, but also their friendship, which is even more valuable. I would also like to give a special shout-out to one of my best friends while here at Purdue, Sebastian Tamrazian, who has been a partner in commiseration ever since our sophomore year.

And finally, I owe the largest debt to my family. I could not have completed any of my degrees without their loving support. From the beginning, my family has supported all of my fascinations—no matter how brief—giving me endless opportunities to learn and grow. So; to my mom, Nancy; my dad, Brian; my brother, Brad; and my Aunt Pat, thank you all. This work exists because of you.

TABLE OF CONTENTS

Page

LIST OF TABLES

LIST OF FIGURES

Figure Page

Figure Page

Figure Page

ABSTRACT

Bolliger, Matthew J. M.S. AAE, Purdue University, August 2019. Cislunar Mission Design: Transfers Linking Near Rectilinear Halo Orbits and the Butterfly Family. Major Professor: Kathleen C. Howell.

An integral part of NASA's vision for the coming years is a sustained infrastructure in cislunar space. The current baseline trajectory for this facility is a Near Rectilinear Halo Orbit (NRHO), a periodic orbit in the Circular Restricted Three-Body Problem. One of the goals of the facility is to serve as a proving ground for human spaceflight operations in deep space. Thus, this investigation focuses on transfers between the baseline NRHO and a family of periodic orbits that originate from a period-doubling bifurcation along the halo family. This new family of orbits has been termed the "butterfly" family. This investigation also provides an overview of the evolution for a large subset of the butterfly family. Transfers to multiple subsets of the family are found by leveraging different design strategies and techniques from dynamical systems theory. The different design strategies are discussed in detail, and the transfers to each of these regions are compared in terms of propellant costs and times of flight.

1. INTRODUCTION

The foundation of NASA's vision for the coming years—as outlined in the 2018 strategic plan—places renewed emphasis on commercial, governmental, and international missions to the Moon, with the intent that the lunar vicinity may facilitate human exploration and habitation of the Moon's surface, increased access to and knowledge of Mars, and missions to other destinations [1]. An integral part of this vision is a sustained infrastructure in cislunar space, many versions of which have been investigated in recent years.[1] The proposed facility includes modules for human habitation and science operations, with the current baseline trajectory being a Near Rectilinear Halo Orbit (NRHO) [3]. Near Rectilinear Halo Orbits are multi-body orbits near the Moon that offer advantageous properties with regard to eclipsing, stability, communications, operations, and science opportunities [4–6]. In addition to these desirable qualities, NRHOs facilitate access to regions near the Moon, the lunar surface, and deep space.

Halo orbits are members of a continuous family of three-dimensional, periodic libration point orbits that exist in the Circular Restricted Three-Body Problem (CRTBP). Near Rectilinear Halo Orbits are defined as a subset of the more extensive family of halo orbits. In general, trajectories in the CRTBP offer unique opportunities for space mission design that are not available within the context of the two-body (Keplerian) model; properties of NRHOs represent some of the qualities that are most significant to mission designers, especially with respect to a long-term cislunar infrastructure. With NRHOs serving a central role in the planned facility, options for transfers to various types of destinations are critical for mission design.

[1]The current manifestation is the Lunar Orbital Platform-Gateway, which was previously known as the Deep Space Gateway. Similar infrastructures from earlier years were the Exploration Gateway Platform and the Deep Space Habitat [2].

A family of period-doubling orbits that bifurcate from the three-dimensional halo family has emerged as one such destination of interest. This period-doubling family is more frequently termed the "butterfly" family [7]. Given the nature of this bifurcation, the periods of butterfly orbits near the bifurcation are approximately double that of corresponding NRHOs. Consistent with the geometry of NRHOs, the butterflies possess brief, close passages of the Moon, with most of their range extending to high altitudes; butterflies also demonstrate similar stability behavior in the vicinity of NRHOs. However, concomitant with their periods being roughly twice the halo orbit periods, a unique geometrical characteristic of members of the butterfly family is a pair of distinct lobes on either side of the Moon (the Earth-facing side and the anti-Earth-facing side). As the family evolves, so does this lobe structure. Such geometry creates interesting opportunities for mission design.

1.1 Historical Development

The CRTBP has been investigated by some of the world's most accomplished mathematicians and astronomers since the eighteenth century. With interest in the problem seeing a considerable resurgence in recent years, the body of research involving these innovative concepts has grown, as have the applications that exploit the unique properties of trajectories in the CRTBP. As such, the scientific community's understanding of the underlying dynamics, which govern the motion of many phenomena in the universe, has increased significantly.

Although astronomy is one of the oldest natural sciences, the pedigree of modern celestial mechanics only dates back as far as 1687 to Isaac Newton's *Principia*, the first work to characterize the motion of celestial bodies in terms of the same physical laws as the motion of objects on the surface of the Earth (for example, apples) [8]. In the following years, many advancements in the field were motivated by applications for celestial navigation; accurate navigation requires precise measurement and prediction of the locations of the Sun, the Earth, and the Moon. To correctly and

completely model such motion, the effects of every body in the solar system (and more) must be incorporated. This task, solving for the motion of any number of bodies subject to their mutual gravitational attraction, is commonly known as the n-body problem. It is impossible to solve the full n-body problem by means of known analytical equations, but, by introducing simplifying assumptions, it is possible to deliver significant progress in understanding the underlying dynamics.

The most ubiquitous of such simplifying formulations is the two-body problem, that is, the motion of two gravitational bodies subject to their mutual attraction. This problem is solvable under Kepler's laws of planetary motion, and the resulting orbits are simple conic sections. The two-body approach produces useful solutions for many applications; the motion of a planet-moon system is often accurately represented by such a model, and most space mission designs use Keplerian orbits as a baseline solution. Despite the practicality of two-body solutions, however, it is beneficial to include the effects of additional gravitational bodies to produce more accurate results and to investigate new types of motion. The simplest step is to move from a two-body model to a three-body model, but the addition of just one body results in an analytically unsolvable set of equations. Three-body systems are common in the universe, though, so great effort has been expended to aid in their understanding despite the lack of analytical solutions.

Some of the most famous and groundbreaking contributions in the three-body problem originated with Leonhard Euler and Joseph-Louis Lagrange in 1772. In particular, two steps from Euler and Lagrange delivered significant progress:

- Reformulation of the problem into a rotating coordinate frame, and
- The search for particular solutions.

Euler published the first formulation of the restricted three-body problem in a rotating coordinate system, and, further analysis, led by Joseph-Louis Lagrange, described a series of simplifications to reduce the order of the problem. Although the problem remains unsolvable analytically, the lower dimension presented by the new formulation

offers insights that are critical to further developments. The particular solutions deduced by Euler and Lagrange are some of the most well-known features of the CRTBP. The solutions are now labelled the Lagrange points, or libration points. The solutions determined by Euler include the three collinear libration points (L_1, L_2, and L_3), and those identified by Lagrange include the two points corresponding to equilateral triangles (L_4, L_5) [9, 10]. The regions of space surrounding libration points are rich with many forms of complex motion, and they remain essential to understanding the natural dynamics accompanying the problem.

A significant contribution to the problem was delivered in 1836 by Carl Gustav Jacob Jacobi, who introduced an integral of the motion in the rotating frame (now termed the Jacobi constant) [11]. The implications of the Jacobi constant are far-reaching, but one particular use of the constant was leveraged to great effect by George William Hill with his work on zero-velocity curves. Zero-velocity curves are dynamical structures that offer useful insight for analysis in the CRTBP by bounding the regions of possible motion for an object that is comparatively small in relation to two large bodies. Hill demonstrated that such structures, applied to the Sun-Earth-Moon system, prevented the Moon from ever escaping the vicinity of the Earth [12]. Following these contributions, some of the most influential work on the problem of three bodies originates with Henri Poincaré in the late 1800s [13]. His research in support of the CRTBP is part of the foundation of modern dynamical systems theory. Poincaré's analysis of motion in the CRTBP necessitated qualitative developments that, in the opinion of Victor Szebehely, are equal in importance to Euler's computational accomplishments in lunar theory [14]. Poincaré's emphasis on ordered, periodic motion was the basis for further analysis by George Darwin, whose paper in 1897 was the first to include a systematic, computational search for such orbits [15]. Poincaré also introduced the concept of a "surface of section," to reduce the complexity of the problem and offer insight on subsequent behavior. The search for periodic motion was the impetus for many of the developments now used to support analysis in dynamical systems theory; such developments are vital components of this work.

1.2 Previous Contributions

The focus of this investigation is on mission design capabilities in cislunar space—a rich region of space for both past and present studies. Many authors have published works exploring the useful properties of three-body orbits, especially in the Earth-Moon system. Significant contributions over the last few decades have served to elucidate the analytical foundations now exploited for applications in cislunar space.

1.2.1 Near Rectilinear Halo Orbits in Cislunar Space

The term "halo" orbit was first introduced in literature by Farquhar (1968) to describe a family of motion he was investigating for lunar communications [16]. In 1979, Breakwell and Brown demonstrated the existence of related families of solutions in the vicinity of L_1 and L_2 [17]. Notably, stable orbits emerge in all three families. Howell and Breakwell published linear approximations for "almsot rectilinear halo orbits" existing in all three families [18]. They also described a linear analysis to assess the orbits' stability. These "almost rectilinear halo orbits" are now labelled Near Rectilinear Halo Orbits [4]. Near Rectilinear Halo Orbits are emerging as a recognizable example of multi-body orbits; the body of analysis supporting their understanding has expanded to become quite rich. More recently, as detailed in her M.S. thesis, Zimovan describes the suitability of NRHOs for long-term use as a facility near the Moon in cislunar space [19]; such a hub supports a wide range of activities and is expected to include a crewed habitat. Zimovan's work details transitioning NRHOs from the CRTBP to the ephemeris model and characterizes the resultant behavior: some NRHOs are more likely than others to maintain motion similar to their CRTBP complement. She also explores some of the favorable eclipsing behavior that arises from orbits whose periods are in lunar synodic resonance, where the period of the orbit and the synodic period of the Moon are an integer ratio; some resonances avoid Earth and Moon shadowing for a significant interval of time. Finally, she offers sample transfers using two different strategies. Transfers originating from NRHOs

and delivering a spacecraft to other destinations demonstrate good agreement with work from previous authors [20]. Overall, her analysis supports NRHOs as a suitable candidate for staging orbits.

Many authors have published results expanding on those of Zimovan, as well as supporting analysis of other aspects of a cislunar facility. In 2015, Whitley and Martinez published a comparison of staging orbits to support a cislunar habitat, concluding that NRHOs were the most favorable [6]. In addition to Zimovan's analysis, Guzzetti et al. and Davis et al. analyze NRHO station-keeping [21,22], demonstrating that multiple algorithms that leverage dynamical systems theory supply relatively low maneuver costs and robust station-keeping capabilities, which is essential for long-term stays in NRHOs. Whitely et al. explore transfers to NRHOs from the Earth, as well transfers from NRHOs to the lunar surface (they also examine some members of the butterfly family) [23]. They explore both short and long time of flight Earth-to-NRHO transfers. The shorter transfers benefit crewed missions and allow for abort scenarios, while the long time of flight transfers are typically much cheaper in terms of propellant. They demosntrate similar analysis for short and long time of flight transfers to the lunar surface. Their work on the long time of flight transfers builds on extensive work by Parker, specifically his ballistic lunar transfers [24–26]. Not investigated in this work, but important to the understanding of NRHOs for long-term habitation, is disposal of spent stages or human waste. Work from Boudad investigates disposal dynamics in the Bicircular Restricted Four-Body Problem [27]. Conference proceedings from Boudad et al. and Davis et al. expand on this analysis [28, 29]. These works are integral to the understanding of NRHOs as a suitable home for future missions.

1.2.2 Butterfly Orbits

Butterfly orbits are gaining interest for various applications, due, in part, to their stability characteristics in some regions, as well as their eclipsing characteristics. The

butterfly family has not been examined quite as extensively as the halo family, but there exists a useful body of existing work. Early examples of the family exist from the 1970s: Robin and Markellos, in their 1979 paper exploring three-dimensional bifurcations of families in the CR3BP, include butterfly motion in the Sun-Jupiter system [30]. A 2008 paper by Grebow et al. investigates lunar south pole coverage [31]. A number of different orbits are examined in the CRTBP and the ephemeris model, each of which is a member of either the halo family, the vertical family, or the butterfly family. One conclusion asserts that two phased spacecraft ensure adequate coverage of the lunar south pole, and a preliminary station-keeping analysis is also completed. In 2017, Davis et al. [21] examine station-keeping and transfer costs for L_2 southern butterfly orbits. They show that the station-keeping strategies used for NRHOs are also effective for butterflies. They also employ periapse Poincaré maps to generate initial guesses for NRHO-to-butterfly transfers (as well as NRHO-to-halo transfers). The NRHO-to-butterfly transfers in Davis et al. [21] are recreated in the present work, delivering good agreement between results. Whitley et al., similar to their analysis of Earth-to-NRHO and NRHO-to-lunar-surface transfers, explore Earth-to-butterfly and butterfly-to-lunar-surface transfers [23]. Among the orbits examined, the Earth-to-butterfly transfers are similar to Earth-to-NRHO transfers, with the exception that the butterflies offered more entry and exit geometries because of their two lobes. Further, the authors determine that propellant costs to access polar and equatorial lunar landing sites are lower for butterflies than for NRHOs.

1.3 Overview of This work

The underlying goal of this work is in support of renewed interest in cislunar space. To that end, this work details the evolution of the butterfly family itself in the Earth-Moon system, as well as multi-body orbit design strategies linking the family with NRHOs. The document is organized as follows:

- Chapter 2: The rotating reference frame is introduced, as well as the nondimensionalization of system parameters. The equations of motion are derived in nondimensional form and an integral of the motion if introduced (the Jacobi integral). The five equilibrium points are identified. To further inform potential motion, zero-velocity curves and surfaces are developed.

- Chapter 3: This chapter introduces the State Transition Matrix (STM) and the differential corrections process, which are vital tools used for the construction of orbits and transfers in the CRTBP. Continuation schemes are also detailed, as they are closely linked with differential corrections and are important for analysis used later in this work.

- Chapter 4: Concepts from dynamical systems theory are introduced, including periodic orbit stability, invariant manifolds, Poincaré maps, and bifurcation theory. Multiple definitions of stability are developed to aid in orbit characterization and selection.

- Chapter 5: The halo and butterfly families are introduced. The subset of halo orbits known as NRHOs are defined, and the evolution of the butterfly family is investigated with respect to its geometry, stability, and energy.

- Chapter 6: This chapter details the transfer results. Transfers between the halos and the butterflies are examined using multiple design strategies. One-arc, two-arc and manifold-based transfers are explored, as well as transfers returning to the NRHOs from the butterfly family.

- Chapter 7: The results of this work are summarized and areas of future work and recommended.

2. BACKGROUND: CIRCULAR-RESTRICTED THREE-BODY PROBLEM

Edmund T. Whittaker described the three-body problem as the *"most celebrated of all dynamical problems."* [32] The problem is an intriguing mathematical exercise; the dynamics themselves are representative of many phenomena in our solar system—and likely beyond. One of the earliest motivations for examining the problem was the stability of the Sun-Earth-Moon system; investigations frequently assessed the stability of the configuration and the potential for the Moon to depart the vicinity of the Earth. Qualitative tools developed to examine the three-body problem sought an answer this question [12]. Many researchers have expended great effort in support of other aspects of the three-body problem as well. June Barrow-Green offers an elegant statement of the problem [33]:

> "Three particles move in space under their mutual gravitational attraction; given their initial conditions, determine their subsequent motion.[1]"

Even with a straightforward problem statement, there is no known analytical solution. To deliver a more tractable problem, there are numerous simplifications and reformulations that also offer new insights into the problem. One useful reformulation that reduces complexity is the Circular Restricted Three-Body Problem (CRTBP).

2.1 Problem Definition

Reformulation of the general three-body problem via a set of simplifying assumptions yields the CRTBP. The purpose of analysis is then a determination of the motion of one body of infinitesimal mass subject to the gravitational forces of two massive

[1]Barrow-Green 1997, page 7

bodies. Hence, the two gravitational bodies, labelled P_1 and P_2, possess finite masses m_1 and m_2, respectively. The value of masses m_1 and m_2 are arbitrary, but assuming their shape to be perfectly spherical and their mass distributions to be perfectly uniform allows them to be modelled as point masses. These bodies, labelled the "primaries," move solely under their mutual gravitational attraction in a Keplerian orbit about their barycenter. Assuming that the primary conic motion is circular further reduces complexity. The third body, P_3, possesses infinitesimal mass m_3 and, thus, moves under the gravitational influence of the two primaries without affecting their motion. The resulting equations of motion are nonlinear and possess no closed form solutions by means of elementary functions. However, the CRTBP remains useful because it is representative of many types of naturally occurring motion in the solar system. Applied in the Sun-Earth-Moon system, the Sun and the Earth are modelled as the two massive primaries and the Moon is assumed as the massless body. In engineering applications, a common analysis models the primaries as the Sun and a planet, or a planet and its moon, with a spacecraft as the massless body. Such a formulation—the Earth-Moon-Spacecraft problem—is the focus of this work.

2.1.1 Rotating Reference Frame

Analysing the problem in a rotating frame of reference offers many benefits. First, consider the inertial coordinate system I with origin at the barycenter of the primaries, point B, with unit vectors $\hat{X},\ \hat{Y},\ \hat{Z}$ forming a dextral, orthonormal triad. (See Figure 2.1.) Since the primaries move on conic paths, their mutual plane of motion remains fixed and the angular momentum vector of the system is constant in magnitude and direction. The $\hat{Z}$ axis is depicted along the angular momentum vector and the $\hat{X}$ and $\hat{Y}$ axes lie in the plane of motion of the primaries. The rotating reference frame, R, centered at the barycenter with dextral, orthonormal unit vectors $\hat{x},\ \hat{y},\ \hat{z}$, is then defined such that it rotates with respect to the inertial frame. The $\hat{z}$ axis of the rotating frame is parallel to the inertial direction $\hat{Z}$. The $\hat{x}$ axis lies

along the line joining the primaries and rotates at the same rate so that it is always directed from P_1 towards P_2. The $\hat{y}$ axis completes the right-handed set of coordinate directions. The rotating frame moves counter-clockwise with respect to the inertial frame when viewed from the positive $\hat{z}$ direction at a constant rate due to the circular motion of the primaries. This rate, N, is the dimensional mean motion of the two-body system. Thus, the orientation of R with respect to I is evaluated as $\theta = N\kappa$ where κ is the dimensional time since the frames were aligned at $\theta_0 = \theta(\kappa_0) = 0$. The frames are then related as follows,

$$\begin{aligned} \hat{X} &= \hat{x}\cos\theta - \hat{y}\sin\theta \\ \hat{Y} &= \hat{x}\sin\theta + \hat{y}\cos\theta \\ \hat{Z} &= \hat{z}. \end{aligned} \tag{2.1}$$

The formulation of this analysis is focused in the rotating frame, but transforming the results into an inertial frame can enable a visual understanding of the motion.

2.1.2 Nondimensionalization and Definition of Variables

Nondimensionalization enables more general analysis of the equations of motion. A standard set of characteristic quantities is typically employed in the CRTBP. The characteristic quantities used to nondimensionalize the equations of motion include length, mass, and time, defined as

$$l^* = D_1 + D_2, \tag{2.2}$$

$$m^* = m_1 + m_2, \tag{2.3}$$

$$t^* = \sqrt{\frac{l^{*3}}{\tilde{G}m^*}}, \tag{2.4}$$

where D_1 and D_2 are the distances from the barycenter to each primary and $\tilde{G}$ is the dimensional universal gravitational constant. The characteristic time, t^*, is defined

as the inverse of the mean motion of the primaries, N. Recall that the mean motion is the angular rate of a two-body system, and may be written

$$N = \sqrt{\frac{Gm^*}{l^{*3}}},$$

with units [1/time]. Then, the nondimensional mean motion is the product of N and the characteristic time, i.e.,

$$n = Nt^* = 1. \tag{2.5}$$

Next, the nondimensional mass of P_2 is defined using the characteristic mass. This quantity is termed the mass parameter, μ, and is a significant parameter in the CRTBP model,

$$\mu = \frac{m_2}{m^*}. \tag{2.6}$$

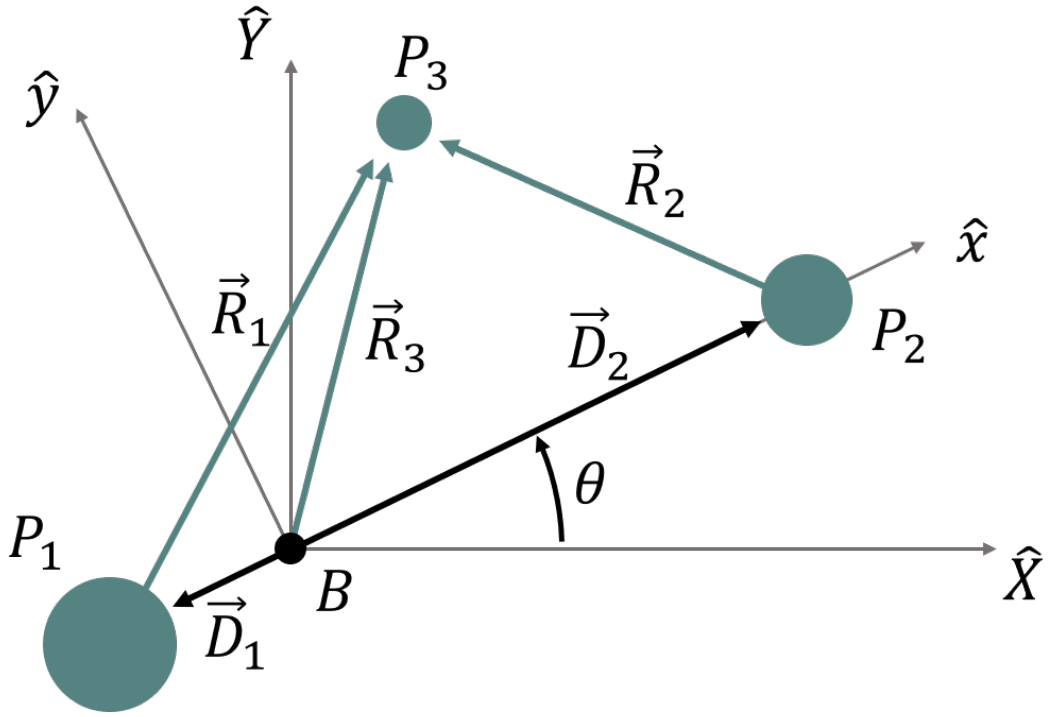

Figure 2.1. The rotating and inertial coordinate frames. The angular momentum vector is directed out of the page.

The nondimensional mass of the first primary is then

$$1 - \mu = \frac{m_1}{m^*}. \tag{2.7}$$

These quantities are also relevant to assess the position of the primaries in the rotating frame. Consider the center of mass of a system of particles along a line such that

$$R_{O,B} = \frac{1}{M} \sum_{i=1}^{n} m_i \; r_{O,i}, \tag{2.8}$$

where $R_{O,B}$ is the location of the center of mass with respect to some arbitrary point O along the line joining the particles, M is the sum of the masses of the particles, m_i is the mass of the i-th particle, and $r_{O,i}$ is the location of the i-th particle with respect to point O. If O is centered at the first primary, P_1, Equation (2.8) becomes

$$\begin{aligned} R_{P_1,B} &= \frac{1}{m^*}\left(m_1 \; r_{P_1,P_1} + m_2 \; r_{P_1,P_2}\right) \\ &= \frac{m_2}{m^*} \; r_{P_1,P_2} \\ &= \mu \; l^*, \end{aligned}$$

which supplies the dimensional distance of the barycenter with respect to the first primary in the rotating frame. Nondimensionalize by dividing by the characteristic length, then shift the origin from P_1 to the barycenter, and produce the nondimensional coordinates of the first primary in the rotating frame, denoted $\vec{D_1}$. The same procedure, centered at P_2, delivers the nondimensional representation of the location of the second primary in frame R, as follows

$$\vec{D_1} = -\mu \; \hat{x} \tag{2.9}$$

$$\vec{D_2} = (1 - \mu) \; \hat{x}. \tag{2.10}$$

The rotational relationship between coordinate frames I and R, in Equation (2.1), is also simplified. Recall that the nondimensional mean motion is equal to unity, then

the angle between the frames is expressed $\theta = nt = t$, where t is the nondimensional time. The rotations are then written as a simple function of time, that is

$$\begin{aligned} \hat{X} &= \hat{x}\cos t - \hat{y}\sin t \\ \hat{Y} &= \hat{x}\sin t + \hat{y}\cos t \\ \hat{Z} &= \hat{z}. \end{aligned} \tag{2.11}$$

A comparison of the characteristic quantities for common bodies in the solar system is summarized in Table 2.1.

Table 2.1. Approximate characteristic quantities in various systems. Notice that the Earth-Moon system possesses a relatively large mass parameter.

System	Mass Parameter, μ	Characteristic Mass, m^* [kg]	Characteristic Length, l^* [km]	Characteristic Time, t^* [sec]
Sun-Earth	3.003×10^{-6}	1.989×10^{30}	1.490×10^{8}	5.022×10^{6}
Sun-Jupiter	9.534×10^{-4}	1.991×10^{30}	7.786×10^{8}	5.959×10^{7}
Earth-Moon	0.01215	6.048×10^{24}	3.840×10^{5}	3.751×10^{5}
Jupiter-Europa	2.529×10^{-5}	1.898×10^{27}	6.710×10^{5}	4.884×10^{4}

2.2 Equations of Motion

The equations of motion in the CRTBP originate from direct application of Newton's second law and Newton's law of universal gravitation. The motion of the third body, subject to the gravity of two other bodies, is mathematically described by the dimensional second-order vector differential equation

$$\vec{F}_G = m_3\vec{R}_3'' = -\frac{\tilde{G}m_1m_3}{R_1^3}\vec{R}_1 - \frac{\tilde{G}m_2m_3}{R_2^3}\vec{R}_2, \tag{2.12}$$

where $\vec{R}_3''$ is the dimensional acceleration of the third body relative to the barycenter as viewed by an inertial observer, $\vec{R}_1$ is the relative position of the third body with

respect to the first primary, $\vec{R}_2$ is the relative position of the third body with respect to the second primary, and R_i is the magnitude of the corresponding vector. Note that all of the quantities in Equation (2.12) are dimensional, but the equation is easily rewritten in nondimensional form. The nondimensional barycentric position vector of P_3 in the rotating frame is

$$\vec{\rho} = x\ \hat{x} + y\ \hat{y} + z\ \hat{z}, \tag{2.13}$$

and the derivative with respect to nondimensional time as viewed by a rotating observer is

$$\dot{\vec{\rho}} = \dot{x}\ \hat{x} + \dot{y}\ \hat{y} + \dot{z}\ \hat{z}. \tag{2.14}$$

The six-dimensional state vector then possesses the form

$$\vec{x} = \begin{bmatrix} \vec{\rho} & \dot{\vec{\rho}} \end{bmatrix}^T = \begin{bmatrix} x & y & z & \dot{x} & \dot{y} & \dot{z} \end{bmatrix}^T.$$

The nondimensional relative position vectors of P_3 with respect to the primaries in the rotating frame are

$$\vec{r}_1 = \vec{\rho} - \vec{D}_1 = (x + \mu)\ \hat{x} + y\ \hat{y} + z\ \hat{z} \tag{2.15}$$

$$\vec{r}_2 = \vec{\rho} - \vec{D}_2 = (x - 1 + \mu)\ \hat{x} + y\ \hat{y} + z\ \hat{z} \tag{2.16}$$

Equation (2.12) is then rewritten in nondimensional form,

$$\ddot{\vec{\rho}}^I = -\frac{(1-\mu)}{r_1^3}\vec{r}_1 - \frac{\mu}{r_2^3}\vec{r}_2, \tag{2.17}$$

where $\ddot{\vec{\rho}}^I$ is the acceleration of P_3 relative to an inertial observer expressed in the inertial frame. Note that the position vectors $\vec{\rho}$, $\vec{r}_1$, and $\vec{r}_2$, and the velocity vector $\dot{\vec{\rho}}$, are defined in terms of the rotating frame, not the inertial frame. The accelerations in the equations of motion are better suited if expressed in terms of the rotating observer. Such a formulation requires kinematic expansions of the velocity and acceleration terms $\dot{\vec{\rho}}^I$ and $\ddot{\vec{\rho}}^I$. The velocity expansion, from the basic kinematic equation, is

$$\dot{\vec{\rho}}^I = \frac{{}^I d\rho}{dt} = \frac{{}^R d\rho}{dt} + {}^I\vec{\omega}^R \times \vec{\rho} + \dot{\vec{R}}^I_{OB}, \tag{2.18}$$

where ${}^{I}\bar{\omega}^{R}$ is the angular velocity of the rotating frame with respect to the inertial frame and $\dot{\vec{R}}^{I}_{OB}$ is the translational velocity of the origin of the rotating frame with respect to the origin of the inertial frame (which is zero in the CRTBP). The angular velocity is, by definition, ${}^{I}\bar{\omega}^{R} = n\hat{z}$, which is constant in magnitude and direction. The acceleration expansion is then similarly derived as

$$\ddot{\vec{\rho}}^{I} = \ddot{\vec{\rho}}^{R} + {}^{I}\bar{\omega}^{R} \times ({}^{I}\bar{\omega}^{R} \times \vec{\rho}) + {}^{I}\alpha^{R} \times \vec{\rho} + 2\,{}^{I}\bar{\omega}^{R} \times \dot{\vec{\rho}}^{R} + \ddot{\vec{R}}^{I}_{OB}, \tag{2.19}$$

where the angular acceleration of frame R with respect to frame I, ${}^{I}\vec{\alpha}^{R}$, and the translational acceleration of the base point of R with respect to the base point of I, $\ddot{\vec{R}}^{I}{}_{OB}$, are both zero. Evaluating the kinematic expressions in Equations (2.18) to (2.19) yields the following velocity and acceleration expansions relative to an inertial observer expressed in terms of the rotating frame:

$$\dot{\vec{\rho}}^{I} = (\dot{x} - ny)\hat{x} + (\dot{y} + nx)\hat{y} + \dot{z}\hat{z} \tag{2.20}$$

$$\ddot{\vec{\rho}}^{I} = (\ddot{x} - 2n\dot{y} - n^2x)\hat{x} + (\ddot{y} + 2n\dot{x} - n^2y)\hat{y} + \ddot{z}\hat{z}. \tag{2.21}$$

By combining Equation (2.21) with the nondimensional form of the n-body equation (Equation (2.17)) and the definitions of $\vec{r}_1$ and $\vec{r}_2$ (Equations (2.15) to (2.16)), the equations of motion written as their scalar components appear as

$$\ddot{x} - 2n\dot{y} - n^2x = -\frac{(1-\mu)(x+\mu)}{r_1^3} - \frac{\mu(x-1+\mu)}{r_2^3} \tag{2.22}$$

$$\ddot{y} + 2n\dot{x} - n^2y = -\frac{(1-\mu)y}{r_1^3} - \frac{\mu y}{r_2^3} \tag{2.23}$$

$$\ddot{z} = -\frac{(1-\mu)z}{r_1^3} - \frac{\mu z}{r_2^3}. \tag{2.24}$$

Recall that the nondimensional mean motion is equal to unity, but it is included it for completeness. Notice that, because of the formulation of the CRTBP, there are no time-dependent terms in the equations of motion, thus, the system is autonomous. To write the differential equations in an alternative form, introduce a "pseudo-potential" function, U^*, that is,

$$U^* = \frac{1-\mu}{r_1} + \frac{\mu}{r_2} + \frac{1}{2}n^2(x^2+y^2), \tag{2.25}$$

such that the equations of motion are also represented as

$$\ddot{x} - 2n\dot{y} = \frac{\partial U^*}{\partial x} \tag{2.26}$$

$$\ddot{y} + 2n\dot{x} = \frac{\partial U^*}{\partial y} \tag{2.27}$$

$$\ddot{z} = \frac{\partial U^*}{\partial z}. \tag{2.28}$$

The pseudo-potential function is used in future developments.

2.2.1 Integrals of the Motion (The Jacobi Constant)

Consider again the more general three-body problem, prior to the introduction of the simplifying assumptions for the circular restricted case. Finding the time history of the third body's position and velocity with respect to any point in space requires the simultaneous solution for the positions and velocities of all three bodies. Because there are three scalar position and three scalar velocity components of each state vector, the system therefore possesses 18 degrees of freedom. A analytical solution thus requires 18 integrals of the motion. There are only 10 known integrals of the motion available: one from conservation of energy, three due to conservation of angular momentum, and six due to conservation of linear momentum. The full three-body problem is, therefore, not solvable analytically.

The simplifying assumptions introduced by the CRTBP reduce the complexity of the problem. Restricting the motion of the two primaries to be two-body, conic orbits simplifies the primary motion. Further constraining the motion of the primaries to be on circular orbits and reformulating the equations of motion into the rotating frame results in a single integral of motion, termed the Jacobi constant, C.

The derivation of the Jacobi constant is straightforward. The dot product of the velocity vector with the gradient of the pseudo-potential, Equations (2.26) to (2.28), yields the following scalar quantity

$$\dot{\vec{\rho}} \cdot \nabla U^* = \dot{\vec{\rho}} \cdot \ddot{\vec{\rho}} = \dot{x}\frac{\partial U^*}{\partial x} + \dot{y}\frac{\partial U^*}{\partial y} + \dot{z}\frac{\partial U^*}{\partial z}. \tag{2.29}$$

Note that the vector gradient ∇U^* is equal to the acceleration vector, $\ddot{\vec{\rho}}$. The right side of this expression is equal to the time derivative of the pseudo-potential,

$$\frac{dU^*}{dt} = \frac{\partial U^*}{\partial x}\frac{\partial x}{\partial t} + \frac{\partial U^*}{\partial y}\frac{\partial y}{\partial t} + \frac{\partial U^*}{\partial z}\frac{\partial z}{\partial t}. \tag{2.30}$$

Recall that the pseudo-potential is autonomous, thus, $\frac{\partial U^*}{\partial t}$ is zero. The integral of the scalar dot product $\dot{\vec{\rho}} \cdot \ddot{\vec{\rho}}$ with respect to nondimensional time, and isolating the resulting constant, yields:

$$\int \dot{\vec{\rho}} \cdot \ddot{\vec{\rho}}\, dt = \frac{1}{2}(\dot{x}^2 + \dot{y}^2 + \dot{z}^2) = U^* - C,$$

or

$$C = 2U^* - v^2, \tag{2.31}$$

where $v = \dot{\rho}$. The Jacobi constant offers useful insights. It is often termed an "energy-like" quantity, because an increase in the relative velocity corresponds to a decrease in energy relative to the rotating frame. The term does not, however, represent a conservation of energy; the energy of the two-body system is constant, but the energy of the motion of P_3 is not. The term simply represents an integral of the equations of motion as formulated in the rotating frame [14].

There are many useful applications of the Jacobi constant. For example, the accuracy of the numerical process is assessed by evaluating C at every time step to ensure that it is a constant value (to machine precision). Another application of the Jacobi constant, used extensively in this work, informs the bounds on the motion of an object in the CRTBP. Note the v^2 term in definition of C in Equation (2.31). Because the square of the velocity magnitude is never an imaginary quantity, the minimum value of v^2 is zero. This condition imposes an inequality constraint on the pseudo-potential function. Since U^* depends only on position, this inequality results in a bound on the motion of P_3. Such bounds are labelled curves of zero velocity in the planar problem, and they provide a qualitative means for analysis of the motion.

2.2.2 Equilibrium Solutions (Libration Points)

An essential component of analysis in the CRTBP is the examination of the equilibrium points, also termed the libration—or Lagrange—points. With no analytical solution available for the equations of motion, libration points are particularly useful for providing insight. The equilibrium points exist at locations where all time derivatives in the governing equations of motion are zero. Any object placed exactly at such a location—and not subject to any perturbations—theoretically remains in that position for infinite time. To compute their numerical locations, all of the velocity and acceleration components are zero,

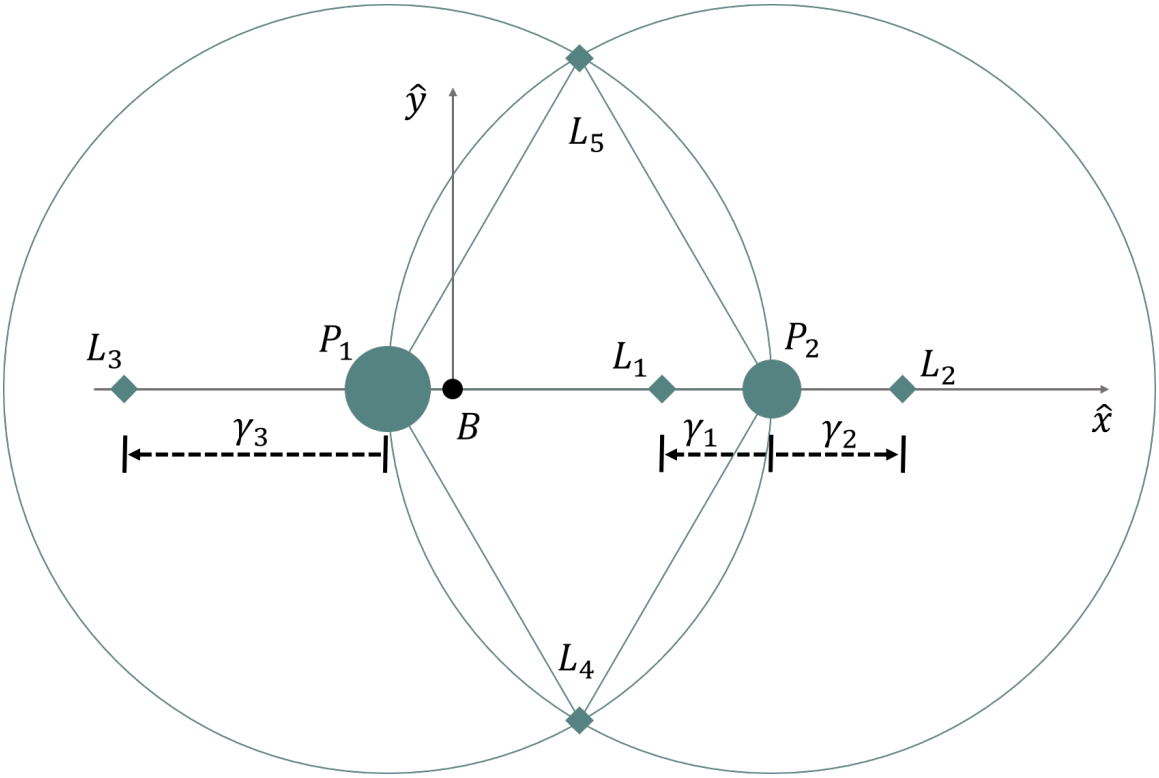

Figure 2.2. The five libration points, denoted by the green diamonds, plotted in the rotating frame. As the primaries rotate about their barycenter, the libration points remain fixed in the given orientation in the rotating frame.

$$\dot{x} = \dot{y} = \dot{z} = \ddot{x} = \ddot{y} = \ddot{z} = 0,$$

or equivalently,

$$\frac{\partial U^*}{\partial x} = \frac{\partial U^*}{\partial y} = \frac{\partial U^*}{\partial z} = 0.$$

From the equations of motion, Equations (2.22) to (2.24), expanding the partials yields

$$\frac{\partial U^*}{\partial x} = -x\left[\frac{1-\mu}{r_1^3} + \frac{\mu}{r_2^3} - 1\right] + \mu\left[\frac{-(1-\mu)}{r_1^3} - \frac{\mu}{r_2^3}\right] + \frac{\mu}{r_2^3} = 0 \tag{2.32}$$

$$\frac{\partial U^*}{\partial y} = -y\left[\frac{1-\mu}{r_1^3} + \frac{\mu}{r_2^3} - 1\right] = 0 \tag{2.33}$$

$$\frac{\partial U^*}{\partial z} = -z\left[\frac{1-\mu}{r_1^3} + \frac{\mu}{r_2^3}\right] = 0. \tag{2.34}$$

From here, the derivation follows Cox [34]. Observe that Equation (2.34) is only satisfied when $z = 0$. Thus, all of the equilibrium solutions exist in the $\hat{x}$-$\hat{y}$ plane, the plane of rotation of the primaries. Next, consider the solution when $y = 0$. Since these equilibrium points all lie on the $\hat{x}$-axis, they are denoted the collinear points. Only Equation (2.32) remains, and it reduces to

$$x - (1-\mu)\frac{x+\mu}{A(x+\mu)^3} - \mu\frac{x-1+\mu}{B(x-1+\mu)^3} = 0, \tag{2.35}$$

where $A = \text{sgn}(x+\mu)$ and $B = \text{sgn}(x-1+\mu)$. There are three possible combinations of A and B:

1. A is positive and B is negative (L_1, between the primaries),
2. Both A and B are positive (L_2, to the right of both primaries).
3. And both A and B are negative (L_3, to the left of both primaries).

An analytical solution is not available, so a quintic polynomial is solved numerically for each scenario. Typically, it is convenient to replace x by the distance from each primary, i.e., γ_1, γ_2, and γ_3, as defined in Figure 2.2, resulting in a more effective numerical algorithm.

The remaining equilibrium points exist when $y \neq 0$. When y is not constrained to be zero, then the term in the brackets in Equation (2.33) must instead evaluate to

zero. Since this same term exists in Equation (2.32), rewrite Equation (2.32) in the following form

$$x[0] + \mu[-1] + \frac{\mu}{r_2^3} = 0,$$

which simplifies to $r_2 = 1$. Substituting this value into Equation (2.32) results in $r_1 = 1$ as well. Thus, any equilibrium points where $y \neq 0$ must be one nondimensional distance from *both* primaries. The locations are apparent as the intersections of two circles of unity radius centered on each primary. Since the nondimensional distance between the primaries is also unity, two equilateral triangles appear; the equilibrium points are thus denoted the triangular points, L_4 and L_5. For reference, the Jacobi constant value corresponding to the locations of each libration point in the Earth-Moon system is listed in Table 2.2.

Table 2.2. Jacobi constant, Equation (2.39), evaluated at each libration point in the Earth-Moon system.

Location	C Value
L_1	3.1883
L_2	3.1722
L_3	3.0121
L_4	2.9885
L_5	2.9885

2.2.3 Symmetry and Mirroring

The equations of motion yield solutions that are symmetric across the x-z plane in reverse time. Consider a new set of coordinates that satisfy this symmetry condition: $x' = x,\ y' = -y,\ z' = z$, with $t' = -t$. The time derivatives are then $\frac{d}{dt'} = -\frac{d}{dt}$ and $\frac{d^2}{d^2t'} = \frac{d^2}{d^2t}$. Note that the primes in the following equations do *not* represent derivatives with respect to dimensional time. Substitute these values into the equations of motion

written using the pseudo-potential, Equations (2.26)–(2.28), to yield the transformed equations:

$$\frac{\partial U^*}{\partial x'} = \frac{d^2x'}{d\tau^2} - 2\frac{d(-y')}{d\tau} \tag{2.36}$$

$$-\frac{\partial U^*}{\partial y'} = -\frac{d^2y'}{d\tau^2} - 2\frac{dx'}{d\tau} \tag{2.37}$$

$$\frac{\partial U^*}{\partial z'} = \frac{d^2z'}{d\tau^2} \tag{2.38}$$

These transformed equations have the same structure as those in Equations (2.26)–(2.28). Thus, any solution to the transformed equations are also a solution to the original equations in reverse time, mirrored across the x-z plane. That is, if

$$\vec{x}(t) = \begin{bmatrix} x(t) & y(t) & z(t) & \dot{x}(t) & \dot{y}(t) & \dot{z}(t) \end{bmatrix}$$

is a solution to the equations of motion, so is

$$\vec{x'}(t') = \begin{bmatrix} x'(t') & y'(t') & z'(t') & \dot{x'}(t') & \dot{y'}(t') & \dot{z'}(t') \end{bmatrix}.$$

Therefore, for every trajectory in the CRTBP, there is a mirror image trajectory across the x-z plane in reverse time. This behavior is captured by the Mirror Theorem.

Theorem 2.1 (The Mirror Theorem): *If n point masses are acted upon by their mutual gravitational forces only, and at certain epoch each radius vector from the center of mass of the system is perpendicular to every velocity vector, then the orbit of each mass after that epoch is a mirror of its orbit prior to that epoch.* [35]

As a consequence of the the Mirror Theorem, if a trajectory crosses the x-z plane *perpendicularly* (that is, $y = 0,\ \dot{x} = 0$, and $\dot{z} = 0$) at two distinct locations, then the trajectory is periodic. This implication is leveraged to aid in the search for periodic orbits in the CRTBP.

2.3 Zero-Velocity Curves and Surfaces

These structures, as previously noted in Chapter 1 and Section 2.2.1, supply insight into the motion of P_3 by physically bounding its allowable region of space. Recall the Jacobi constant definition,

$$\begin{aligned} C &= 2U^* - v^2 \\ &= \frac{2(1-\mu)}{r_1} + \frac{2\mu}{r_2} + (x^2 + y^2) - v^2. \end{aligned} \tag{2.39}$$

Because the square of the relative velocity magnitude is never physically imaginary, an inequality constraint occurs on the pseudo-potential function, that is,

$$v^2 \geq 0$$
$$C \leq 2U^*$$

The values of U^* for $v = 0$ then define a boundary that restricts the path of P_3. These restricted areas of space, into which P_3 cannot cross, are designated "forbidden regions." Since U^* is a function of all three position components, these regions actually represent a three-dimensional surface. Constructing the zero velocity boundaries, or surfaces, requires implicitly solving U^* for position to satisfy

$$C = 2U^*. \tag{2.40}$$

The surfaces then depend only on C and μ. Note that μ is generally equal to a constant in the CRTBP. Thus, the regions of space accessible to a particle are directly linked to the value of Jacobi constant.

Consider first the two-dimensional case, i.e., planar motion where $z = 0$ and $\dot{z} = 0$. Sample bounding curves in the Earth-Moon CRTBP at a Jacobi constant value equal to $C = 3.22$ are plotted in Figure 2.3. Note that this value of C is greater than the value of C at L_1 by an arbitrary amount. The gray regions in Figure 2.3 represent a forbidden region which is not available to the particle. At the given energy level, a particle in the region around the Earth never departs the vicinity; the same is true

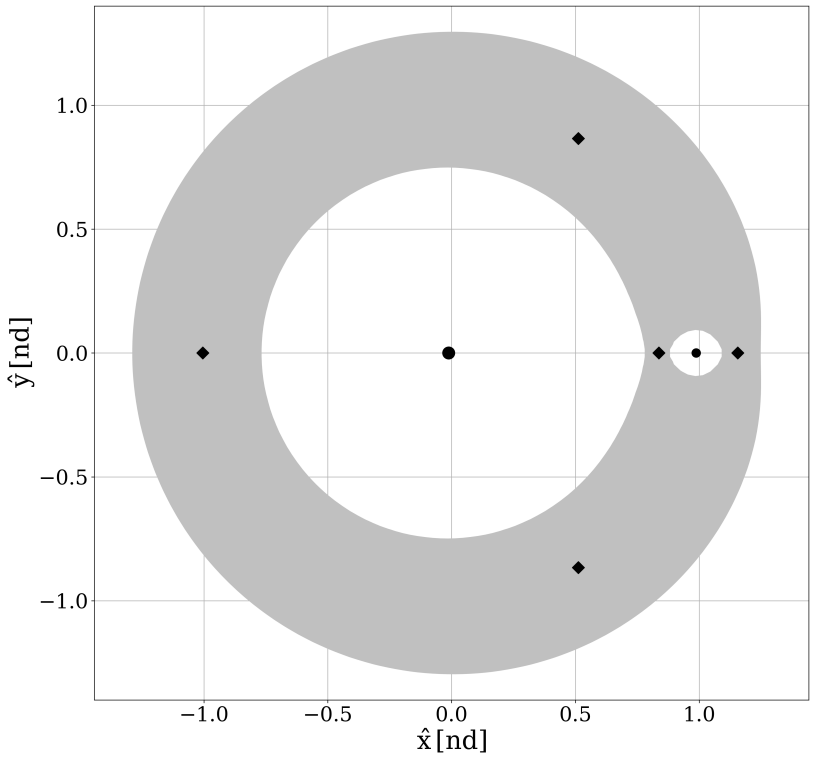

Figure 2.3. Zero velocity curves (ZVCs) in the Earth-Moon system at a $C = 3.22$. The equilibrium points are denoted as black diamonds, and the Earth (left) and Moon (right) appear as black circles

for the region surrounding the Moon. Sample paths are plotted in Figure 2.4, where arbitrary initial states corresponding to $C = 3.22$ are numerically integrated for 1,000 days. Note that the trajectories "bounce" off of the boundaries but never cross. To move between regions requires a change in Jacobi constant value.

Zero-velocity curves (ZVCs) evolve continuously with the Jacobi constant; as C decreases, energy increases, allowing for access to more regions. The first significant change occurs in the region of L_1, where the curves recede to create an opening between the primaries, as illustrated in Figure 2.5(a). Note that this opening does

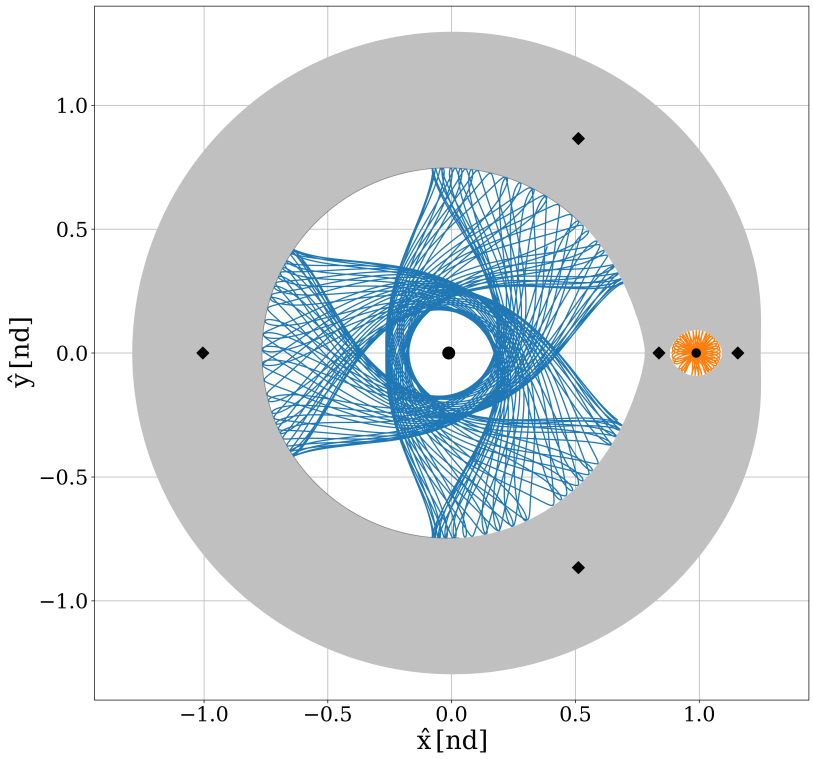

Figure 2.4. Trajectories propagated for 1000 days plotted with ZVCs. The blue curve represents a trajectory originating in the vicinity of the Earth, while the orange curve represents a trajectory with initial conditions near the Moon. The trajectories can never cross the boundaries, so they remain in their original regions of space.

not exist in the curves plotted in Figure 2.3. As C is further decreased, a gap emerges near L_2, joining the interior and exterior regions, as apparent in Figure 2.5(b). As C continues to decrease, the C-shape of the curves becomes smaller until it separates near L_3, Figure 2.5(c). The two distinct curves continue to shrink towards L_4 and L_5 until they disappear at a sufficiently high energy, Figure 2.5(d).

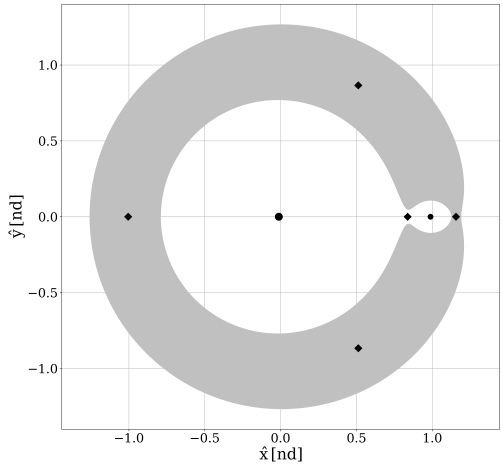

(a) $C_{L_2} < C < C_{L_1}$

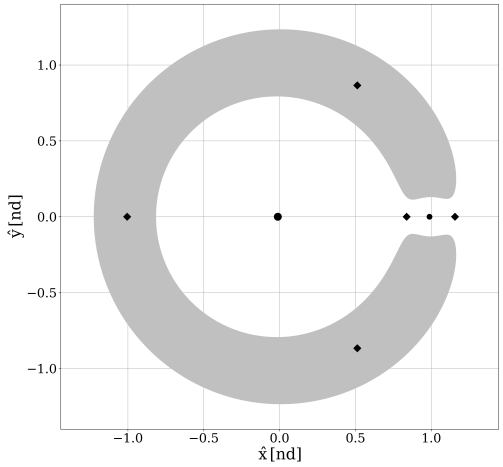

(b) $C_{L_3} < C < C_{L_2}$

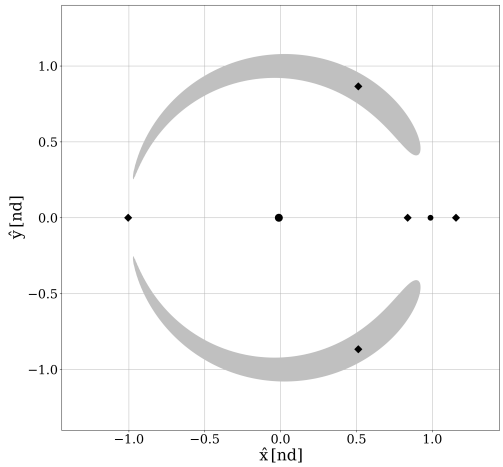

(c) $C_{L_4},\ C_{L_5} < C < C_{L_3}$

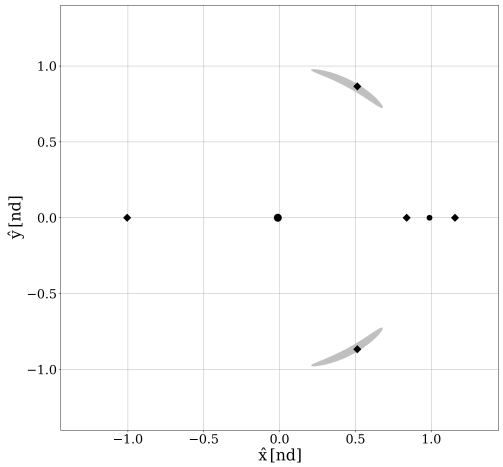

(d) $C_{L_4},\ C_{L_5} < C < C_{L_3}$

Figure 2.5. Evolution of the ZVCs in Earth-Moon system. As Jacobi constant decreases, the forbidden region shrinks. For a case where $C_{L_1} < C$, see Figure 2.3

Note that the curves in Figure 2.5 are simply two-dimensional slices of three-dimensional surfaces. Compared to the 3-D case, the two-dimensional curves are relatively simple. For the 3-D case, a sample surface appears in Figure 2.6.

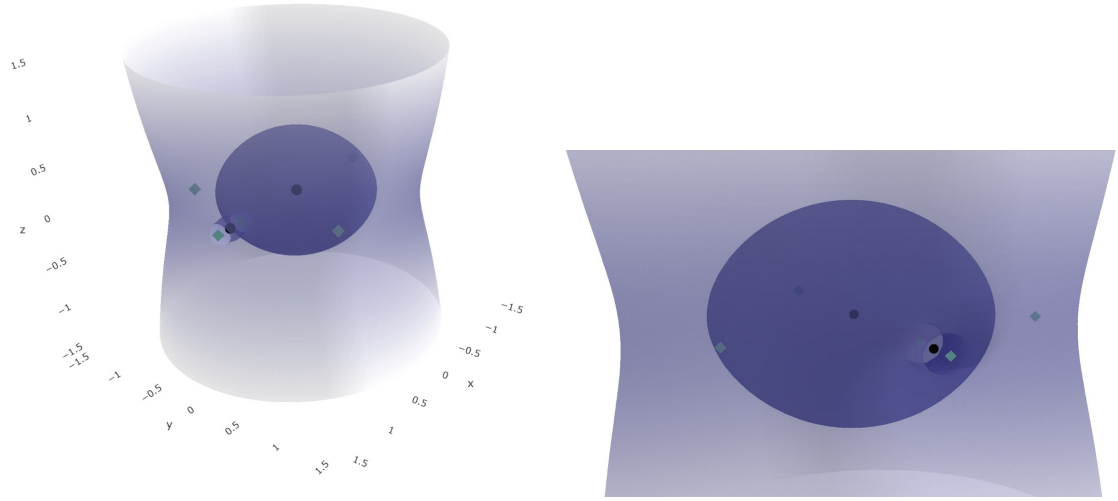

(a) Wide view (b) Zoomed view

Figure 2.6. Zero velocity surface in the Earth-Moon system at $C = 3.14$. The gateway from the interior region to the exterior region is open. The Earth and the Moon are denoted by black dots, and the libration points by green diamonds.

2.4 Theoretical Minimum Delta-V

The Jacobi constant may be leveraged to indicate the "effort" required to shift from one trajectory arc to another; the difference in Jacobi constant value between two arcs can provide an estimate of the minimum ΔV required to complete some idealized impulsive maneuver. The cost of such a maneuver will always be minimized when the velocity directions before and after the maneuver are parallel, freeing the maneuver to deliver only an energy change. This energy change is represented by the difference in Jacobi constant value: ΔC. There are multiple ways to formulate the theoretical minimum ΔV, but the one used in this investigation leverages the pseudo-potential, U^*:

$$\Delta V_{min} = \sqrt{2U^* - C_1} - \sqrt{2U^* - C_0}. \tag{2.41}$$

The values of C_0 and C_1 represent the Jacobi constant value before and after the maneuver, respectively. The theoretical minimum ΔV in Equation (2.41) is minimized when U^* is maximized. Thus, to create a bound on the minimum ΔV, the maximum value of U^* is chosen between the two arcs of interest. This formulation then assumes that there exists some arc, with at least one position state at this value of U^*, that intersects both orbits in position space. U^* will always be largest near one of the primaries. To visualize this dependence on U^* (and thus position), the theoretical minimum ΔV for an arbitrary ΔC is evaluated for a range of positions in the Earth-Moon system. This scalar field appears in Figure 2.7.

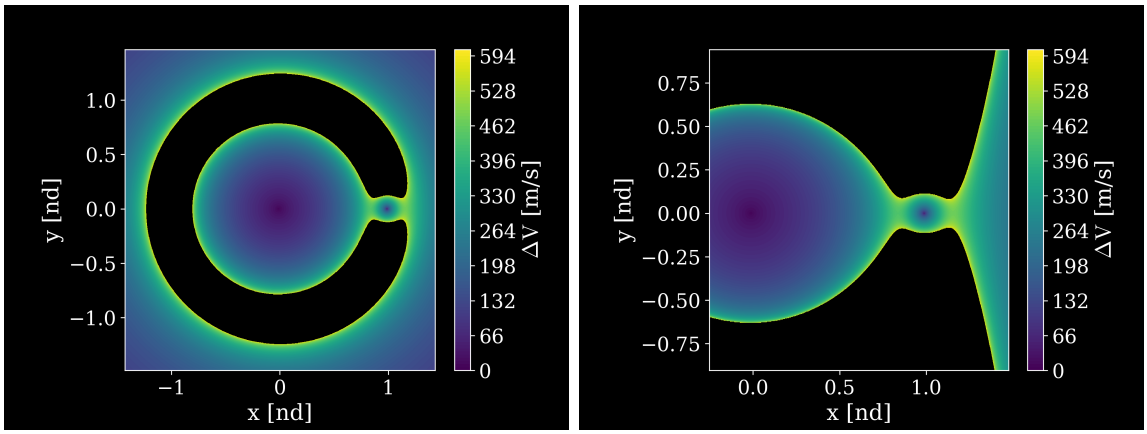

(a) x-y plane

(b) x-z plane

Figure 2.7. Theoretical minimum ΔV evaluated in the Earth-Moon system for an arbitrary Jacobi constant difference of $\Delta C = 0.35$.

3. DIFFERENTIAL CORRECTIONS

The equations of motion of the CRTBP are coupled, second-order, nonlinear, and possess no closed-form, analytical solutions. Thus, it is necessary to rely on numerical methods to propagate orbits and to generate motion that achieves specific goals. such trajectories may include those that are periodic or that reach a desired location in space. Construction of these trajectories frequently exploits differential corrections procedures—also known as shooting methods. However, differential corrections processes require sensitivity information to make reasonabl predictions, and numerical propagation yields only a single solution that offers no information about nearby motion. To gain insight into the types motion near point solutions, and to aid in the differential corrections process, the state transition matrix, or STM, is introduces. The STM is used in the formulation of shooting scheme. Methods of continuation are also introduced to expand point solutions into families of similar motion.

3.1 The State Transition Matrix

The state transition matrix leverages linearization techniques to relate variations in an initial state to variations in a state at a later time. The nonlinear equations of motion may be written in first order form as

$$\dot{\vec{x}} = \vec{f}(\vec{x},\ t), \tag{3.1}$$

where $\vec{x}$ is a column vector of the state elements in the rotating frame, that is $\vec{x} = [x,\ y,\ z,\ \dot{x},\ \dot{y},\ \dot{z}]^T$. Consider a reference solution to Equation (3.1), $\vec{x}_*(t)$. A trajectory near the reference solution, $\vec{x}(t)$, has the form $\vec{x}(t) = \vec{x}_*(t) + \delta\vec{x}(t)$ where $\delta\vec{x}(t)$ is a small deviation from the reference solution. Substituting $\vec{x}(t)$ into Equa-

tion (3.1) allows the equation to be written as a function of the reference state and a perturbation, for example

$$\dot{\vec{x}} = \dot{\vec{x}}_* + \delta\dot{\vec{x}} = \vec{f}(\vec{x}_* + \delta\vec{x}, t). \tag{3.2}$$

Apply a first-order Taylor series expansion to $\vec{f}$ about the reference solution, $\vec{x}_*$:

$$\dot{\vec{x}} = \dot{\vec{x}}_* + \delta\dot{\vec{x}} \approx \vec{f}(\vec{x}_*, t) + \left.\frac{\partial \vec{f}}{\partial \vec{x}}\right|_{\vec{x}_*} (\vec{x} - \vec{x}_*) + \text{Higher Order Terms},$$

and ignore terms of order two or higher. Since $\vec{x}_*$ is a solution to Equation (3.1), one can substitute $\dot{\vec{x}}_*$ for $\vec{f}(\vec{x}_*, t)$ and eliminate $\dot{\vec{x}}_*$ from both sides of the equation. Substituting $\delta\vec{x}$ for $(\vec{x} - \vec{x}_*)$ then yields

$$\begin{aligned} \delta\dot{\vec{x}} &= \left.\frac{\partial \vec{f}}{\partial \vec{x}}\right|_{\vec{x}_*} \delta\vec{x}, \\ \delta\dot{\vec{x}} &= \mathbf{A}\delta\vec{x}, \end{aligned} \tag{3.3}$$

where $\mathbf{A}$ is the Jacobian matrix of partials for $\vec{f}$ with respect to the state vector $\vec{x}$ evaluated at the reference $\vec{x}_*$. The elements of $\mathbf{A}(t)$ are then

$$\mathbf{A}(t) = \begin{bmatrix} 0 & 0 & 0 & 1 & 0 & 0 \\ 0 & 0 & 0 & 0 & 1 & 0 \\ 0 & 0 & 0 & 0 & 0 & 1 \\ \frac{\partial U^*}{\partial x \partial x} & \frac{\partial U^*}{\partial x \partial y} & \frac{\partial U^*}{\partial x \partial z} & 0 & 2n & 0 \\ \frac{\partial U^*}{\partial y \partial x} & \frac{\partial U^*}{\partial y \partial y} & \frac{\partial U^*}{\partial y \partial z} & -2n & 0 & 0 \\ \frac{\partial U^*}{\partial z \partial x} & \frac{\partial U^*}{\partial z \partial y} & \frac{\partial U^*}{\partial z \partial z} & 0 & 0 & 0 \end{bmatrix}.$$

Equation (3.3) represents a linear system, so all of its solutions satisfy

$$\delta\vec{x}(t) = e^{A(t-t_o)}\delta\vec{x}(t_0). \tag{3.4}$$

Thus, Equation (3.4) is the general solution to Equation (3.3). The matrix $e^{A(t-t_0)}$ is denoted the state transition matrix (STM), or sensitivity matrix. It may be written more explicitly as

$$\Phi(t,\ t_0) = e^{A(t-t_0)} = \frac{\delta\vec{x}(t)}{\delta\vec{x}(t_0)}. \tag{3.5}$$

The evolution of the STM is captured by its time derivative, which satisfies Equation (3.3) such that

$$\dot{\Phi}(t,\ t_0) = \mathbf{A}(t)\Phi(t,\ t_0). \tag{3.6}$$

The equations of motion for the STM in Equation (3.6) are computed simultaneously with the equations of motion for the state vector $\vec{x}(t)$, Equations (2.22) to (2.24). Some useful properties of the STM include

$$\Phi(t_0,\ t) = \Phi^{-1}(t,\ t_0), \tag{3.7}$$

$$\Phi(t_2,\ t_0) = \Phi(t_2,\ t_1)\Phi(t_1,\ t_0), \tag{3.8}$$

$$\Phi(t_0,\ t_0) = \mathbf{I}_{6\times 6}, \tag{3.9}$$

$$\det\ \Phi(t,\ t_0) = 1. \tag{3.10}$$

It is useful to examine the components of the STM individually, and to group them together as follows

$$\Phi(t,\ t_0) = \begin{bmatrix} \frac{\partial x}{\partial x_0} & \frac{\partial x}{\partial y_0} & \frac{\partial x}{\partial z_0} & \frac{\partial x}{\partial \dot{x}_0} & \frac{\partial x}{\partial \dot{y}_0} & \frac{\partial x}{\partial \dot{z}_0} \\ \frac{\partial y}{\partial x_0} & \frac{\partial y}{\partial y_0} & \frac{\partial y}{\partial z_0} & \frac{\partial y}{\partial \dot{x}_0} & \frac{\partial y}{\partial \dot{y}_0} & \frac{\partial y}{\partial \dot{z}_0} \\ \frac{\partial z}{\partial x_0} & \frac{\partial z}{\partial y_0} & \frac{\partial z}{\partial z_0} & \frac{\partial z}{\partial \dot{x}_0} & \frac{\partial z}{\partial \dot{y}_0} & \frac{\partial z}{\partial \dot{z}_0} \\ \frac{\partial \dot{x}}{\partial x_0} & \frac{\partial \dot{x}}{\partial y_0} & \frac{\partial \dot{x}}{\partial z_0} & \frac{\partial \dot{x}}{\partial \dot{x}_0} & \frac{\partial \dot{x}}{\partial \dot{y}_0} & \frac{\partial \dot{x}}{\partial \dot{z}_0} \\ \frac{\partial \dot{y}}{\partial x_0} & \frac{\partial \dot{y}}{\partial y_0} & \frac{\partial \dot{y}}{\partial z_0} & \frac{\partial \dot{y}}{\partial \dot{x}_0} & \frac{\partial \dot{y}}{\partial \dot{y}_0} & \frac{\partial \dot{y}}{\partial \dot{z}_0} \\ \frac{\partial \dot{z}}{\partial x_0} & \frac{\partial \dot{z}}{\partial y_0} & \frac{\partial \dot{z}}{\partial z_0} & \frac{\partial \dot{z}}{\partial \dot{x}_0} & \frac{\partial \dot{z}}{\partial \dot{y}_0} & \frac{\partial \dot{z}}{\partial \dot{z}_0} \end{bmatrix} = \begin{bmatrix} \Phi_{rr} & \Phi_{rv} \\ \Phi_{vr} & \Phi_{vv} \end{bmatrix}. \tag{3.11}$$

The upper left 3×3 quadrant, Φ_{rr}, represents changes in the final position state vector to changes in the initial position state vector, the upper right quadrant, Φ_{rv}, similarly relates changes in the final position state vector to changes in the initial velocity state vector. The submatrices Φ_{vr} and Φ_{vv} then follow. It convenient to label elements of $\Phi(t,\ t_0)$ by their row and column indices. For example, the partial $\frac{\partial \dot{x}}{\partial z_0}$ is also identified $\Phi_{4,3}$.

3.2 Shooting Methods

Due to the nonlinear nature of the CRTBP, it is often necessary to rely on numerical methods to achieve some desired motion; random initial states are not likely to deliver the motion of interest. The goal of the differential corrections process is, then, to select an initial state that meets some set of constraints. The differential corrections process is formulated as a shooting scheme, using the STM to iteratively update an initial guess to meet the design criteria. There are multiple approaches to solving a two-point boundary value problem, but the one employed in this analysis uses a multi-dimensional constraint/free variable Newton-Raphson procedure because it is versatile and easy to implement.

An appropriate framework for the implementation of any corrections process is important for meaningful results. The components of the free variable vector, or the design variable vector, are the quantities that are adjusted by the algorithm to achieve the desired constraints. The design variables typically include state vector components, time of flight, epoch time, phase angles, or any other variable of interest of tcan be modified. The constraint vectors are comprised of similar components, and are constructed to achieve some type of desired motion, such as a trajectory that reaches an exact position in space, or a path that is periodic. The differential corrections process aims to drive the error in the constraint vector to zero (within some tolerance) by manipulating the components of the free variable vector. Consider the free variable vector $\bar{X}$ with n components, and the constraint vector $\vec{F}(\vec{X})$ with m components, such that

$$\vec{X} = \begin{bmatrix} X_1 \\ X_2 \\ \vdots \\ X_n \end{bmatrix}, \qquad \vec{F}(\vec{X}) = \begin{bmatrix} F_1(\vec{X}) \\ F_2(\vec{X}) \\ \vdots \\ F_m(\vec{X}) \end{bmatrix} = \vec{0}.$$

Notice that the constraints are defined so that they are equal to zero for a satisfactory vector $\vec{X}$. In practice, this process becomes solving for $\vec{X}$ such that $\vec{F}(\vec{X})$ is zero to within a predefined tolerance, e, that is

$$||\vec{F}(\vec{X}_*)|| \leq e \tag{3.12}$$

where $\vec{X}_*$ is the value of $\vec{X}$ such that all constraints are satisfied, and $||\cdot||$ is the L^2 norm. A linear approximation is employed to relate changes in the components of $\vec{X}$ to changes in the components $\vec{F}(\vec{X})$. This relationship allows the corrections algorithm to implement corrective updates to the vector $\vec{X}$ that shift it towards $\vec{X}_*$ and drive the error in $\vec{F}(\vec{X})$ towards zero. Expand $\vec{F}(\vec{X})$ in a first order Taylor series about an initial guess for the design vector, $\vec{X}_0$:

$$\vec{F}(\vec{X}_*) = \vec{F}(\vec{X}_0) + \mathbf{DF}(\vec{X}_0)(\vec{X}_* - \vec{X}_0), \tag{3.13}$$

ignoring terms of order two or higher in the Taylor series expansion. The matrix $\mathbf{DF}(\vec{X}_0)$ is the $m \times n$ Jacobian matrix of partial derivatives of the constraint elements with respect to the design variables. All matrix quantities in this investigation are denoted by a bold typeface. The Jacobian matrix has the form

$$\mathbf{DF}(\vec{X}_0) = \begin{bmatrix} \frac{\partial F_1}{\partial X_1} & \cdots & \frac{\partial F_1}{\partial X_n} \\ \vdots & \ddots & \vdots \\ \frac{\partial F_m}{\partial X_1} & \cdots & \frac{\partial F_m}{\partial X_n} \end{bmatrix}.$$

Recognizing that $\vec{F}(\vec{X}_*)$ evaluates to zero, Equation (3.13) reduces to

$$\vec{F}(\vec{X}_0) + \mathbf{DF}(\vec{X}_0)(\vec{X}_* - \vec{X}_0) = \vec{0}. \tag{3.14}$$

Isolate $\vec{X}_*$ in Equation (3.14) to solve for the values of the design variables that satisfy the constraints. In practice, though, it is rare for $\vec{F}(\vec{X}_*)$ to reach zero with only a single update, as linear predictions are approximating the nonlinear dynamics. Hence, Equation (3.14) serves as an update equation to iteratively solve for $\vec{X}_*$. Substitute the more general variables $\vec{X}_i$, the current iteration, and $\vec{X}_{i+1}$, the next iteration, into Equation (3.14) to represent $\vec{X}_0$ and $\vec{X}_*$ respectively, and isolate $\vec{X}_{i+1}$, that is

$$\vec{X}_{i+1} = \vec{X}_i - \mathbf{DF}^{-1}(\vec{X}_i)\vec{F}(\vec{X}_i). \tag{3.15}$$

Notice that **DF** is only invertible if $m = n$, where the number of scalar constraints and the number of scalar design variables is equal. If $m \neq n$, other approaches are required to determine an appropriate update equation.

Consider first an over-determined system, where the constraints outnumber the design variables ($m > n$). There are no solutions that satisfy Equation (3.14), unless some of the constraints are linear functions of others. If there is no solution, however, a least squares method is typically applied to minimize the errors in the constraint vector. The least squares update equation is

$$\vec{X}_{i+1} = \vec{X}_i - [\mathbf{DF}(\vec{X}_i)^T \ \mathbf{DF}(\vec{X}_i)]^{-1} \ \mathbf{DF}(\vec{X}_i)^T \ \vec{F}(\vec{X}_i). \tag{3.16}$$

In the case of an under-determined system, the number of scalar design variables is greater than the number of constraints, or $n > m$. In this case, there are infinitely many solutions to $\vec{X}_*$, and there are any number of options to solve the system of equations. The options selected in this work is the minimum-norm solution. The minimum-norm seeks an update to $\vec{X}_i$ that is as close as possible to the previous iteration. The update then retains many of the same characteristics of the initial guess, which is useful if the initial guess possesses some desirable geometry. The minimum-norm update equation is then

$$\vec{X}_{i+1} = \vec{X}_i - \mathbf{DF}(\vec{X}_i)^T \ [\mathbf{DF}(\vec{X}_i) \ \mathbf{DF}(\vec{X}_i)^T]^{-1} \ \vec{F}(\vec{X}_i). \tag{3.17}$$

While a solution is not guaranteed by any differential corrections process, a "good" initial guess frequently delivers favorable results in a small number of iterations; the convergence rate is quadratic.

3.2.1 Single-Shooting

A single-shooting targeting scheme is a simple but useful example of the corrections process. Consider a spacecraft moving in the CRTBP. Its initial state $\vec{x}_0 = \vec{x}(t_0) = [x_0, \ y_0, \ z_0, \ \dot{x}_0, \ \dot{y}_0, \ \dot{z}_0]$ is propagated for time τ. At time $t_0 + \tau$, the state vector arrives at some point in space with state $\vec{x}_f = \vec{x}(t_0 + \tau) = [x_f, \ y_f, \ z_f, \ \dot{x}_f, \ \dot{y}_f, \ \dot{z}_f]$.

Suppose it is desired for the spacecraft to reach some different position in space, i.e., $\vec{\rho}_* = \vec{\rho}(t_0 + \tau) = [x_*,\ y_*,\ z_*]$, with no restriction on the velocity at $\vec{\rho}_*$ and with the time of flight, τ, allowed to vary. An impulsive maneuver implemented at the initial position can deliver the spacecraft to the desired position at the end of the propagation. See Figure 3.1 for a schematic. With the position components in the initial state vector fixed, the design variable vector is comprised of the initial velocity components and the propagation time, so

$$\vec{X} = \begin{bmatrix} \dot{x}_0 \\ \dot{y}_0 \\ \dot{z}_0 \\ \tau \end{bmatrix},$$

and the constraint vector captures the final position requirements:

$$\vec{F}(\vec{X}) = \begin{bmatrix} x_f - x_* \\ y_f - y_* \\ z_f - z_* \end{bmatrix}.$$

Notice that the constraint vector tends to zero when the final position components are equal to the desired position components. Of course, there are an infinite number of solutions since there are more free variables than constraints (i.e., $n > m$). The Jacobian for this targeting scheme predicts changes in final the position with respect to changes in the initial velocity and time of flight. Thus, $\mathbf{DF}(\vec{X})$ has the form

$$\mathbf{DF}(\vec{X}) = \begin{bmatrix} \frac{\partial(x_f - x_*)}{\partial \dot{x}_0} & \frac{\partial(x_f - x_*)}{\partial \dot{y}_0} & \frac{\partial(x_f - x_*)}{\partial \dot{z}_0} & \frac{\partial(x_f - x_*)}{\partial \tau} \\ \frac{\partial(y_f - y_*)}{\partial \dot{x}_0} & \frac{\partial(y_f - y_*)}{\partial \dot{y}_0} & \frac{\partial(y_f - y_*)}{\partial \dot{z}_0} & \frac{\partial(y_f - y_*)}{\partial \tau} \\ \frac{\partial(z_f - z_*)}{\partial \dot{x}_0} & \frac{\partial(z_f - z_*)}{\partial \dot{y}_0} & \frac{\partial(z_f - z_*)}{\partial \dot{z}_0} & \frac{\partial(z_f - z_*)}{\partial \tau} \end{bmatrix}. \tag{3.18}$$

Since the desired position components are explicitly defined and not a function of the design variables, every partial derivative of the desired position components is zero. The partials of the final position states with respect to time are simply the time derivative of those state components at the final time—final velocity components,

in this case. The remaining terms are variations in final position with respect to variations in the initial velocity, i.e., the exact elements of the STM, $\Phi(t0,\ t_0 + t)$. Specifically, they are the 3×3 upper-right quadrant, or Φ_{rv}. Substituting these terms into Equation (3.18) yields

$$\mathbf{DF}(\vec{X}) = \begin{bmatrix} \Phi_{14} & \Phi_{15} & \Phi_{16} & \dot{x}_f \\ \Phi_{24} & \Phi_{25} & \Phi_{26} & \dot{y}_f \\ \Phi_{34} & \Phi_{35} & \Phi_{36} & \dot{z}_f \end{bmatrix}. \tag{3.19}$$

Since the Jacobian is under-determined, there are an infinite number of solutions for the update equation. Thus, the minimum-norm solution is implemented, Equation (3.17). This targeting formulation could be altered in a straightforward manner

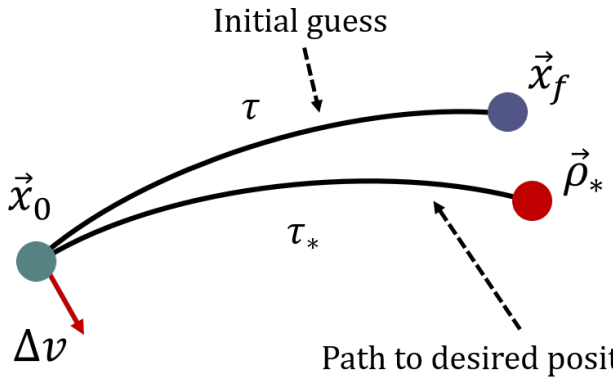

Figure 3.1. Representation of the targeting scheme. An impulsive maneuver applied at the initial position and a new time of flight deliver the spacecraft to the desired point.

by selecting different design variables and/or constraints. For example, one of the initial velocities or the propagation time can be removed from the design variable vector to produce a square Jacobian matrix. Targeting schemes that do not possess integration time as a free variable are labelled "fixed-time," while those that incorporate adjustments in time are labelled "variable-time." Both are valid options that exist in mission design scenarios.

Another trade-off in the differential corrections process is the update of the STM. Since each iteration of the initial guess is itself a unique trajectory, the STMs are accordingly unique for each iteration. However, depending upon the sensitivities of the specific problem, it is possible that the STM associated with the initial guess is sufficient to determine a free variable vector that satisfies the constraints. That is, in some cases, it may be possible to converge on a solution without ever updating the STM. Two such examples include cases where the changes between each iteration are small, and/or the target conditions are not sufficiently different from the initial guess. Since STM propagation requires an additional 36 equations of motion, such a trade-off may be worthwhile if the computational burden is a concern.

3.2.2 Multiple-Shooting

Multiple-shooting is a powerful extension of the single-shooting scheme that allows for longer propagation times and applications to more complex trajectories. It is especially beneficial for trajectories with close passes near the primaries, a dynamically sensitive event. Also, multiple-shooting strategies typically allow finer control of the solution than single-shooting methods. Despite the additional complexity of multiple-shooting schemes, the free variable/constraint vector formulation is, in essence, the same as in the single-shooting case. The multiple-shooting strategy adjusts multiple distinct trajectory arcs simultaneously, forcing continuity between each arc. The individual arcs may be provided as entirely separate trajectories with a goal to simply link them together, or they may be generated from one long arc that has been discretized into smaller segments. The originating point of each segment, as well as the desired target position, are denoted patch points. Thus, a multiple-shooting scheme possesses n patch points and $n-1$ arcs; the last patch point is not propagated and serves as an endpoint that may be constrained. See Figure 3.2 for a graphical representation. Similar to a single-shooting algorithm, multiple-shooting schemes can use a fixed or a variable integration time. For the variable-time formulation, though, the targeter

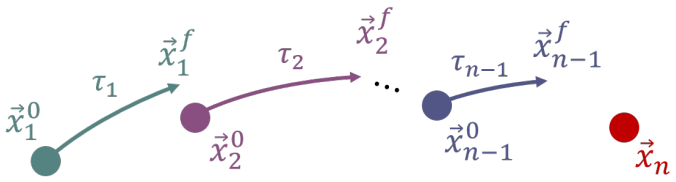

Figure 3.2. Representation of a multiple-shooting scheme. $\vec{x}_i^0$ represents the initial state of the i-th arc, the superscript f represents the final state of the corresponding arc, and τ_i reprsents the propagation time along each arc.

can adjust the integration time of every arc independently (that is, allow each arc to be defined with a different integration time, as illustrated in Figure 3.2), or it can force each arc to incorporate some constant subdivision of the total time for every iteration. Another benefit of the multiple-shooting formulation is the ability to add or remove extra constraints between arcs. For example, forcing position continuity between two patch points, but not velocity continuity, is analogous to introducing an instantaneous maneuver. This example is useful for joining complex transfer arcs or designing a multi-maneuver transfer.

The shooting scheme may be formulated in multiple ways. For this example, consider a scenario in which continuity is enforced between n patch points for a continuous trajectory, allowing the propagation time to vary along each segment. The design variable vector then includes $7n-1$ components in the following form,

$$\vec{X} = \begin{bmatrix} \vec{x}_1^0 & \vec{x}_2^0 & \vec{x}_3^0 & \dots & \vec{x}_{n-1}^0 & \vec{x}_n & \tau_1 & \tau_2 & \tau_3 & \dots, \tau_{n-1} \end{bmatrix}^T. \tag{3.20}$$

The constraint vector, enforcing a continuous trajectory, incorporates $6n-6$ elements with the following form,

$$\vec{F}(\vec{X}) = \begin{bmatrix} \vec{x}_1^f - \vec{x}_2^0 \\ \vec{x}_2^f - \vec{x}_3^0 \\ \vdots \\ \vec{x}_{n-1}^f - \vec{x}_n \end{bmatrix}^T. \tag{3.21}$$

The ordering of the components in $\vec{F}(\vec{X})$ and $\vec{X}$ creates a pattern in the Jacobian matrix that can be beneficial. To further simplify process, subdivide the Jacobian matrix into two parts: the partial derivatives with respect the patch point state vectors, $\mathbf{DF}_1$, and the partials with respect to time, $\mathbf{DF}_2$. Consider the first row and column of $\mathbf{DF}_1$, which defines the partials $\frac{\partial \vec{x}_1^f - \vec{x}_2^0}{\partial \vec{x}_1^0}$. Since, $\vec{x}_2^0$ is not a function of $\vec{x}_1^0$, the first term simplifies to $\frac{\partial \vec{x}_1^f}{\partial \vec{x}_1^0}$, which reflects the STM for the appropriate patch point, $\Phi(t_1 + \tau_1,\ t_1)$. For brevity, define $\Phi_1 = \Phi(t_1 + \tau_1,\ t_1)$ in this example. The next column of $\mathbf{DF}_1$, the term $\frac{\partial \vec{x}_1^f - \vec{x}_2^0}{\partial \vec{x}_2^0}$, simplifies to $\frac{-\partial \vec{x}_2^0}{\partial \vec{x}_2^0}$, or simply the identity matrix $-\mathbf{I}_{6\times 6}$. The remaining terms in this row evaluate to zero. The matrix $\mathbf{DF}_1$ then results in the following form:

$$\mathbf{DF}_1 = \begin{bmatrix} \Phi_1 & -\mathbf{I}_{6\times 6} & \mathbf{0}_{6\times 6} & \dots & \mathbf{0}_{6\times 6} & \mathbf{0}_{6\times 6} \\ \mathbf{0}_{6\times 6} & \Phi_2 & -\mathbf{I}_{6\times 6} & \dots & \mathbf{0}_{6\times 6} & \mathbf{0}_{6\times 6} \\ & & & \vdots & & \\ \mathbf{0}_{6\times 6} & \mathbf{0}_{6\times 6} & \mathbf{0}_{6\times 6} & \dots & \Phi_{n-1} & -\mathbf{I}_{6\times 6} \end{bmatrix} \tag{3.22}$$

Notice the diagonal structure of the patch point STMs and the identity matrices. The elements of $\mathbf{DF}_2$ reduce in a similar manner. The first row and column of $\mathbf{DF}_2$ represents the term $\frac{\partial \vec{x}_1^f - \vec{x}_2^0}{\partial \tau_1}$. Since $\vec{x}_2^0$ is not a function of τ_1, the term simplifies to $\frac{\partial \vec{x}_1^f}{\partial \tau_1}$, i.e., simply the time derivative of the state vector at the end of the segment, $\dot{\vec{x}}_1^f$. The remaining elements of the row evaluate to zero, so $\mathbf{DF}_2$ reduces to the form

$$\mathbf{DF}_2 = \begin{bmatrix} \dot{\vec{x}}_1^f & \vec{0}_{6\times 1} & \dots & \vec{0}_{6\times 1} \\ \vec{0}_{6\times 1} & \dot{\vec{x}}_2^f & \dots & \vec{0}_{6\times 1} \\ & & \vdots & \\ \vec{0}_{6\times 1} & \vec{0}_{6\times 1} & \dots & \dot{\vec{x}}_{n-1}^f \end{bmatrix}. \tag{3.23}$$

The Jacobian matrix is then the combination of each submatrix:

$$\mathbf{DF} = \begin{bmatrix} \mathbf{DF}_1 & \mathbf{DF}_2 \end{bmatrix}. \tag{3.24}$$

In this example, the formula for the update equation requires the minimum-norm solution, as the system in under-determined. However, the addition of constraints, if desired, could deliver a square Jacobian.

3.2.3 Computing Periodic Orbits by Exploiting Symmetry

Periodic orbits are one of the fundamental types of motion exploited by mission designers. There are *many* types of periodic motion in the CRTBP with diverse characteristics, and, as in the two-body Keplerian context, the number of periodic orbits is infinite. One way of classifying these orbits is by their symmetry: some orbits are symmetric with respect to a plane defined by two unit vectors in the rotating frame, some orbits are symmetric with respect to *two* of such planes, and some are simply not symmetric. Orbits that are symmetric across the xz-plane are particularly significant for the applications of this investigation. Targeting schemes can leverage this symmetry to constract exactly periodic solutions.

The Mirror Theorem was introduced in Section 2.2.3. By this theorem, a trajectory that possesses two distinct perpendicular crossings of the xz-plane must be periodic. Leveraging this property, a targeting scheme produces a periodic orbit by locating initial conditions that produce a perpendicular crossing at both ends of the arc. Consider an initial state on the x-axis propagated for time τ,

$$\vec{x}_0 = \begin{bmatrix} x_0 & 0 & 0 & 0 & \dot{y}_0 & 0 \end{bmatrix}.$$

The initial state is defined as a perpendicular crossing of the xz-plane, such that $y_0 = z_0 = \dot{x}_0 = \dot{z}_0 = 0$. It is also planar, but orbits symmetric to the xz-plane are not required to be so; there are 3-D orbits that also possess two perpendicular crossings of the xz-plane. However, since both z_0 and $\dot{z}_0$ are zero, the orbit is planar for all time, simplifying the design. A periodic orbit is delivered if the final state is also perpendicular, so a targeter is designed to adjust x_0 and $\dot{y}_0$ such that, at the final state, all state elements except y_f and $\dot{x}_f$ are zero. This scheme is represented by the green trajectories in Figure 3.3. Allow, also, the propagation time vary. Using

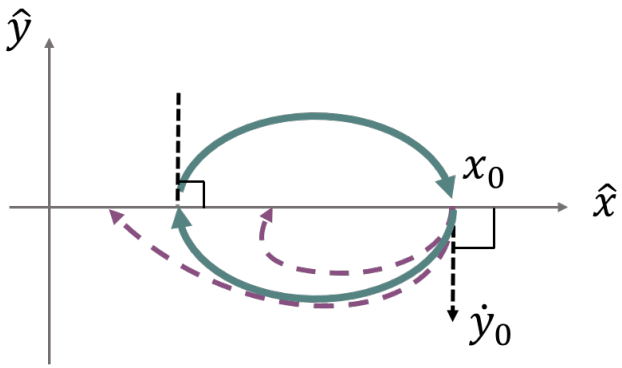

Figure 3.3. Representation of targeting a planar perpendicular crossing. The purple dashed curves represent trajectories that are perpendicular at one crossing of the plane, but not the other.

a single-shooting targeter, the design variable vector, $\vec{X}$, and the constraint vector, $\vec{F}(\vec{X})$, are defined as

$$\vec{X} = \begin{bmatrix} x_0 \\ \dot{y}_0 \\ \tau \end{bmatrix} \quad \text{and} \quad \vec{F}(\vec{X}) = \begin{bmatrix} y_f \\ \dot{x}_f \end{bmatrix} = \vec{0}. \tag{3.25}$$

The Jacobian matrix is then comprised of STM elements and partials with respect to time,

$$\mathbf{DF} = \begin{bmatrix} \Phi_{2,1} & \Phi_{2,5} & \dot{y}_f \\ \Phi_{4,1} & \Phi_{4,5} & \ddot{x}_f \end{bmatrix}. \tag{3.26}$$

There is an infinite number of solutions to the update equation, thus the minimum-norm solution is selected. It can be useful to remove some variables from the design variable vector, either to deliver a square Jacobian matrix or to fix a component of $\vec{X}$. For example, such a strategy can deliver an orbit with an exact period or a trajectory that crosses the xz-plane at a specific x value. The targeting scheme is also easily modified to determine a non-planar periodic trajectory by adding z_0 to the design variable vector and adding $\dot{z}_f = 0$ to the constraint vector. For a good initial guess, the targeter converges in a small number of iterations, but the convergence rate also

depends upon the dynamical sensitivities in the region of interest and the path of the trajectory through space. Successful convergence benefits from the perpendicular crossing approach because the integration time required to deliver sufficient initial conditions is half that of the actual orbital period, leading to a smaller buildup of numerical error.

3.2.4 Computing Periodic Orbits by Exploiting Periodicity

Targeters that construct a periodic orbit by means of periodicity constrain the final state vector at the end of some propagation time to be equal to the initial state vector. They are particularly useful for orbits that do not exhibit symmetry or orbits whose initial state is defined at a location that is not a perpendicular crossing. The design variable vector typically includes all six state elements, as well as the propagation time. The constraint vector is defined as the difference between the final state and the initial state, however, due to the implicit constraint imposed by the existence of the Jacobi integral, the continuity constraint vector only includes five of the six state elements. Thus, the design variable vector and the constraint vector have the form

$$\vec{X} = \begin{bmatrix} x_0 \\ y_0 \\ z_0 \\ \dot{x}_0 \\ \dot{y}_0 \\ \dot{z}_0 \\ \tau \end{bmatrix} \quad \text{and} \quad \vec{F}(\vec{X}) = \begin{bmatrix} x_f - x_0 \\ z_f - z_0 \\ \dot{x}_f - \dot{x}_0 \\ \dot{y}_f - \dot{y}_0 \\ \dot{z}_f - \dot{z}_0 \end{bmatrix} = \vec{0}. \tag{3.27}$$

Notice that $\vec{F}(\vec{X})$ omitted the y-position continuity constraint, but any of the six state elements could be omitted instead. Sometimes it is desired to add a phasing condition to the constraints as well, for example $y_f = 0$. This ensures that the initial states of every orbit are on the same plane (useful for plotting parameter curves).

3.3 Continuation Schemes

Targeting schemes enable the construction of trajectory arcs that deliver some specified behavior. However, a targeting scheme only delivers a single solution that satisfies the constraints. Originating with a single converged solution, continuation methods deliver a *range* of similar solutions that also meet the constraints, putting the original solution into a larger context. The set of solutions that emerge from this process are typically labelled a "family." Examples of such families include periodic orbits, quasi-periodic orbits, and transfers. Families of such solutions span a range of characteristics, offering a broader understanding of the dynamical environment. There are numerous approaches to develop such families, but this analysis employs two techniques in particular: natural parameter continuation and pseudo-arclength continuation.

3.3.1 Natural Parameter Continuation

Natural parameter continuation (NPC) is a straight-forward and intuitive approach to compute a family of solutions. The process is initiated with some converged solution from a single-shooting or multiple-shooting algorithm. The next solution is initialized by perturbing or varying a parameter assocaited with the converged solution. The initial guess for the perturbed solution is then converged to meet the constraints via a targeter, and this new converged solution then initializes the next solution. This process is repeated for a specified number of iterations. The resulting family evolves smoothly, and the evolution of its properties are examined to select an appropriate trajectory.

Many parameters are typically available for a continuation scheme, such as a position component, a velocity component, period, energy level, or even the mass parameter μ of the system, but *a priori* knowledge of the family of interest can simplify the selection. Such knowledge is especially useful when the curve of the stepping parameter suddenly increases in slope or reaches a cusp. Decreasing the

step size is helpful in such cases, but switching parameters is also a viable option. A "single-parameter family"— that is, for any given value of the stepping parameter, there is only *one* member of the family that exists—is often the most insightful. As an example of the NPC process, a portion of the single-parameter L_1 Lyapunov family in the Earth-Moon system is constructed. Members of this family are centered about the L_1 equilibrium point, are planar, and are periodic.

The continuation process requires a single periodic Lyapunov orbit, which is then used to initialize the continuation process. First, define the initial guess of the i-th family member to be $\vec{x}_{i,0}$ with half-period $\tau_{i,0}$, and the converged solution to be $\vec{x}_{i,*}$ with half-period $\tau_{i,*}$. Note the "half-period" refers to the integration time between the two perpendicular crossings. The resulting orbit possesses period 2τ. The initial state vector has the form

$$\vec{x}_{0,0} = \begin{bmatrix} x_{0,0} & 0 & 0 & 0 & \dot{y}_{0,0} & 0 \end{bmatrix}.$$

Then, with $\vec{x}_{0,0}$ as the initial guess for the first family member, a single-shooter delivers two perpendicular crossing by adjusting the initial y-velocity and the time of flight, $\tau_{0,0}$, while holding the initial x-position fixed. The design variable vector, constraint vector, and Jacobian then yield the following general form for every family member,

$$\vec{X} = \begin{bmatrix} \dot{y}_0 \\ \tau \end{bmatrix} \quad \vec{F}(\vec{X}) = \begin{bmatrix} y_f \\ \dot{x}_f \end{bmatrix} = \vec{0} \quad \mathbf{DF} = \begin{bmatrix} \Phi_{2,5} & \dot{y}_f \\ \Phi_{4,5} & \ddot{x}_f \end{bmatrix}.$$

An initial guess and a converged periodic orbit appear in Figure 3.4, with the values of $x_{0,*}$, $\dot{y}_{0,*}$, and period presented in Table 3.1. Recall that x is measured relative

Table 3.1. Parameters defining the initial member of the L_1 Lyapunov family in the Earth-Moon system.

$x_{0,*}$ [km]	$\dot{y}_{0,*}$ [km/s]	$2\tau_{0,*}$ [days]
$325,586$	-0.0808	11.76

to the barycenter. The same targeter delivers the subsequent family members. Since

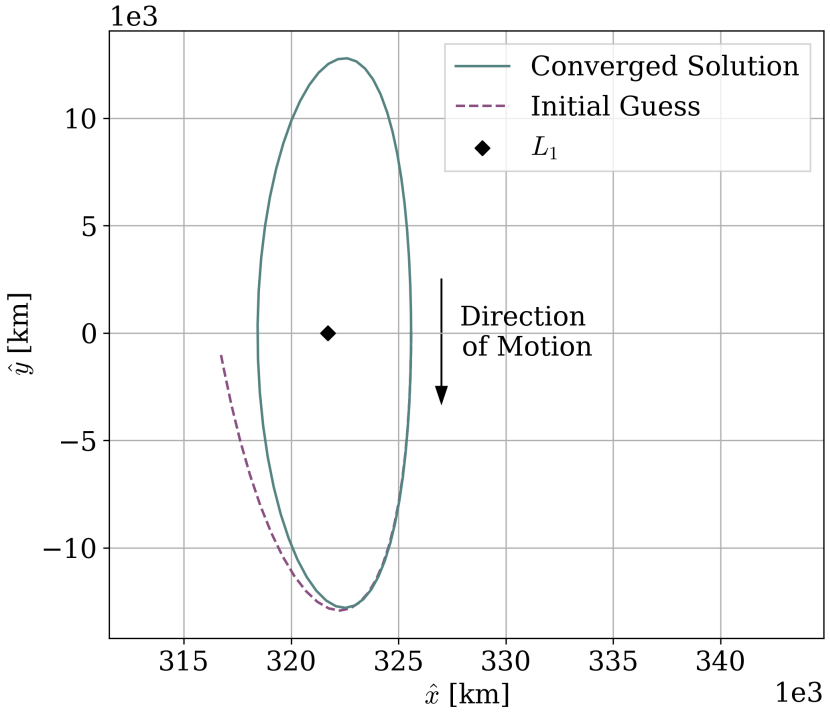

Figure 3.4. An L_1 Lyapunov orbit in the Earth-Moon system. The initial state is on the right side of the equilibrium point and on the x-axis, with initial velocity in the negative $\hat{y}$ direction.

the initial state of this first orbit is defined to the right of the equilibrium point, the continuation process proceeds along the $\hat{x}$-axis with positive increments in the x value of the initial state. Denote this increment with the symbol δx. The initial state for the next solution is then defined with the incremented x value and the initial y velocity of the previous converged solution. Similarly, the initial guess for the period is the period of the previous solution. Selection of an appropriate increment size is a key factor. Small values will evolve the family slowly, but large values can lead to a poor initial guess. In this example, a step size equal to $\delta x = 0.001$ in nondimensional units is successful, which is equal to approximately 384 km. The continuation process

quickly delivers 60 new members of the Lyapunov family, 20 of which are plotted in Figure 3.5 for clarity.

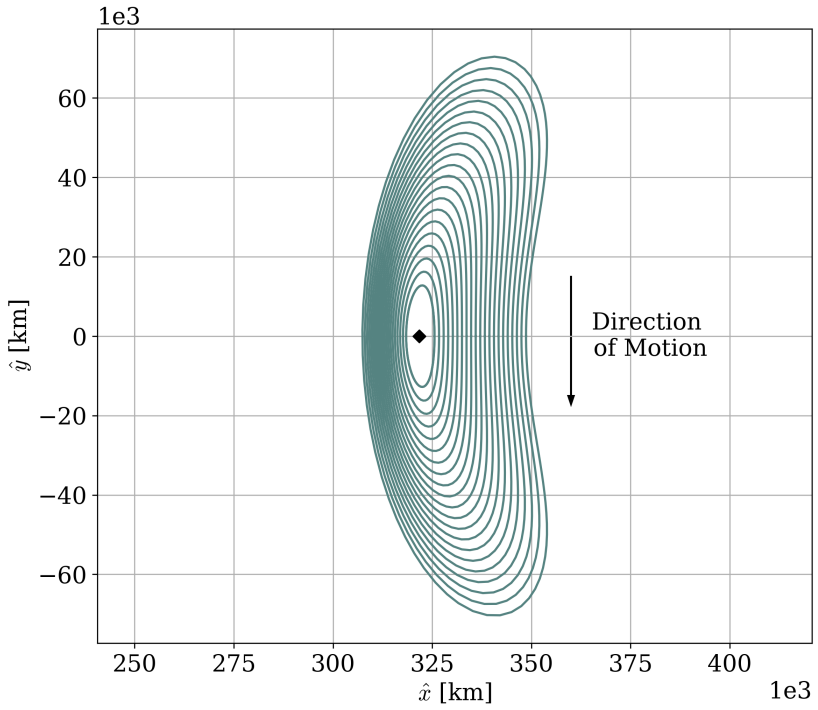

Figure 3.5. Members of the L_1 Lyapunov family. The black diamond at the center is the equilibrium point.

3.3.2 Pseudo-arclength Continuation

While natural parameter continuation is intuitive and easy to implement, it is sometimes less robust to numerical difficulties than some other techniques and often requires prior knowledge of the evolution of a family. An alternative is pseudo-arclength continuation (PAC). Similar to natural parameter continuation, pseudo-arclength continuation uses the previous solution to inform the initial guess for the next periodic orbit, however, PAC uses a different stepping method. The step implemented by PAC, denoted Δs, simultaneously updates *all* elements of the free variable

vector for the next solution. A PAC scheme ensures that this step is in the direction of the next family member by leveraging the Jacobian matrix of the previous solution, ensuring that no prior knowledge of the evolution of the family is required. Thus, PAC is more robust to sudden slope changes and turning points along the parameter curve; it can accommodate larger step sizes and require fewer iterations of the targeter for complex continuation paths. However, PAC schemes are more difficult to implement and, because PAC steps represent a nonphysical parameter, the process is less intuitive and harder to troubleshoot. A graphical comparison of the two methods appears in Figure 3.6.

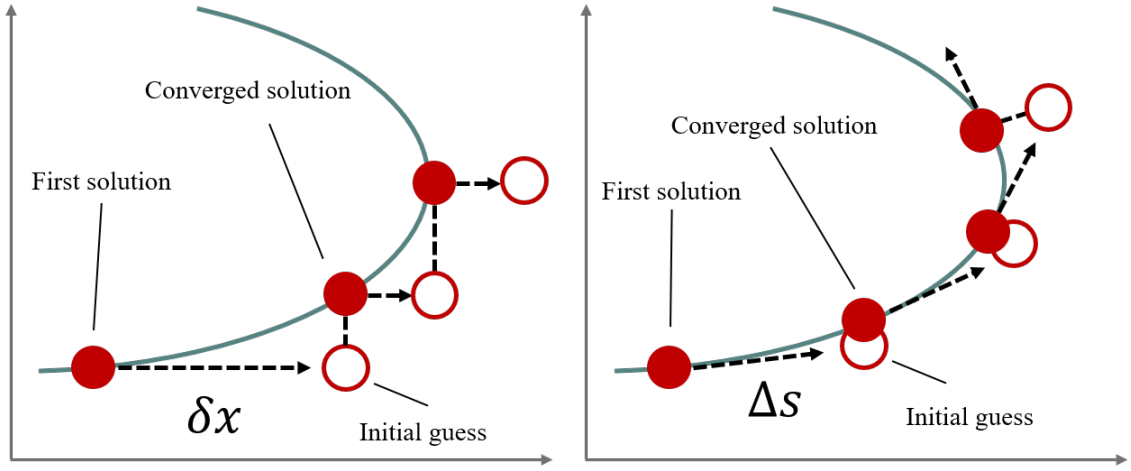

(a) Natural parameter continuation (b) Pseudo-arclength continuation

Figure 3.6. Diagram comparing the continuation processes for an arbitrary parameter curve with a turning point. The NPC process requires extra logic to alter its search direction. The PAC approach follows the solution curve around the turning point.

Pseudo-arclength continuation is, in essence, based upon a predictor-corrector strategy leveraging the observation that arclength is the ideal parameterization of a curve. The prediction stage employs the previous solution's Jacobian matrix to develop an update in the direction of the family; the correction stage uses a targeter to determine the exact initial conditions to produce a periodic orbit. The update in

the direction of the family is delivered by the null space of the Jacobian matrix, as vectors in the null space are tangent to the solution space of the family members. Define the previously converged solution by its free variable vector $\vec{X}_{*,i}$, such that $\vec{F}(\vec{X}_{*,i}) = \vec{0}$. The Jacobian matrix for this solution is $\mathbf{DF}(\vec{X}_{*,i})$. The initial guess for the next solution is then defined

$$\vec{X}_{0,i+1} = \vec{X}_{*,i} + s\Delta\vec{X}_{*,i}, \tag{3.28}$$

where $\Delta\vec{X}_{*,i}$, is the null space of the previously-converged Jacobian matrix, $\Delta\vec{X}_{*,i} = \mathcal{N}(\mathbf{DF}(\vec{X}_{*,i}))$, and s is a scaling factor. This new initial guess is corrected to yield a periodic orbit, but the targeting scheme requires some augmentation. An additional constraint is appended to the original constraint vector. This tangent constraint is expressed

$$F_{PAC} = (\vec{X}_{i+1} - \vec{X}_{*,i})^T \Delta\vec{X}_{*,i} - s = 0, \tag{3.29}$$

and ensures that the next solution is shifted along the tangent vector of the family. The augmented constraint vector then has the form

$$\vec{G}(\vec{X}_{i+1}) = \begin{bmatrix} \vec{F}(\vec{X}_{i+1}) \\ F_{PAC} \end{bmatrix} = \vec{0}. \tag{3.30}$$

The partial derivative of F_{PAC} with respect to $\vec{X}_{i+1}$ is available analytically, as the terms $\vec{X}_{*,i}$, $\Delta\vec{X}_{*,i}$, and s are all constant. Thus, the augmented Jacobian is

$$\mathbf{DG}(\vec{X}_{i+1}) = \begin{bmatrix} \mathbf{DF}(\vec{X}_{i+1}) \\ \Delta\vec{X}_{*,i}^T \end{bmatrix}. \tag{3.31}$$

Throughout this process, it is assumed that the previously-converged Jacobian possesses a one-dimensional null space. This condition can be achieved by properly framing the targeter that delivers the first member of the family. Because of numerical difficulties associated with null space computation, successful family generation using PAC sometimes requires extra control logic.

To demonstrate the capabilities of PAC, consider the L_2 southern halo orbit family. Leveraging a three-dimensional perpendicular crossing targeter to correct each initial guess, the free variable and constraint vectors have the form

$$\vec{X} = \begin{bmatrix} x_0 \\ z_0 \\ \dot{y} \\ \tau \end{bmatrix}, \quad \vec{F}(\vec{X}) = \begin{bmatrix} y_f \\ \dot{x}_f \\ \dot{z}_f \end{bmatrix} = \vec{0}. \tag{3.32}$$

The results are plotted in Figure 3.7. The first family member, used to initialize the continuation process, is the orbit with the closest passage to the Moon. In this formulation, four parameters are allowed to vary during the continuation process. A natural parameter continuation is also successful by varying any one of these parameters, but some of the parameter curves are non-monotonic, so the NPC scheme requires extra logic to deliver the entire family. By contrast, the PAC scheme is constrained to automatically step the parameters in $\vec{X}$ along the vector tangent to the family without any switching logic. The non-monotonic nature of the L_2 southern halo family parameter curves is evident in Figure 3.8. The evolution of the curve in Figure 3.8(a) begins with x_0 slightly decreasing for an increase in z_0 (left-most point of the curve); the slope of the curve continues to evolve significantly across the entire family. Thus, an NPC scheme requires logic to modify the sign and step size for x_0. The right frame of the figure demonstrates that the same requirements emerge if using z_0 as the stepping parameter. Orbits along the L_2 southern butterfly family are also plotted for reference in Figure 3.9. Targeting members of the butterfly family also benefits from the more robust nature of the pseudo-arclength continuation algorithm.

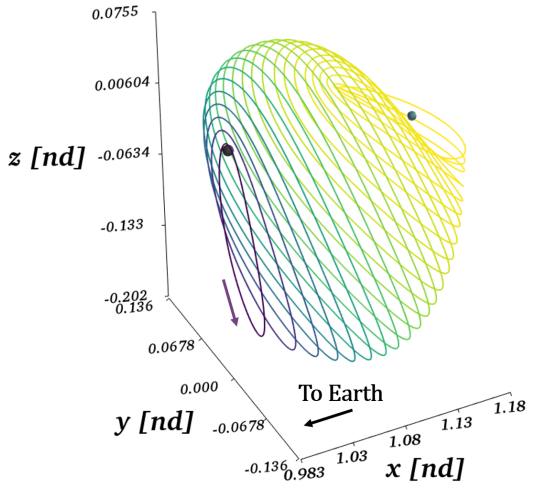

(a)

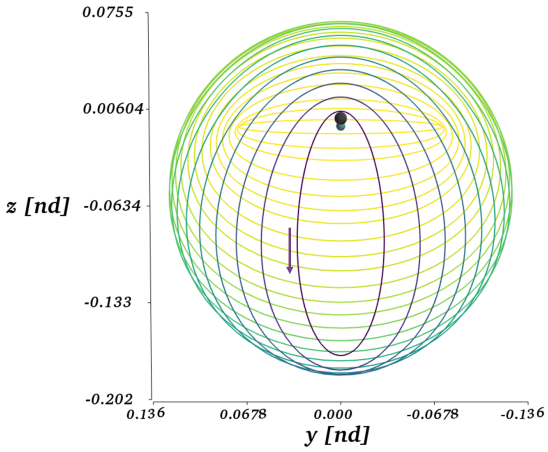

(b) View along $+x$-axis

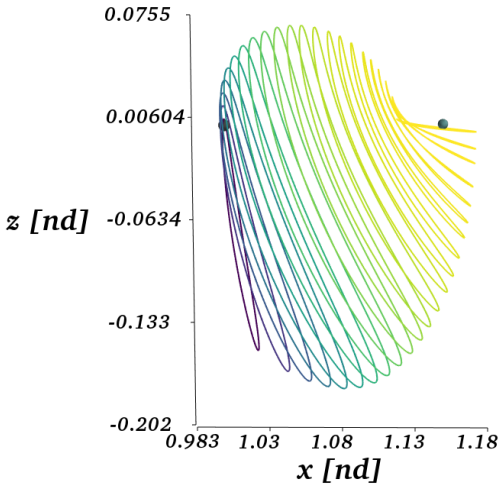

(c) View along $+y$-axis

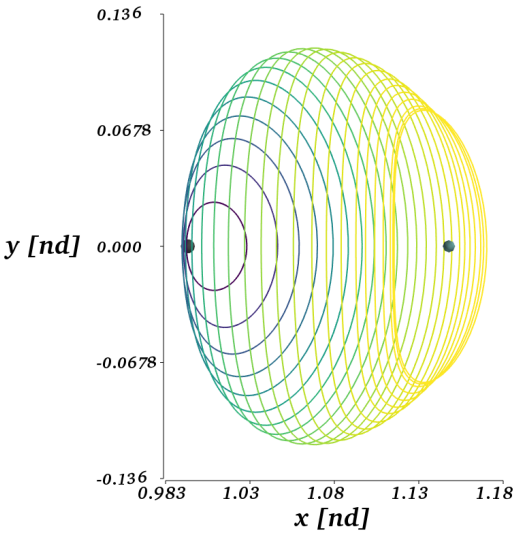

(d) View along $-z$-axis

Figure 3.7. Projections of L_2 southern halo family members. Orbits are colored by period, ranging from approximately 6 days (purple) to approximately 15 days (yellow). The Moon appears as the gray sphere, surrounded by mostly purple orbits, and L_2 is represented by the pale green sphere, surrounded by mostly yellow orbits.

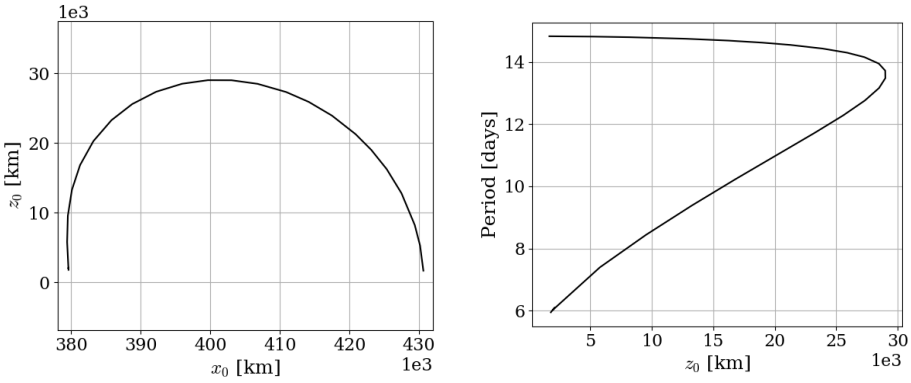

(a) (b)

Figure 3.8. Parameter curves of the L_2 southern halo family. The left frame illustrates the initial x and z positions for each family member in Figure 3.7, while in the right frame the orbit periods are plotted against the initial z position.

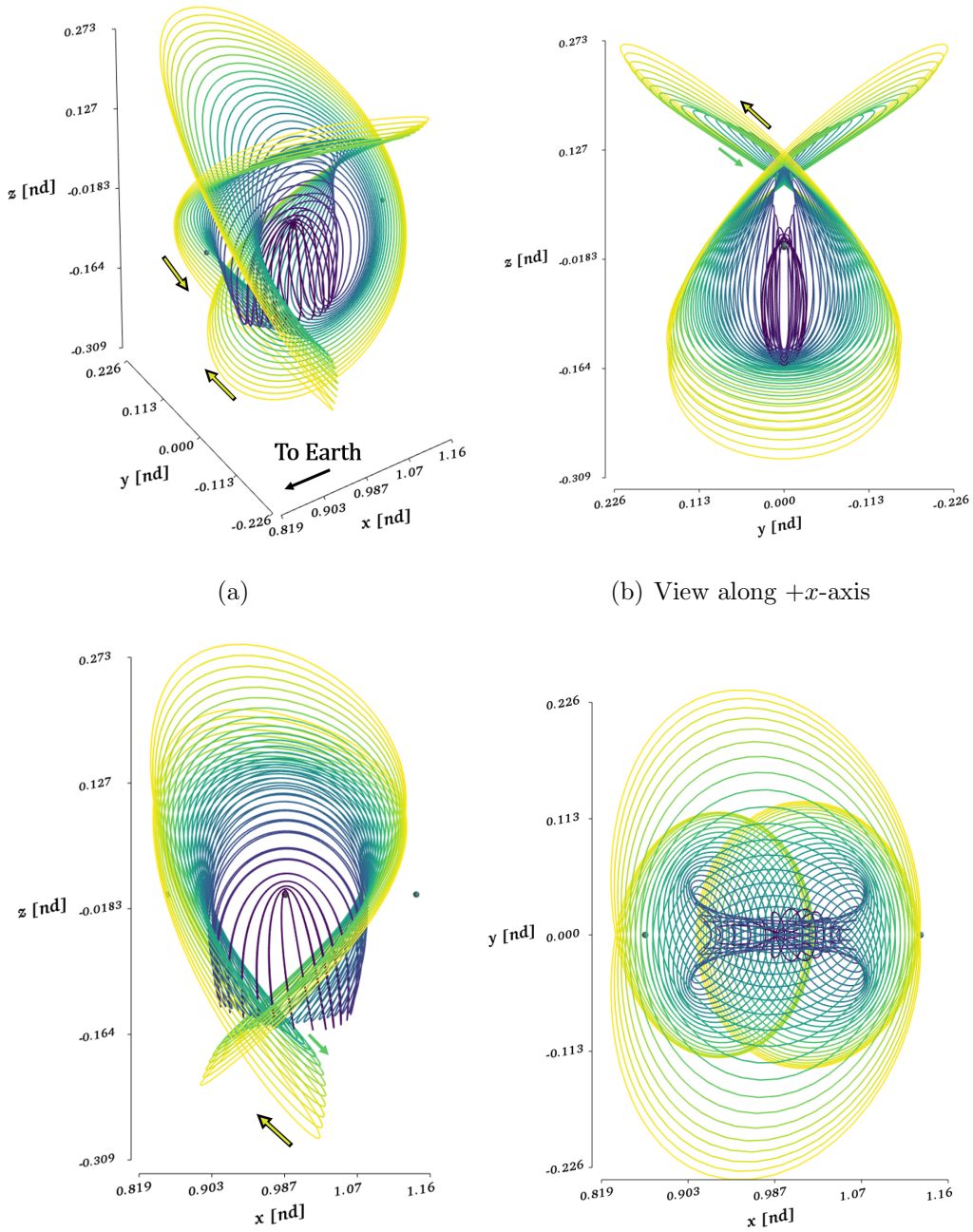

(a)

(b) View along $+x$-axis

(c) View along $+y$-axis

(d) View along $-z$-axis

Figure 3.9. Projections of L_2 southern butterfly family members. Orbits are colored by period, ranging from approximately 12 days (purple) to approximately 44 days (yellow). The Moon appears as the gray sphere, surrounded by mostly purple orbits. L_1 and L_2 are represented by the pale green spheres.

4. DYNAMICAL SYSTEMS THEORY

Dynamical systems theory delivers insight into the complex, chaotic, nonlinear solution space of the CRTBP. Applications of dynamical systems theory aid in analysis as well as mission design. Such applications critical to this investigation include stability analysis, Poincaré maps, invariant manifolds, and bifurcation theory.

4.1 Periodic Orbit Stability

The stability of an orbit is an important consideration in mission design. There are various methods of assessing stability for periodic orbits; a straightforward approach used in this work examines the characteristics of the monodromy matrix. The monodromy matrix, $\mathbf{M}$, is defined as the state transition matrix corresponding to a fixed point (periodic orbit) evaluated after precisely one orbital period. It is represented mathematically as

$$\mathbf{M} = \Phi(t_0 + T, t_0), \tag{4.1}$$

where T is the period of the orbit. The monodromy matrix is a stroboscopic map reducing the continuous time system to a discrete time system. Stability information is determined, in a linear sense, from the eigenvalues of the monodromy matrix, denoted λ_i. Because the monodromy matrix is a discrete mapping, the stability boundary is the unit circle, such that

$$||\lambda_i|| = \begin{cases} < 1 & \text{stable,} \\ = 1 & \text{center,} \\ > 1 & \text{unstable.} \end{cases}$$

The eigenstructure of the monodromy matrix is then described by Lyapunov's theorem [34, 36]: if λ is an eigenvalue of a periodic orbit in a time-invariant system, so

is λ^{-1}. Further, the spectrum of $\mathbf{M}$ is symmetric with respect to the real axis and unit circle. Therefore, eigenvalues that are real occur in reciprocal pairs, and complex eigenvalues occur in conjugate pairs.

The stable, unstable, and center modes associated with the subspaces from the monodromy matrix govern the nature of a periodic orbit. Stability analysis of the solution space of the linear dynamical system is thus subdivided into three fundamental subspaces:

- The stable subspace, E^S, with dimension n_S,
- The unstable subspace, E^U, with dimension n_U,
- And the center subspace, E^C, with dimension n_C.

The total dimension of the solution space is then the sum of the dimensions of each subspace, $n_S + n_U + n_C$. The basis of each subspace is defined by the eigenvectors associated with the corresponding eigenvalues. Because the eigenvalues of $\mathbf{M}$ always occur in reciprocal pairs, an unstable eigenvalue always implies a corresponding stable eigenvalue. Thus, the dimension of the unstable subspace is always equal to the dimension of the stable subspace, $n_U = n_S$. Further, because orbit periodicity guarantees a unity eigenvalue, the center subspace must exist with a dimension that is always a multiple of two: $n_C \geq 2$. For the current application, there are two unity eigenvalues, denoted the trivial pair. As noted, one of the eigenvalues of the trivial pair indicates periodicity, so the corresponding eigenvector is directed along the orbit. The second unity eigenvalue reflects the fact that the orbit is a member of a family of related solutions; the corresponding eigenvector points along the family. The remaining nontrivial eigenvalues are then used to assess the stability of an orbit. Perturbations along the unstable direction, indicated by the corresponding unstable eigenvector, diverge relative to the orbit, while perturbations in the stable direction asymptotically approach the fixed point (this behavior is straightforwardly understood within the context of Poincaré maps). The larger the magnitude of an unstable eigenvalue, the faster a perturbation in that direction expands. The eigenstructure

of a periodic orbit indicates the nature of the underlying motion in its vicinity. Further, changes in the eigenstructure along a family indicate changes in the qualitative behavior of the family, as well as the potential existence of a new family of solutions. The point at which the eigenstructure changes is a *bifurcation*.

4.1.1 Broucke Stability Diagram

Roger Broucke's stability diagram is a useful tool for investigating the evolution of stability along a family of solutions [37]. Each region in the diagram corresponds to a unique stability mode. Crossing any of the boundaries that separate each region corresponds to a distinct eigenstructure change, identifed as a bifurcation. In contrast to other stability metrics, the Broucke stability diagram captures the relevant stability information with no loss of insight.

Building the Broucke stability diagram is straightforward. The monodromy matrix $\mathbf{M}$ is real and symplectic, so the characteristic equation,

$$\det\left(\mathbf{M} - \lambda\mathbf{I}\right) = 0, \tag{4.2}$$

delivers a 4th order form of the characteristic equation, that is,

$$\mathrm{P}(\lambda) = \lambda^4 + A\lambda^3 + B\lambda^2 + A\lambda + 1 = 0, \tag{4.3}$$

where A and B are real coefficients and the trivial pair of eigenvalues at $\lambda = 1$ are factored out. It is possible to demonstrate that the four nontrivial eigenvalues are uniquely determined by the coefficients A and B. The derivation is summarized by Grebow [38]. The resulting relationships are

$$A = 2 - \mathrm{Tr}(\mathbf{M}), \tag{4.4}$$

$$B = \frac{1}{2}\left(A^2 + 2 - \mathrm{Tr}(\mathbf{M}^2)\right), \tag{4.5}$$

where $\mathrm{Tr}(\cdot)$ denotes the trace of a matrix. Because the eigenvalues of the monodromy matrix determine the stability properties of a periodic orbit, and because the coefficients A and B uniquely determine the nontrivial eigenvalues, A and B alone deliver stability information.

The stability boundaries are, thus, defined by relationships between A and B. From Equation (4.3), consider the points $\mathrm{P}(\lambda) = 0$ for $\lambda = 1$ and $\lambda = -1$. These eigenvalues correspond to two linear relationships between A and B:

$$B = -2A - 2, \tag{4.6}$$

and

$$B = 2A - 2, \tag{4.7}$$

respectively. A third boundary denotes the region where the eigenvalues are complex and off the unit circle, reflected in the quadratic relationship

$$B = \frac{A^2}{4} + 2. \tag{4.8}$$

The relationships in Equation (4.6) and Equation (4.7) represent two lines with slopes ± 2 intersecting each other at the point $(A,\, B) = (0,\, -2)$. The quadratic relationship in Equation (4.8) represents a parabola tangent to these lines at $(A,\, B) = (\pm 4,\, 6)$ opening in the positive B direction with apex at $(A,\, B) = (0,\, 2)$. These three curves define seven distinct stability regions in which the eigenstructure of the monodromy matrix is unique. The stability diagram with the representative eigenstructures for each region appear in Figure 4.1, recreated from Campbell[1] [39] and Grebow [38].

4.1.2 Stability Index

The stability index offers an alternative representation of stability, but still employs the eigenvalues of the monodromy matrix. Each nontrivial pair of eigenvalues is combined into a single metric to describe the stability of the corresponding modes. One of the benefits of this formulation is that it views the evolution of stability with respect to a natural parameter, perhaps a more intuitive metric. Further, this strategy combines information from four eigenvalues (which may or may not be complex) into

[1]Note, Campbell [39] and Grebow [38] use slightly different formulations for A and B. The current approach is consistent with Grebow.

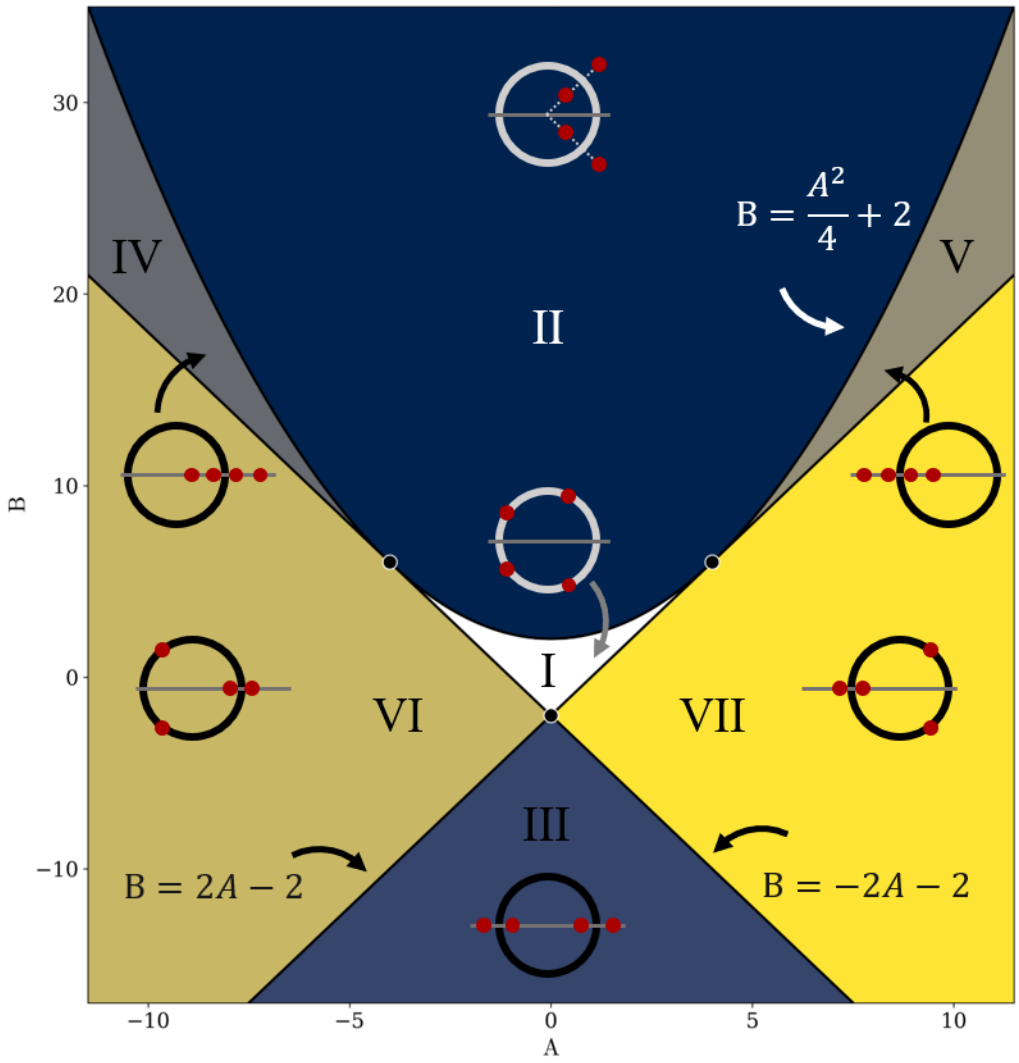

Figure 4.1. Broucke Stability Diagram.

two scalars. Plotting the evolution of these scalars allows for straightforward identification of interesting stability characteristics, as well as simple comparisons of relative stability. Although there are many ways of combining the reciprocal eigenvalues, this analysis employs the following definition for a stability index, ν_i:

$$\nu_i = \frac{1}{2}(\lambda_i + \lambda_i^{-1}) \tag{4.9}$$

for $i = 1, 2$. A sample plot of the stability indices for members of the L_2 southern halo family appear in Figure 4.2. The black lines at ± 1 indicate stability boundaries.

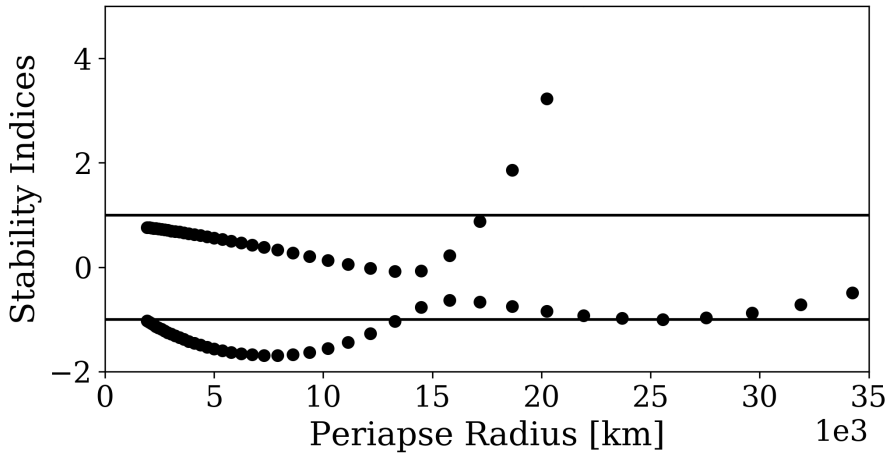

Figure 4.2. Stability index for members of the L_2 southern halo family.

Orbits with *both* stability indices possessing magnitude less than or equal to unity are stable in a linear sense. Larger magnitudes of stability index indicate faster departure from the vicinity of the periodic orbit. Thus, station-keeping costs tend to be lower for orbits with a smaller stability index, and transfer costs are higher [38]. Furthermore, in general, the stability index tends to grow as the distance from the Moon increases [31].

4.1.3 An Alternative Definition of Stability Index

As defined in Equation (4.9), the stability index offers simple stability information for periodic orbits when the nontrivial eigenvalues are real or, if complex, on the unit circle. For complex eigenvalues with unity magnitude (i.e., on the unit circle), the stability index is a real-valued scalar; the inverse of a unit-magnitude complex number is simply the conjugate, resulting in cancellation of the imaginary components in Equation (4.9). When the eigenvalues are complex and *not* on the unit circle, the definition of ν_i no longer results in a real-valued number. Thus, plotting the complex values of stability index requires an extra dimension, or plotting only the real part or complex parts independently. The former adds complexity and the latter does not

accurately represent the stability behavior. Because many members of the butterfly family possess complex eigenvalues off the unit circle, it is necessary to introduce an alternative definition of the stability index.

A different formulation for the stability index captures the full implications of complex eigenvalues off of the unit circle. One alternative form of stability index, denoted ς_i, is used successfully in this investigation, i.e.,

$$\varsigma_i = \frac{1}{2}(||\lambda_i|| + ||\lambda_i||^{-1}), \tag{4.10}$$

for $i = 1, 2$. The value of this alternative stability index is real with magnitude ≥ 1. Notice that some information is lost, for example, the sign of the eigenvalues. The stability indices in Figure 4.2 are all either real or on the unit circle, so the definition in Equation (4.9) fully captures the stability behavior and the alternative definition is not necessary. However, for the sake of comparison, Figure 4.2 is recreated using the new definition of stability index in Figure 4.3. While the same basic stability information remains, the alternative stability index definition does not capture the evolution of the unit-magnitude complex eigenvalues to the same detail.

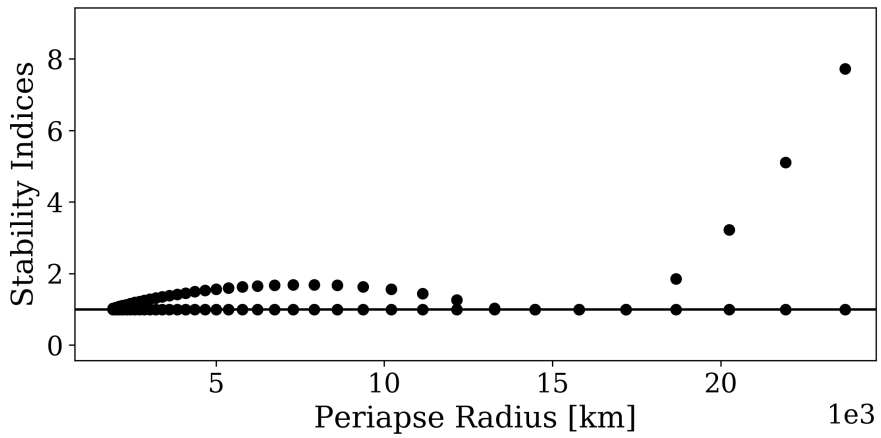

Figure 4.3. Alternative stability index for members of the L_2 southern halo family.

To demonstrate the benefits of the alternative stability index, consider the butterfly family. For comparison, both definitions of the stability index for a subset of the L_2 southern butterfly family are plotted in Figure 4.4. The stability index in

Figure 4.4(a) plots only the real part of any complex values. Notice that, beyond a perilune radius of 30,000 km, the curve in Figure 4.4(a) crosses the x-axis twice. The sections of this curve between ± 1 indicate stable behavior, however, consulting Figure 4.4(b), the actual magnitudes of the eigenvalues are such that the orbit is unstable at these points. Further, the curve in Figure 4.4(b) better reflects the magnitude of instability over the family, as it does not oscillate about the x-axis, but increases for most of the plotted history. Since the magnitude of the stability index is indicative of the rate of departure, Figure 4.4(a) is misleading.

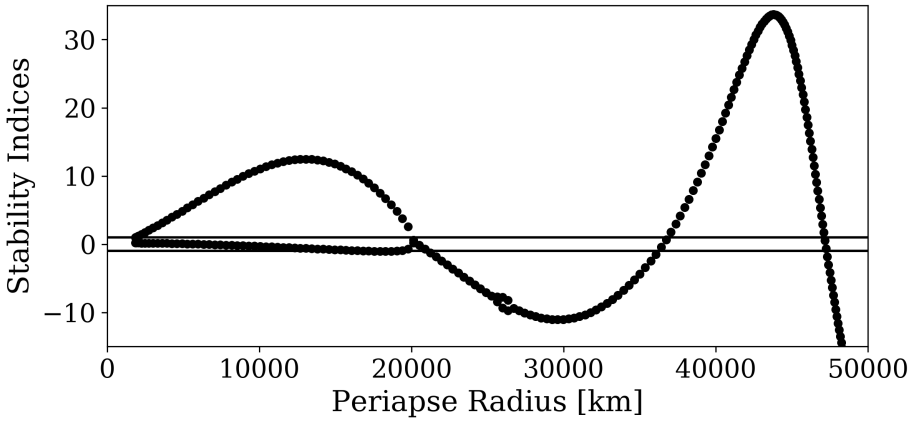

(a) Original stability index

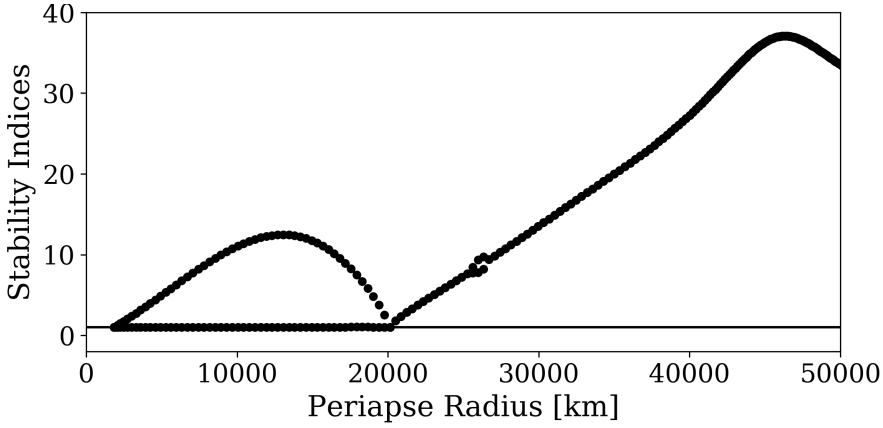

(b) Alternative stability index

Figure 4.4. Comparison of stability index definitions.

4.2 Poincaré Maps

Generally, reducing a continuous time system—a flow—to an associated discrete time system offers some distinct advantages; one strategy is the construction of a map. First, using a map, the dimensionality of the problem is reduced by one, reducing the complexity of the design space. Also, the visual nature of a map allows for the comparison of many trajectories within a specified region simultaneously, and offers visual inspection of the flow qualities; identification of any geometrical patterns in a map informs knowledge of the underlying dynamical structures. Poincaré maps are constructed from a smooth surface of section (or hyperplane, Σ) transverse to the flow. Points at which the flow crosses the hyperplane are recorded and plotted. The hyperplane can be constructed geometrically, i.e., defining a physical plane (such as the x-y plane), or created employing characteristic properties (such as periapse occurrences [40–42]). Poincaré maps preserve both periodicity and stability information; on a map, a periodic orbit is denoted as a fixed point, because every piercing of the hyperplane occurs at the same geometrical location. A schematic representing a fixed point in a low-dimensional system appears in Figure 4.5. The 2-D periodic orbit, Γ^*, returns to the same point on the map after every revolution, i.e., the fixed point. A nearby trajectory, Γ_0, does not return to the same point; its initial position on the map is denoted x_0, and its first return is denoted $P(x_0)$. Typically, maps on a hyperplane are further constrained by filtering crossings based on a specified property, such as direction. Maps that include crossings of the hyperplane in both directions are denoted two-sided maps, while those that incorporate crossings in only one direction are labelled one-sided maps. A simple illustration appears in Figure 4.6. A positive one-sided map is defined as the collection of points, $A = \{x_1, x_3, x_5\}$, a negative one-sided map is the collection, $B = \{x_2, x_4\}$, and the two-sided map is the set of all crossings, $A \cup B = \{x_1, x_2, x_3, x_4, x_5\}$. The concepts in Figure 4.5 and Figure 4.6 demonstrate some of the useful aspects of Poincaré maps. They also illustrate that effective Poincaré mapping techniques, especially in higher-dimensional

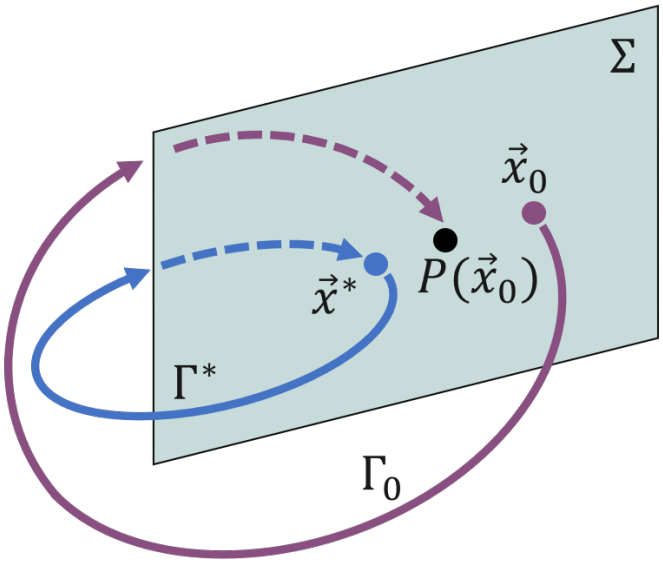

Figure 4.5. Example of an arbitrary Poincaré section showing a fixed point, x^*, corresponding to a periodic orbit Γ^*, and a nearby trajectory Γ_0 that is not periodic in time history shown.

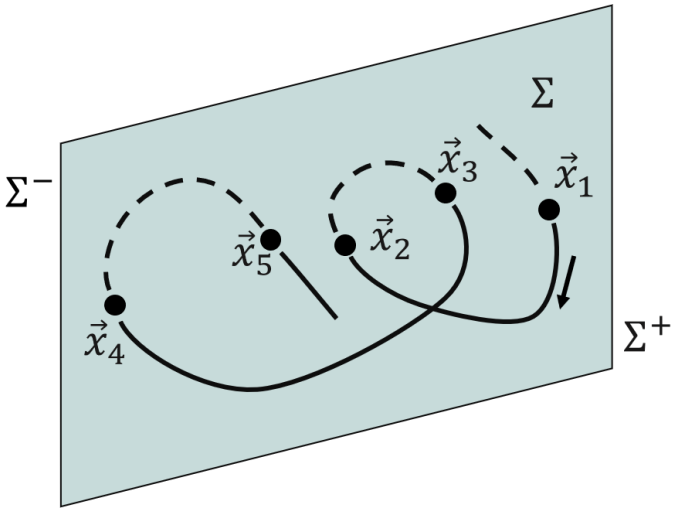

Figure 4.6. An example of a hyperplane with flow that crosses in two directions.

systems, require a deliberate selection of the hyperlane; prior knowledge of the flow is also often necessary to produce an informative map.

4.2.1 Poincaré Maps of Higher Dimension

The phase space associated with the differential equations in the CRTBP is six-dimensional, so conventional mapping techniques cannotfully represent the complex motion on a 2-D hyperplane. There are a number of available strategies, though, to add information to the maps for higher-dimensional flows. One of the simplest options is incorporating color or size variations to represent one extra dimension. This options allows quick identificaiton of a wide range of behavior, even in dense maps. However, precise, exact comparisons are not possible for individual data points by comparing color and/or size. Another option for incorporating higher dimensions is the use of glyphs. Glyphs, such as vectors representing state parameters, supply additional information for multiple dimensions simultaneously. Glyphs can also be stacked, or incorporate color and/or size variations. Too much information, though, clutters the plot and can obfuscate important features. Glyphs have been used to great effect by many previous authors within the context of the CRTBP [41, 43, 44]. This investigation incorporates both color and glyphs to aid in design. As an example, consider an arbitrary flow in the CRTBP given initial state vectors. Define a hyperplane at $z = 0$, propagate the initial state vectors, record crossings with the hyperplane, and plot the x and y position components of the crossings on the map. Assume interest in knowledge of the remaining remaining state components, $\dot{x}$, $\dot{y}$, and $\dot{z}$. Incorporate a vector glyph to represent $\dot{x}$ and $\dot{y}$, and apply a color map to the marker and glyph to represent $\dot{z}$. All six state components are represented on the map. A schematic of the glyphs is shown in Figure 4.7. Higher-dimensional Poincaré maps are particularly useful for construction of transfers between arcs: if two arcs, represented on a map such as Figure 4.7, possess similar x and y coordinates, similar vector directions and magnitude, and a similar color, it is likely that a low cost transfer exists between them.

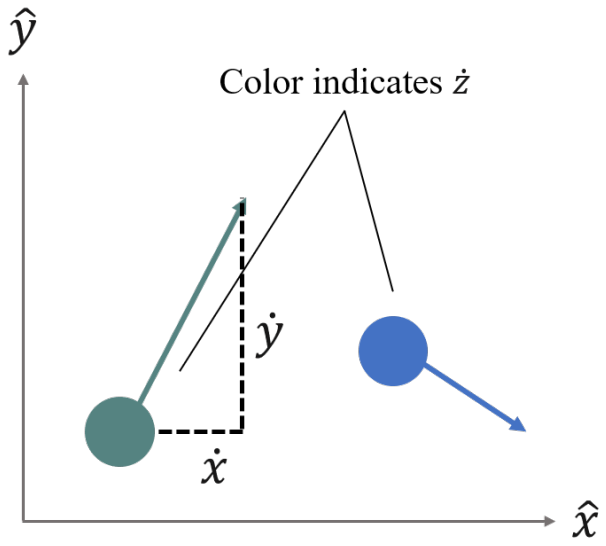

Figure 4.7. Sample crossings on a Poincaré map at $z = 0$. The combination of vector glyphs and color fully represents all six states.

4.2.2 Insights from Poincaré Maps

One of the most powerful features of Poincaré maps is their ability to display a large quantity of flow information succinctly. Dynamical structures in the six-dimensional flow are identified with relative easy by geometrical features in the map. Higher-dimensional maps potentially convey an even greater level of detail.

Consider an arbitrary member of the butterfly family with a perilune radius of 3,500 km. As an example, consider a scenario in which a spacecraft inserts into the butterfly orbit at a specific location or some subset of locations along the orbit. The butterfly orbit is plotted in Figure 4.8, with the candidate locations highlighted in red. One method for designing a transfer is the implementation of a range of maneuvers along this subset and propagate the resultant arcs backwards in time. By evaluating the state history along the resulting arcs, a candidate with desirable qualities (e.g., low maneuver cost, close approaches to a primary, or short time of flight) is selected. In this example, maneuvers of 10, 20, 30, 40, 50, and 60 m/s are applied in the velocity and anti-velocity directions at 200 evenly-spaced time intervals along the candidate

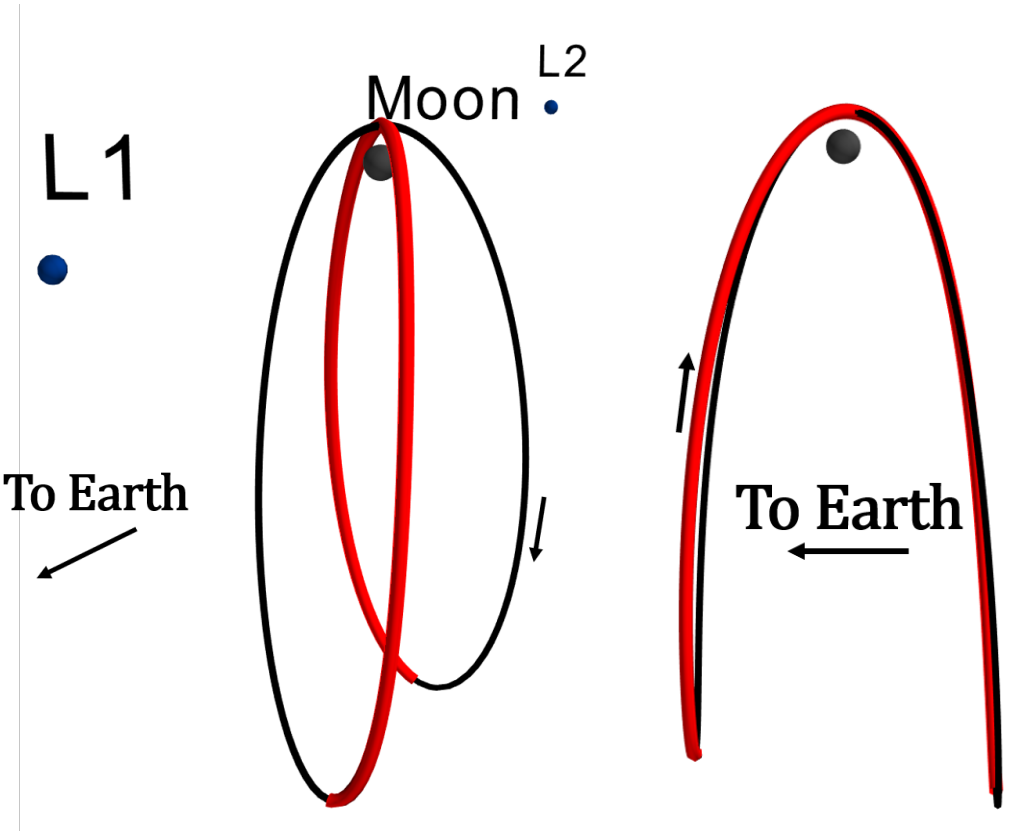

(a) Candidate Butterfly

(b) View along $+\hat{y}$ axis

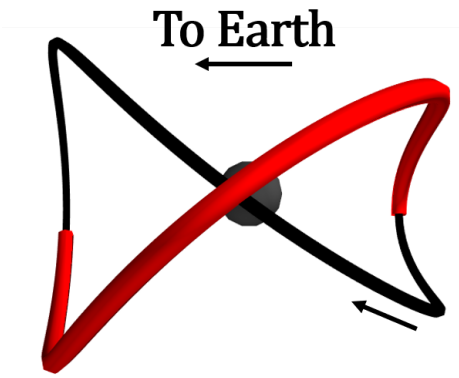

(c) View along $-\hat{z}$ axis

Figure 4.8. Butterfly orbit with periapse radius of 3,500 km. The red region indicates the possible arrival locations.

subset, resulting in 2,400 candidate transfer arcs. The trade space is large, so a Poincaré map is leveraged to offer insight into the resultant behavior. Choose a one-sided hyperplane at $z = 0$, plotting only the crossings with $\dot{z} < 0$. The one-sided map is displayed in Figure 4.9, zoomed into the vicinity near the Moon. There are multiple

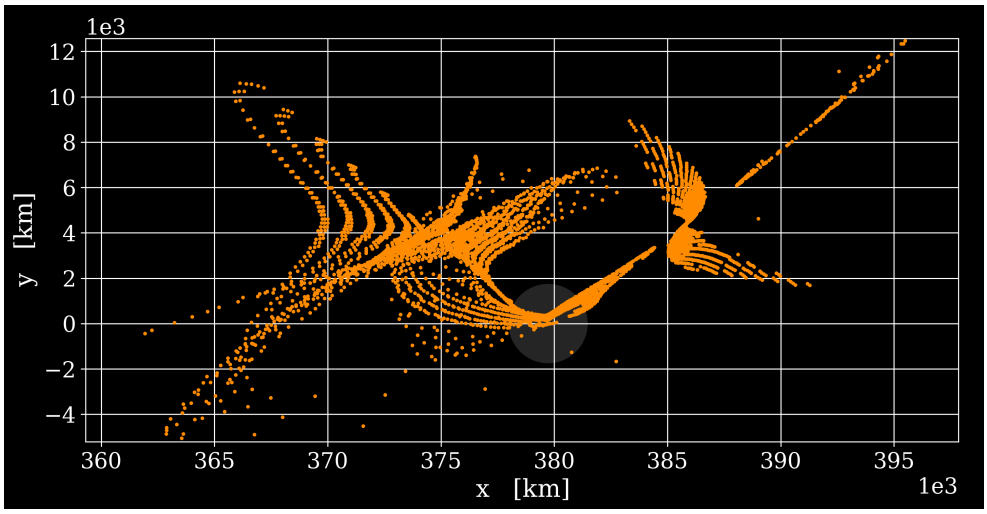

Figure 4.9. One-sided ($\dot{z} < 0$) Poincaré map at $z = 0$ for the candidate transfers. The dark gray circle near center is the Moon.

distinct regions on the map in Figure 4.9. Each region can be compared to identify motion of interest. First, consider a set of arcs from the bow-shaped structures at the upper-left of Figure 4.9, sets P and Q. The regions of interest are highlighted in Figure 4.10(a). Plotting some in each set illustrates that arcs within each set are more similar to each other than they are to arcs in the other set; while each set exists in a similar area of the map, they also exhibit unique behavior. Notice that there also appears to be a diagonal sepratrix in the evolution of the Poincaré map, indicated by the dashed white line in Figure 4.11(a). To compare, an arc is selected for plotting near the apex of each of the distinct bow-shaped curves in set R. The map is denser near set S, but similar structures exist, reflected across the sepratrix. Both sets are plotted in Figure 4.11(b) alongside the reference butterfly orbit. The dark blue arcs possess a perilune pass between the reference butterfly orbit and the

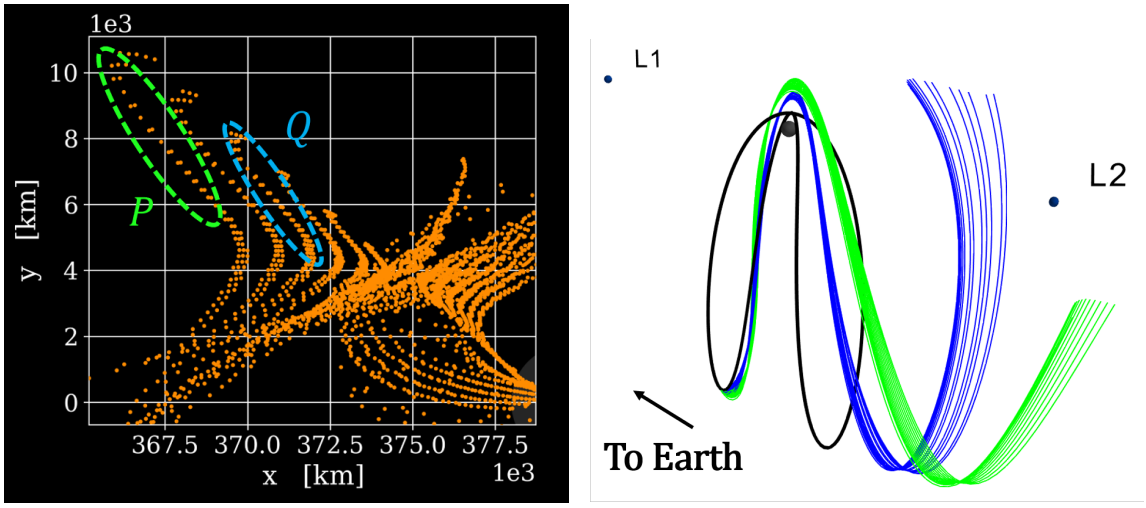

(a) Regions of interest

(b) Arcs of sets A and B

Figure 4.10. Comparison of two structures from the Poincaré map in Figure 4.9. The colors of the dashed circles in the left frame correspond to the colors of the orbits in the right frame. The reference butterfly is plotted in black.

lunar radius, while the light blue arcs possess a perilune pass at a higher altitude than the reference butterfly orbit. Notice that the butterfly orbit separates the flows of each set. More geometrical features of of the map could be explored to determine a desirable transfer, but this example serves to demonstrate the useful capabilities of Poincaré maps.

4.3 Invariant Manifolds

Invariant manifolds are dynamical structures representing the local and global flow associated with equilibrium points as well as periodic orbits. In this investigation, invariant manifolds associated with periodic orbits are leveraged to initiate low-cost transfers and to inform the type of motion that exists in their vicinity. The manifolds associated with a periodic orbit are directly dependant upon the orbit's stability modes. Consider a fixed point on a Poincaré map, $\vec{x}^*$, corresponding to a periodic

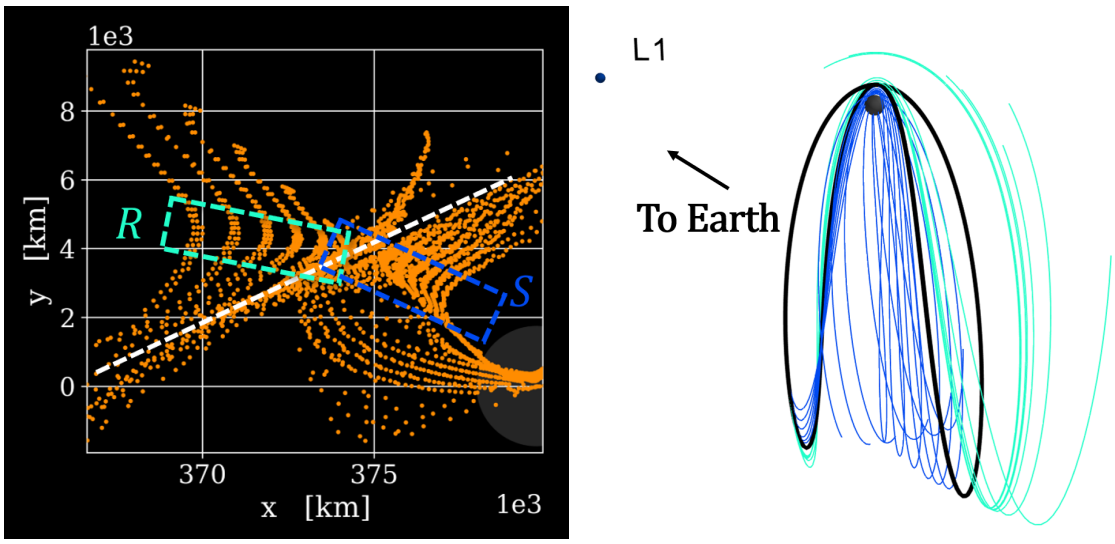

(a) Sepratrix geometry

(b) Arcs of sets C and D

Figure 4.11. Comparison of two types of structures from the Poincaré map in Figure 4.9. The colors of the dashed boxes in the left frame correspond to the colors of the orbits in the right frame. The reference butterfly is plotted in black.

orbit, and recall the subspaces defined by the eigenvalues and eigenvectors of the monodromy matrix in Section 4.1:

- The stable subspace, E^S, with dimension n_S,
- The stable subspace, E^U, with dimension n_U,
- The center subspace, E^C, with dimension n_C.

The subspaces are invariant; any solution initially defined entirely within the subspace remains in the subspace indefinitely when propagated under the linear system of equations. The points that lie within the stable subspace exhibit exponential decay; those in the unstable subspace reflect exponential growth; and those in the center subspace neither expand nor contract. Each type of subspace has an associated type of manifold. The local stable manifold is the set of all points in the vicinity of $\vec{x}^*$ such that flow initiated at these points asymptotically approaches $\vec{x}^*$ as $t \to +\infty$. Similarly,

the unstable manifold is the set of points in the vicinity of $\vec{x}^*$ that asymptotically approach $\vec{x}^*$ as $t \to -\infty$. The center manifold is then defined as the set of points in the vicinity of $\vec{x}^*$ that neither approach nor depart as $t \to \pm\infty$. Any of these manifolds may possess oscillatory modes in addition to their stable, unstable, or center modes. Such modes are associated with complex eigenvalues. A graphical representation of unstable and complex center manifolds are illustrated in Figure 4.12. The local

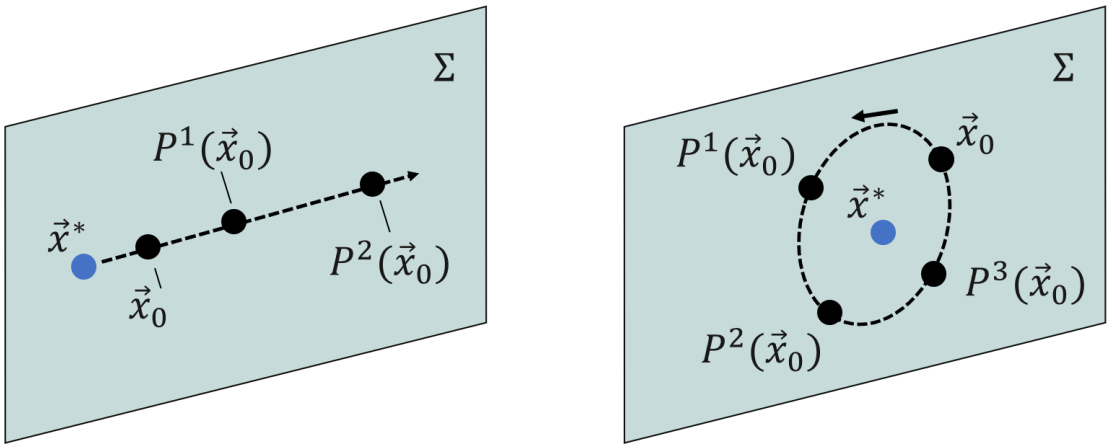

(a) Unstable manifold

(b) Complex center manifold

Figure 4.12. Representation of manifold crossings on a Poincaré map of an arbitrary hyperplane. The blue dot, x^*, represents a fixed point (periodic orbit). The black dots represent subsequent crossings on the map, with x_0 denoting an initial state on the manifold and $P^i(x_0)$ indicating the i-th crossing.

manifolds possess global analogs, generated by propagating points originating on the manifolds forwards and backwards in time using the complete nonlinear differential equations of motion. The global manifolds are tangent to their linear approximations at the fixed point [45]. While, for every fixed point along an orbit, the eigenvalues are identical, the orientation of the eigenvectors is not the same. In other words, the rate of expansion or contraction is the same at every point along the orbit, but the corresponding directions are unique for each fixed point. The tangency condition holds true for *all* fixed points.

4.3.1 Computation of Periodic Orbit Invariant Manifolds

The manifolds associated with periodic orbits are surfaces in the six-dimensional phase space comprised of an infinite set of trajectories. Thus, manifolds are typically represented graphically in terms of a finite set of trajectories sufficiently large enough in number to accurately represent the evolution of the manifold surface. The process of computing a trajectory along a manifold is initiated with a small perturbation relative to a fixed point and in the direction of the local eigenvector corresponding to the mode of interest. Denote the unstable manifold associated with the fixed point as $W^U(\vec{x}^*)$. Near the fixed point, the initial state along the manifold is approximated (to first order) by a step off the fixed point in the direction of the eigenvector corresponding to the unstable linear subspace. Thus, a point that is approximately on the unstable manifold is delivered by the relationship

$$\vec{x}_{U+} = \vec{x}^* + d\vec{\nu}_U, \tag{4.11}$$

where $\vec{x}^*$ is the 6-D fixed point, $\vec{\nu}_U$ is the 6-D eigenvector corresponding to the unstable subspace, and d is a constant to appropriately scale the vector. Note that the "+" in Equation (4.11) denotes the "right-half" vs the "left-half" manifold, i.e., simply the half-manifolds in the positive direction of the eigenvector and the negative direction of the same eigenvector, respectively. Choosing a value of d requires careful consideration. If the perturbation is too large, $\vec{x}_{U+}$ might not be close enough to an actual state on the manifold $W^U(\vec{X}^*)$. If the perturbation is too small, the resulting trajectory may spend too much time in its original vicinity before departing, resulting in a buildup of numerical error so that the path no longer lies on the manifold. Further, because the perturbation occurs in all six dimensions of the state vector, the process is somewhat unintuitive. A way to add clarity to the procedure is to normalize the eigenvectors with respect to, say, position. Define the components of the unstable eigenvector like so:

$$\vec{\nu}_U = \begin{bmatrix} x_U & y_U & z_U & \dot{x}_U & \dot{y}_U & \dot{z}_U \end{bmatrix}^T.$$

Then the position-normalized eigenvector is defined

$$\vec{\nu}_U = \frac{\vec{\nu}_U}{(x_U^2 + y_U^2 + z_U^2)^{1/2}}.$$

This allows the step size, d, to be interpreted as a physical distance. There is no value of d that is applicable for all scenarios, but a common starting point in the Earth-Moon is $d = 50$ km, or $d \approx 0.00013$ in nondimensional units. Propagating the point $\vec{x}_{U+}$ forward in time delivers an unstable half-manifold for the periodic orbit and associated with the fixed point $\vec{x}^*$. The other unstable half-manifold is delivered by repeating the procedure for $\vec{x}_{U-}$. In contrast, the stable manifolds are delivered by propagating the initial points in *negative* time. Recall that, since the eigenvalues are reciprocals, a stable manifold is always correlated with an unstable manifold. Plotting the global manifolds for the periodic orbit is typically constructed by leveraging a set of fixed point along an orbit. Collecting the trajectories for a discrete set of fixed points results in a set of "tubes" emanating from and approaching the orbit. The tubes are denoted such because of the their appearance when projected into configuration space. An example is plotted in Figure 4.13 for an arbitrary L_1 Lyapunov orbit in the Earth-Moon system. The zero-velocity curve associated with the orbit's Jacobi constant value is plotted as well. The eigenvectors for each point were normalized by position.

4.3.2 Invariant Manifolds Associated with Complex Eigenvalues

Invariant manifolds corresponding to complex eigenvalues are often associated with the center subspace. Such eigenvalues typically possess modulus one. Recall that any periodic orbit in the CRTBP will possesses two eigenvalues equal to unity—the trivial pair—indicating the periodicity of the trajectory and the existence of the trajectory within a family of solutions. Alternatively, complex eigenvalues on the unit circle indicate the existence of quasi-periodic motion in the vicinity of the fixed point. Interest in and analysis of such motion has expanded in recent years [46–53].

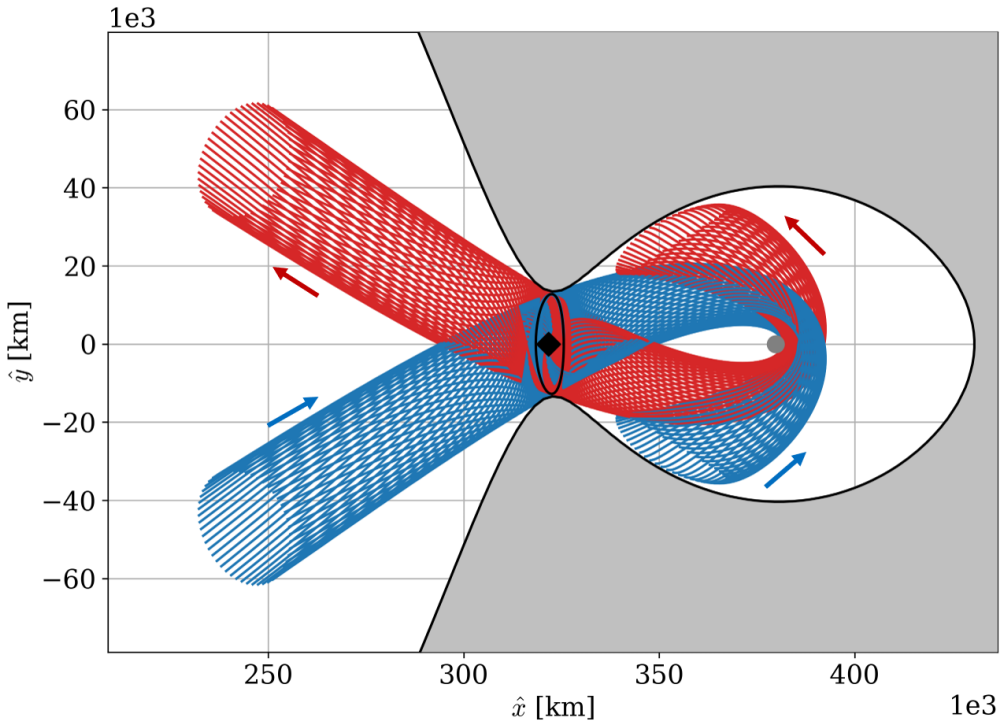

Figure 4.13. Global stable (blue) and unstable (red) manifold "tubes" associated with an L_1 Lyapunov orbit in the Earth-Moon system. The black diamond denotes L_1 and the gray area denotes the forbidden region.

There are examples of orbits in the CRTBP where the non-trivial eigenvalues of the monodromy matrix are complex and off the unit circle. These eigenvalues possess oscillatory modes coupled with stable/unstable modes. The associated motion is then a spiral sink or spiral source. One of the unique properties of these eigenvalues is that, if there is one pair of complex eigenvalues off the unit circle, the other non-trivial pair must also be off the unit circle; if $\lambda = a + jb$ is an eigenvalue, so is λ^{-1}, $\overline{\lambda}$, and $\overline{\lambda}^{-1}$, where the overbar represents the complex conjugate. This behavior is due the symmetric nature of the eigenstructure with respect to the unit circle and the real axis. The resulting subspaces are thus two-dimensional, $n_S = n_U = 2$. Relative to the periodic orbit, the two dimensions correspond to longitudinal motion along the manifold (motion approaching toward or departing from the obit) and rotational

motion (an apparent twisting or winding of the manifold "tube"). This behavior is illustrated in Figure 4.14. The frequency of rotation is indicated by the angle in the complex plane formed by the real and imaginary components associated with the eigenvalue.

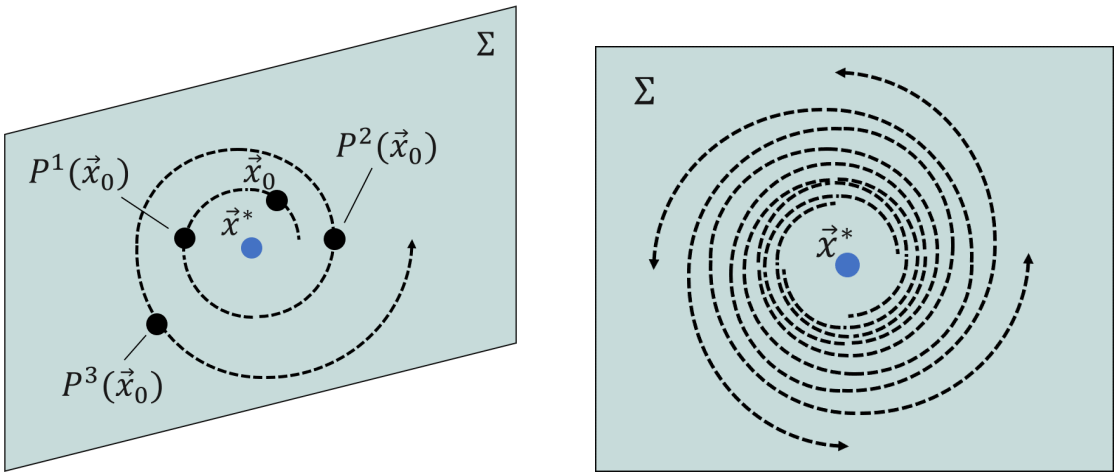

(a) Complex unstable manifold, single spiral

(b) Multiple sirals

Figure 4.14. Representation of spiral manifold crossings on a Poincaré map. The left frame represents a single trajectory on the manifold, while the right frame represents multiple trajectories.

Computation of these spiral manifolds combines the processes for computing (un)stable manifolds and center manifolds[2]. Consider an unstable spiral mode with the associated eigenvalue and eigenvector $\lambda_{\tilde{U}}$ and $\vec{\nu}_{\tilde{U}}$. The eigenvalue is complex with modulus > 1. The eigenvector is also complex. An initial state along the spiral manifold is delivered by perturbing the fixed point in the direction of the eigenvector $\vec{\nu}_{\tilde{U}}$. To capture the full dimensionality of the manifold (that is, to accomodate the rotational motion), apply the perturbation to a range of N equally-spaced angles

[2]Computation of center manifolds is covered in depth by Olikara nd McCarthy [47, 48].

$\{\theta_i \,|\, 0 \leq \theta_i < 2\pi\}$. The real-valued vectors approximating the states that lie along the spiral manifold are then delivered via the following relationship

$$\vec{x}_{i,\tilde{U}+} = \vec{x}^* + d\,(\mathrm{Re}[\vec{\nu}_{\tilde{U}}]\cos\theta_i - \mathrm{Im}[\vec{\nu}_{\tilde{U}}]\sin\theta_i), \tag{4.12}$$

where $\vec{x}^*$ is the fixed point, $\vec{x}_{i,\tilde{U}+}$ is the state on the manifold corresponding to the i-th angle θ_i, and d is a small scalar perturbation. Propagating the set of N points forward in time results in the right-half unstable manifold constructed at the specififed fixed point. Repeating the procedure for the left-half manifold, then repeating the procedure for every fixed point along the orbit, results in a three-dimensional unstable manifold corresponding to the periodic orbit.

4.4 Bifurcation Theory

Bifurcation theory is the study of changes in the qualitative behavior of a family of solutions to a system of differential equations. A change in the stability properties along a family indicates the presence of a bifurcation, and, potentially, the existence of a new family of solutions. Given a parameter curve defining a family (such as Figure 3.8), a point on the curve where a bifurcation occurs is denoted a *bifurcation point*, and the corresponding orbit in that family is denoted a *bifurcating orbit*. Bifurcation theory is fundamental to understanding the relationship between members of the halo family and the butterfly family of orbits, as well as their evolution.

Bifurcations in the CRTBP are identified by monitoring the eigenvalues of the monodromy matrix across the evolution of a family. A change in the eigenstructure, that is, a change in the number of real, complex, or unit-magnitude eigenvalues, signals a bifurcation. In this way, Broucke's stability diagram is an invaluable tool for analysis. Recall that each region of the diagram corresponds to a unique eigenstructure, and that the boundaries of each region were defined by critical values of the eigenvalues. Thus, when plotting members of a family on the diagram, if the curve crosses one of these boundaries, a bifurcation has occurred. The exact type of bifurcation can be identified by the boundary that was traversed.

4.4.1 Types of Bifurcations

There are 15 unique bifurcations present on the Broucke stability diagram as depicted in Figure 4.1, each classified by the number and location of the eigenvalues in the complex plane. Each of the 15 bifurcations exhibits one of the three following behaviors:

1. **Tangent Bifurcation.** A single pair of eigenvalues collides at $+1$: the eigenvalues move from the unit circle to the positive real axis, or from the positive real axis to the unit circle. An eigenvalue collides with its own reciprocal. This bifurcation corresponds to crossing the boundary $B = -2A - 2$ on the Broucke stability diagram.

2. **Period-Doubling Bifurcation.** A single pair of eigenvalues collides at -1: the eigenvalues move from the unit circle to the negative real axis, or from the negative real axis to the unit circle. An eigenvalue collides with its own reciprocal. This bifurcation corresponds to crossing the boundary $B = 2A - 2$ on the Broucke stability diagram.

3. **Secondary Hopf Bifurcation.** A pair of eigenvalues collides with another pair of eigenvalues on the unit circle (known as a Krein collision): two pairs of eigenvalues split from the unit circle into the complex plane, or two pairs of eigenvalues meet on the unit circle from the complex plane. The eigenvalue of one pair collides with the reciprocal eigenvalue of the conjugate pair. This bifurcations corresponds to crossing the boundary $B = A^2/4 + 2$ on the Broucke stability diagram.

All three bifurcation types occur in both the L_2 halo and the butterfly families. The butterfly family itself originates from a period-doubling bifurcation along the halo family. The three bifurcation types can be classified further.

Tangent Bifurcations

There are three types of tangent bifurcations:the cyclic-fold bifurcation, the pitchfork bifurcation, and the transcritical bifurcation. Of note for this investigation are the cyclic-fold and pitchfork bifurcations. Cyclic-folds indicate a change in the stability of the family, but a new family does *not* exist at this bifurcation. In general, at every local extremum of the Jacobi constant value, the order of instability can change. If the order changes, a cyclic-fold bifurcation occurs [39]. The pitchfork bifurcation indicates the presence of another family with different stability characteristics, without a change of stability in the original family.

Period-Doubling Bifurcations

At a period-doubling bifurcation, a new family of solutions exist with periods that are approximately twice that of the corresponding orbits in the original family. The original family undergoes a stability change, but the new family does not. Further, while the bifurcation occurs at -1 for the original family, the corresponding eigenvalues of the new family must collide at $+1$. This logic follows from an evaluation of the monodromy matrix for the minimal period family. From the properties of the STM and the monodromy matrix, the eigenvalues of the STM evaluated at m minimal periods are equal to the eigenvalues of the monodromy matrix raised to the m-th power. A bifurcation at $+1$ without a stability change corresponds to a pitchfork bifurcation. Thus, when a family of periodic orbits encounters a period-doubling bifurcation, the double-period family encounters a pitchfork bifurcation.

Secondary Hopf Bifurcation

This bifurcation is also denoted a "torus bifurcation." Because this investigation is focused only on the halo and butterfly families, the new families associated with secondary Hopf bifurcations are not currently relevant. However, it is still worthwhile

to track such bifurcations because they represent important stability changes. Subsets of the L_2 butterfly family in region **II** of the Broucke stability diagram possess spiral manifolds, which require extra steps when using the manifolds in transfer construction (as noted in Section 4.3.2).

5. THE HALO FAMILY AND EVOLUTION OF THE BUTTERFLY FAMILY

This chapter provides an overview of the halo family and a discussion of the evolution of the butterfly families. A subset of the halo family, the near rectilinear halo orbits, are identified by their stability characteristics. The evolution of the butterfly family is discussed in detail in terms of its geometry, stability, and Jacobi constant. The implications of the evolution on transfer design are also discussed.

5.1 The Halo Family

Halo orbits have been investigated and leveraged in space missions since the 1970s; halo orbits emanate from all three of the collinear libration points. Of note, a small subset of the family for each of the libration points exhibit nearly stable behavior, denoted Near Rectilinear Halo Orbits (NRHOs). Such an orbit in the L_2 southern halo family is the current baseline for NASA's planned lunar facility [3]. The L_2 halo family originates from a tangent bifurcation along the L_2 Lyapunov family. At the bifurcation point, both the Lyapunov orbit and the halo orbit are planar, but the halo family continues out of plane in both the $+z$ and $-z$ directions. The orbits that continue in the $+z$ direction are labelled the northern halos, while those that continue in the $-z$ direction are labelled the southern halos. The northern and southern halos are simply reflections of each other across the x-y plane; switching the z-position components of one family member results in a member of the opposite family. Like the Lyapunov family, the halo family possesses two perpendicular crossings of the x-z plane: one at perilune and one at apolune. The $\dot{x}$ and $\dot{z}$ velocity components are zero at these points. A portion of the L_2 Lyapunov and southern halo families appear in Figure 5.1. Members of the Lyapunov family are plotted in green, members of

the southern halo family plotted in blue, and the bifurcating orbit is highlighted in red. As the halo family approaches the Moon, the out-of-plane position components

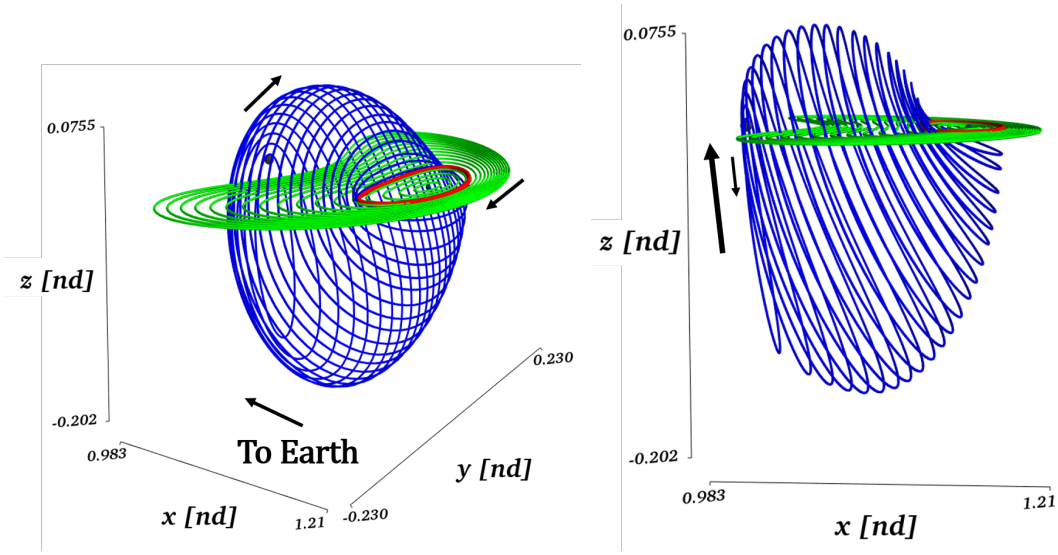

(a) (b) View along $+y$ axis.

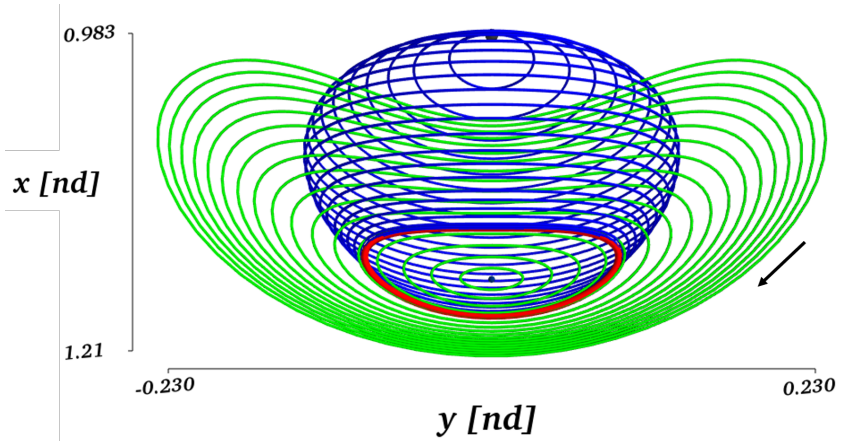

(c) View along $-z$ axis.

Figure 5.1. L_2 Lyapunov and southern halo families. The red orbit denotes the bifurcating orbit.

become more prominent. It is in this region that the NRHOs reside. The L_2 southern NRHOs possess close passages of the northern hemisphere of the Moon while spending most of their period below the Moon's southern hemisphere (i.e., in the $-z$ direction).

The inverse is true for the northern NRHOs. Near Rectilinear Halo Orbits may be precisely defined by their stability characteristics.

5.1.1 Near Rectilinear Halo Orbits

Near Rectilinear Halo Orbits are distinct from most other members of the halo family with respect to their stability and geometrical properties. They are characterized by their large out-of-plane components and nearly-stable behavior. Within the Earth-Moon L_1 and L_2 halo families, NRHOs exist as portions along each family near the Moon that possess stability indices within some small bound surrounding ± 1, with no stability index being significantly larger in magnitude than the other. For the Earth-Moon L_2 halo family in particular[1], this region is demarcated by the first and third stability change in the region of the family near the Moon. The first three stability changes, or bifurcations, are denoted by the red boxes in Figure 5.2. Notice that, after the third stability change, one of the stability indices grows significantly with respect to the other. The term "nearly stable" conveys the sensitivity of NRHOs to perturbations. Perturbations to orbits with large values of stability index grow more quickly than for orbits with smaller stability indices. This characteristic is one of the attractive qualities of NRHOs; the small magnitudes of stability index imply low station-keeping costs, which has been investigated by multiple authors [6, 21, 22]. Because the northern and southern families are simple reflections of each other across the x-y plane, they possess identical stability characteristics and the same definition holds.

Near Rectilinear Halo Orbits are dominated by their out-of-plane position components. Like many members of the halo family, NRHOs maintain line-of-sight to the Earth over the entire orbital period. However, NRHOs nearly perpendicular to the plane of the primaries. Their perilune radii are significantly smaller than their apolune radii, so they spend significantly more of their time near apolune. In the case

[1]The definition of the L_1 family is slightly different.

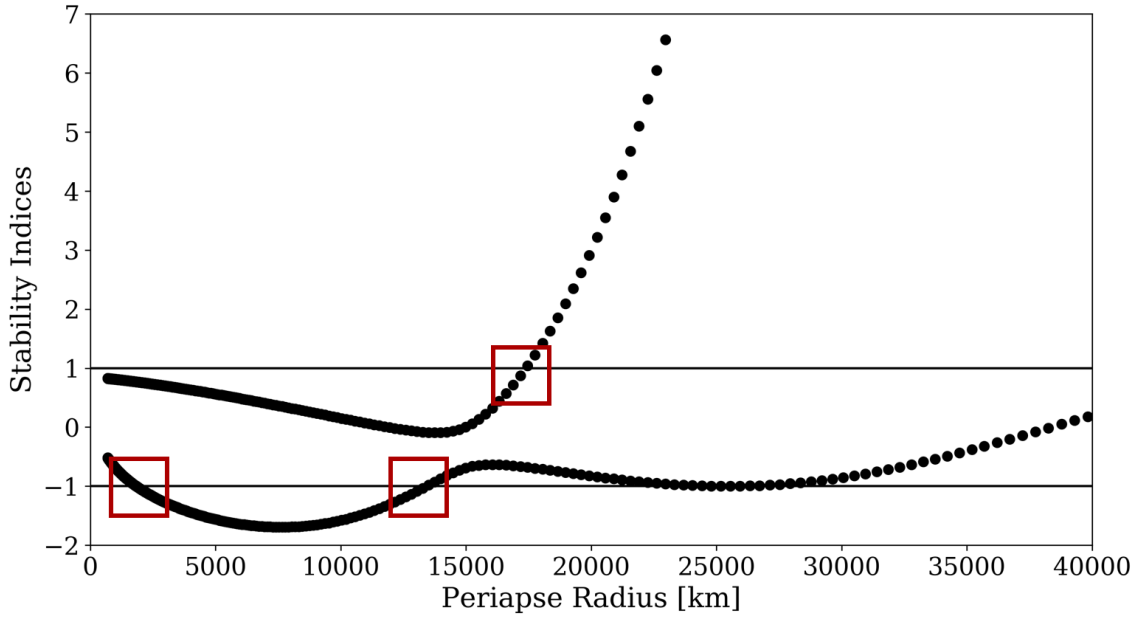

Figure 5.2. Stability indices of the L_2 southern halo family near the Moon. The changes in stability that define the NRHO subset are denoted by red boxes.

of the southern L_2 family, apolune is below the x-y plane, so spacecraft in these orbits maintain visibility of the southern hemisphere of the Moon for long time intervals. This type of coverage facilitates polar surface operations [31, 38]. The bifurcating orbits that define the range of NRHOs possess perilune radii of approximately 1,833 km and 17,400 km, with respective periods of approximately 6 days and 10 days. The corresponding apolune radii are approximately 67,500 km and 86,000 km. Thus, there is a wide range of a orbits within the NRHO subset that may be leveraged for cislunar missions. The halo family appears again in Figure 5.3. An NRHO possessing lunar synodic resonance is highlighted in purple, and the two orbits demarcating the subset of NRHOs are highlighted in red. All family members between these two orbits are members of the NRHO subset. Note that this figure does not plot any halo orbits with perilune radii smaller than that of the lower bound of the NRHO subset, but such members of the L_2 halo family do exist.

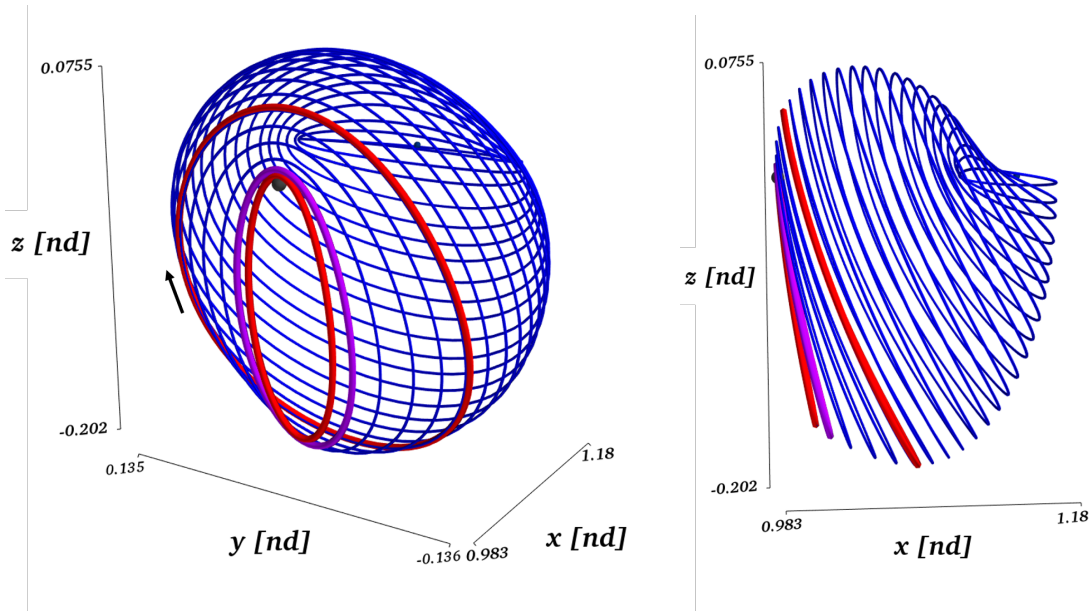

(a) (b) View along $+y$ axis.

Figure 5.3. L_2 southern halo orbits. The red orbits bound the subset or NRHOs and the purple obit denotes the 9:2 resonant NRHO.

In addition to their stability properties, one of the useful properties of some NRHOs is their ability to avoid eclipses. By leveraging a lunar synodic resonance, it is possible for spacecraft in NRHOs to avoid lunar and Earth eclipses for a significant duration of time [4, 19, 21, 23]. Spacecraft in orbits with a lunar synodic resonance complete an integer number of revolutions in their orbit during an integer number of synodic periods of the Moon in orbit about the Earth; a y:n resonance indicates that a spacecraft completes y orbits for every n revolutions of the Moon about the Earth. The sidereal period of the Moon, as opposed to its synodic period, is the time required for the Moon to complete one revolution of the Earth and return to its original position with respect to an inertially-fixed observer. Equivalently, the sidereal period is the time required for the Moon to return to its original position in the sky as seen by an observer fixed at the center of the Earth. The synodic period, then, is the time required for the Moon to return to its position in the sky relative to the Sun.

Equivalently, it is the the time between successive syzygy configurations of the Sun, the Earth, and the Moon. The sidereal period of the Moon is approximately 27.322 days, while the synodic period is approximately 29.5306 days. The current baseline for NASA's proposed ci slunar facility is a 9:2 synodic resonant NRHO [23][2]. Hence, the 9:2 NRHO is selected as the baseline for all NRHO-to-butterfly transfers in this investigation. The 9:2 resonant NRHO possesses a perilune radius of approximately 3,250 km, an apolune radius of approximately 71,200 km, and a period of approximately 6.56 days. The stability indices of this orbit are $\nu_{1,2} \approx -1.3235, 0.6828$. Thus, this NRHO demonstrates nearly stable behavior in addition to its beneficial eclipsing properties.

5.2 The Butterfly Family

The L_2 southern butterfly family originates from a period-doubling bifurcation along the L_2 southern halo orbit family. Like the halo family, the butterfly family possesses a mirror configuration across the x-y plane. This investigation focuses on transfers to the L_2 southern butterfly family. Initially, members of the butterfly family near the originating bifurcation orbit exist primarily in the vicinity of the Moon, but, as the family continues to grow, it begins to encompass a broader range across the Earth-Moon system. The bifurcating orbit in the halo family that generates the butterfly family is, in fact, the lower bound in the NRHO subset, that is, the halo orbit corresponding to the first stability change in Figure 5.2 with perilune radius equal to 1,833 km. The L_2 southern halos (blue), the bifurcating halo (red), and a small subset of the butterfly family (purple) appear in Figure 5.4.

The evolution of the butterfly family is complex geometrically *and* in terms of its period, energy, and stability properties. Consider first the stability evolution of the family (using the alternative definition of stability index introduced in Section 4.1.3). The alternative stability indices, ς_i, over a large portion of the family appear in Fig-

[2]For every 9 revolutions along the NRHO completed by a spacecraft, the Moon completes 2 synodic revolutions about the Earth.

ure 5.5[3]. Note that the final butterfly orbit plotted in Figure 5.4 possesses a period of approximately 19.6 days, so the range of orbits appearing in the stability index plot is much greater than the range of orbits shown in the halo-butterfly bifurcation visualization in Figure 5.4. This larger coverage of the butterfly family undergoes several

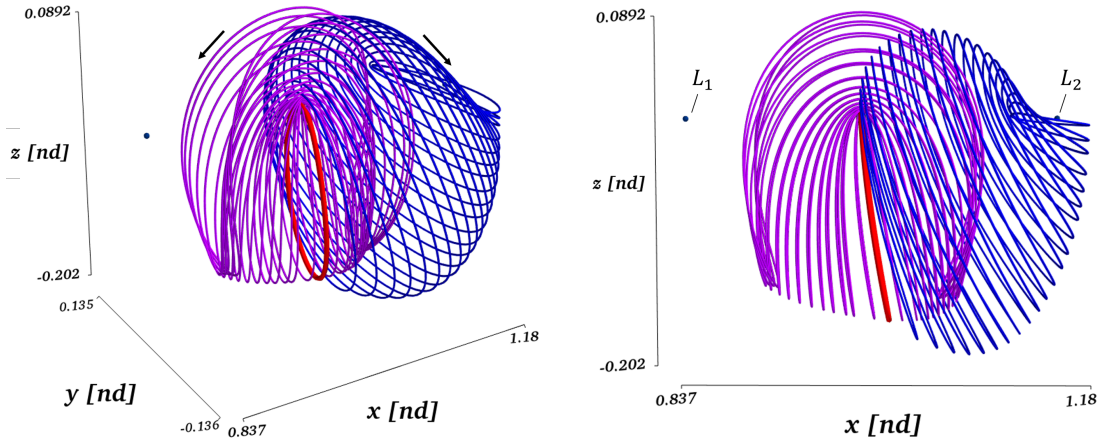

(a) (b) View along $+y$ axis.

Figure 5.4. L_2 southern halo and butterfly families. The red orbit denotes the bifurcating orbit.

stability changes throughout its evolution. The numbered boxes 2–5 in Figure 5.5, corresponding to the loops in the stability index curve, denote distinct eigenstructures. Boxes 1 and 6 represent particular orbits at which bifurcations occur. To aid in understanding the evolution of bifurcations across the family, the family is plotted on a Broucke stability diagram, as observed in Figure 5.6. The same numbered boxes from Figure 5.5 appear on the Broucke stability diagram. The originating member of the family exists on the line $-2A-2$, corresponding to a tangent bifurcation, and continues in the direction of the black arrow in Figure 5.6(a) into region **VI**. The family passes through region **III** briefly, then returns to region **VI** before passing into

[3]Stability indices for a family or obits are often plotted against orbit perilune, however, this portion of the butterfly family possesses multiple orbits with the same perilune radius. To avoid confusion, the stability index plot is presented with orbit period along the x axis in Figure 5.5.

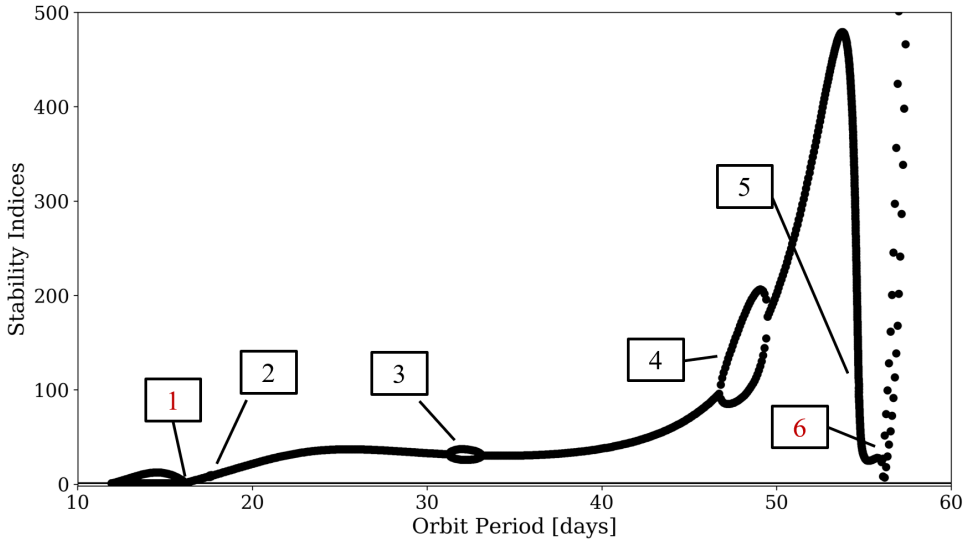

(a) Wide view

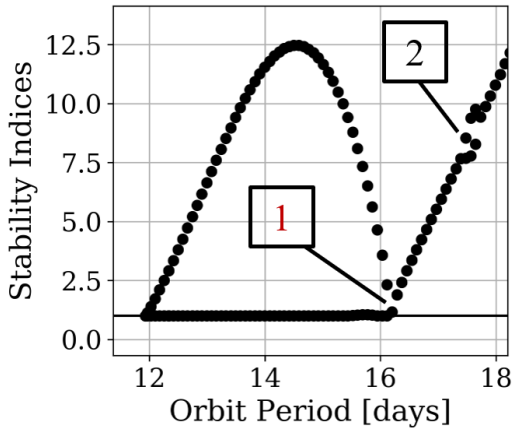

(b) View near bifurcation 1

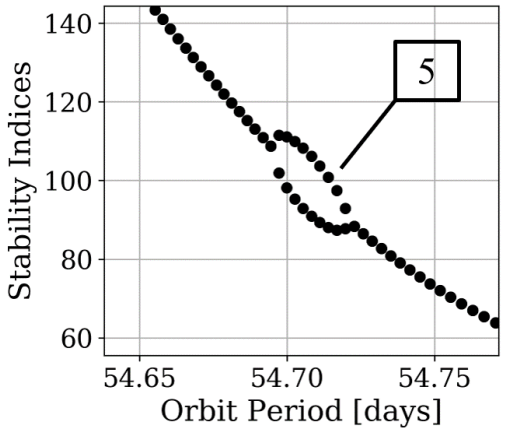

(c) View near bifurcation 1

Figure 5.5. Alternative stability indices for a portion of the L_2 southern butterfly family. Small subsets of the family with different stability properties are denoted by the numbered boxes.

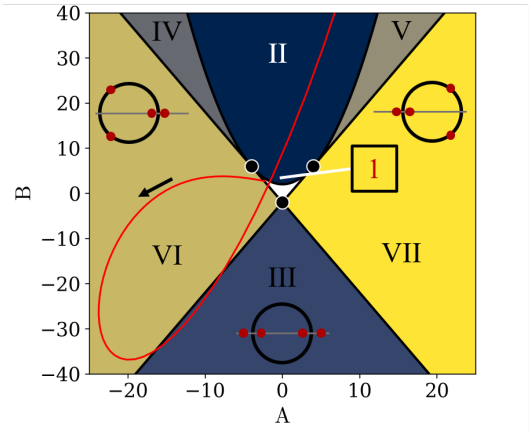

(a) View near bifurcation 1

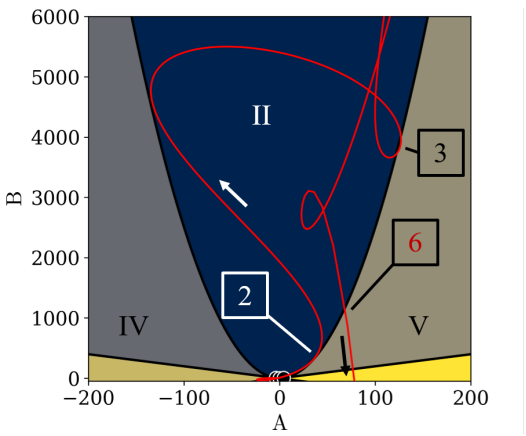

(b) View near subsets 2, 3, and bifurcation 6

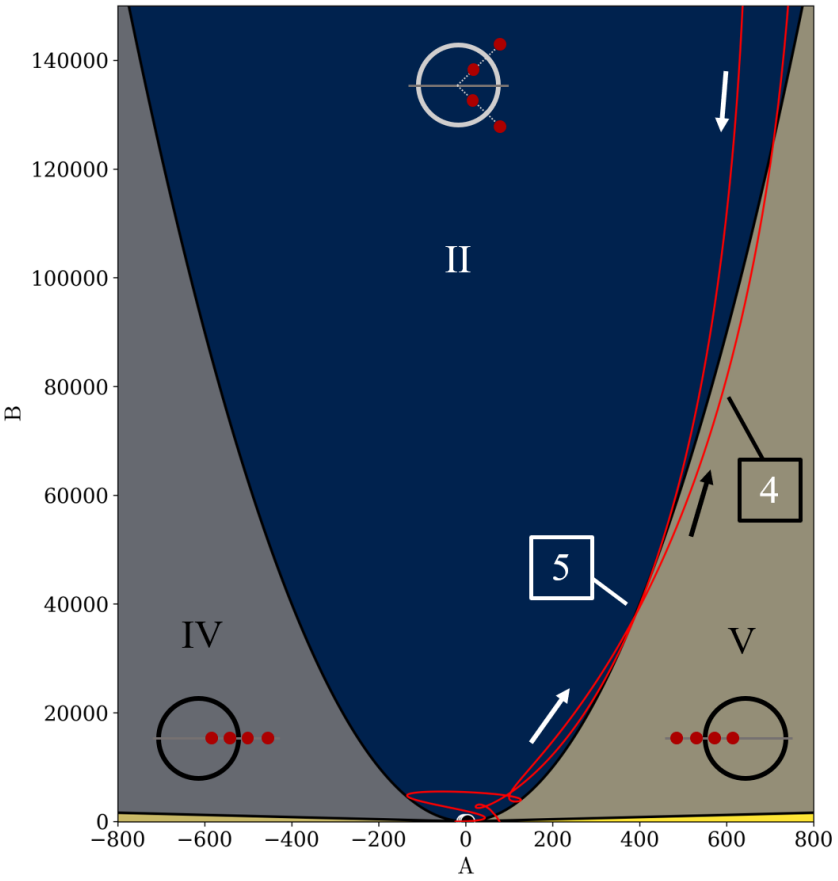

(c) View of subsets 4 and 5

Figure 5.6. L_2 southern halo and butterfly families. The red orbit denotes the bifurcating orbit.

region **I** and then, finally, region **II**. Recall that crossing any of the boundaries on the stability diagram corresponds to a particular bifurcation, and every region represents a unique eigenstructure. Thus, the L_2 butterfly family possesses three different eigenstructures before passing into region **II**; this passage into region **II** is denoted by box 1. Now, moving through region **II** on the Broucke stability diagram, the family crosses the $A^2/4 + 2$ boundary twice in quick succession. This small subset in region **V** is denoted by box 2 in Figure 5.6(b)[4]. The family continues through region **II**, following the white arrow in Figure 5.6(b), until again crossing the **II** $\Leftrightarrow$ **V** boundary twice in quick succession. This subset is denoted by box 3 in Figure 5.6(b). After continuing farther into region **II**, the family once again passes into region **V**. The family lingers in the area for a significant portion of its evolution, denoted by box 4, before reentering region **II** at the top-right corner of Figure 5.6(c). The family continues out of the frame and eventually returns along the downward-oriented white arrow in Figure 5.6(c). Once again, the family briefly passes into region **V** before returning to region **II** (subset 5). Continuing downward in the stability diagram, the family passes from region **II** to region **V**, denoted by box 6. The family then passes from region **V** to region **VII** (not labelled), and then continues into region **III** (not pictured). The eigenstructure of these butterfly orbits can influence mission design. It is evident that the range of the butterfly presented thus far possesses multiple eigenstructures and stability properties; the different eigenstructures can influence design by dictating the nature of the manifold structures that are available, which is particularly important if it is desired to leverage manifolds for a low-cost transfer. Preliminary design and analysis is more complex in region **II**, where the manifolds possess an extra dimension—and most of the L_2 butterfly family presented in this investigation exists in region **II**. Further, the magnitude of the stability indices is correlated to station-keeping and transfer costs; in general, a smaller stability index leads to lower station-keeping costs [38].

[4]The crossings are difficult to distinguish at the scale presented in the figure

The evolution of the Jacobi constant value, C, for the butterfly family is not as complex as its stability evolution. The Jacobi constant value evolution appears in Figure 5.7. The Jacobi constant value for the 9:2 NRHO is also presented in the figure. It is clear that this range of the butterfly family only possesses the same Jacobi constant value as the 9:2 NRHO at one particular point. Thus, there is only one candidate orbit in this range of the butterfly family that may offer a no-cost transfer. Considering the rest of the family, the change in C is relatively small for the first portion of the curve, before dropping at an orbit period corresponding to approximately 50 days. In general, the smaller the difference in Jacobi constant value between two orbits, the lower the transfer cost. Thus, butterfly orbits at this lower value of Jacobi constant (corresponding to a higher energy level) are relatively more expensive to transfer to.

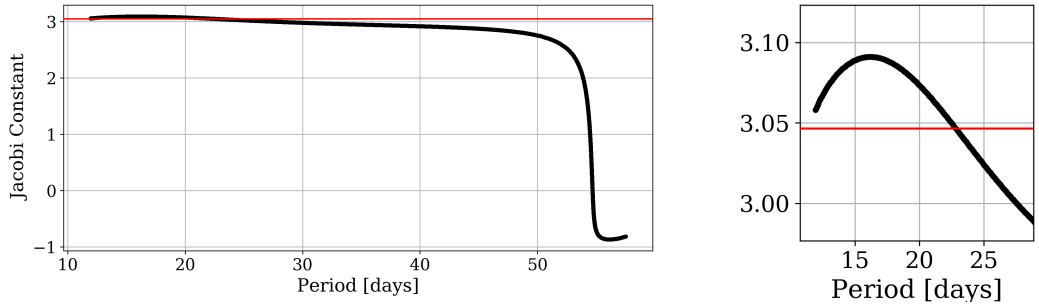

(a) Wide view

(b) Zoomed view

Figure 5.7. Period and Jacobi constant evolution for the L_2 southern butterfly family. The 9:2 NRHO Jacobi constant value is indicated by the red line.

The geometrical evolution for a large range of the butterfly family appears in the following figures. As the family expands, the behavior becomes more complex. Thus, each figure presents a portion of the family, starting with the originating orbit of the butterfly family and ending with one of the subsets denoted in Figure 5.5 (that is, every portion of the family begins with the same butterfly member—the originating orbit at the period-doubling bifurcation along the halos—and ends with a member

farther out in its evolution). The family does continue beyond that in the figures, however, the large periods and stability index magnitudes result in less practical orbits for mission design. The outer-most orbit shown in Figure 5.13 marks the end of the region of butterflies considered in this analysis. A notable feature of the family occurs at the orbit highlighted in blue in Figure 5.8, denoting a change in the geometrical structure of the lobes. The period of the highlighted orbit is approximately 14.75 days. Some of the orbits along the butterfly family possess two distinct lobes: one on the Earth-facing side of the Moon and one on the opposite side. The state vectors at the apex of each lobe are perpendicular crossings of the x-z plane; the y-position as well as the x and z components of velocity are zero. For every butterfly member existing before this orbit, the state vectors at the perpendicular crossing of each lobe possesses a y-velocity in the $-\hat{y}$-direction, which is in the same direction as the perpendicular crossing of the NRHO apolune state vector. At the blue-highlighted butterfly orbit, however, the y-velocity is zero, and, as the family continues to expand, the y-velocity grows in the $+\hat{y}$-direction. This is an important feature to note when designing families of transfers to this subset of the family.

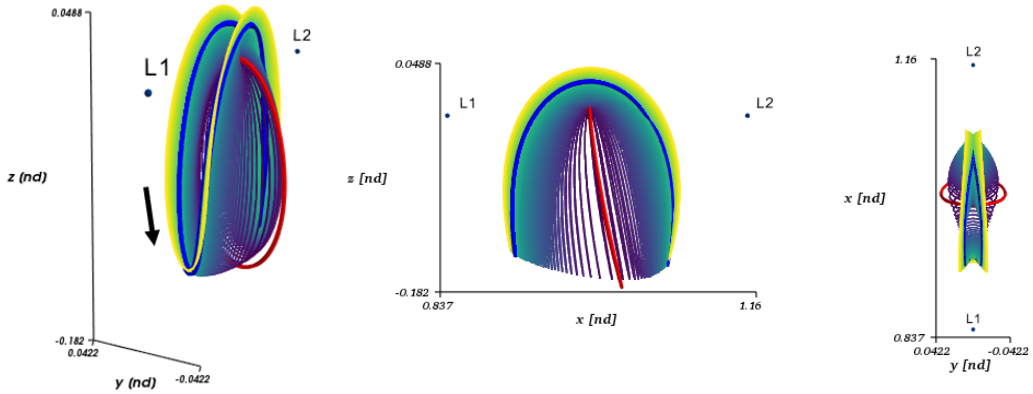

(a) (b) x-z plane (c) y-x plane

Figure 5.8. Members of the L_2 southern butterfly family up to and including bifurcation 1, denoted by box 1 in Figure 5.5 and Figure 5.6(a). The 9:2 NRHO is highlighted in red. The butterfly orbit corresponding to the perpendicular crossing reversal is colored in blue. Every other member of the family is denoted in a unique color, with the very first member of the family colored in purple.

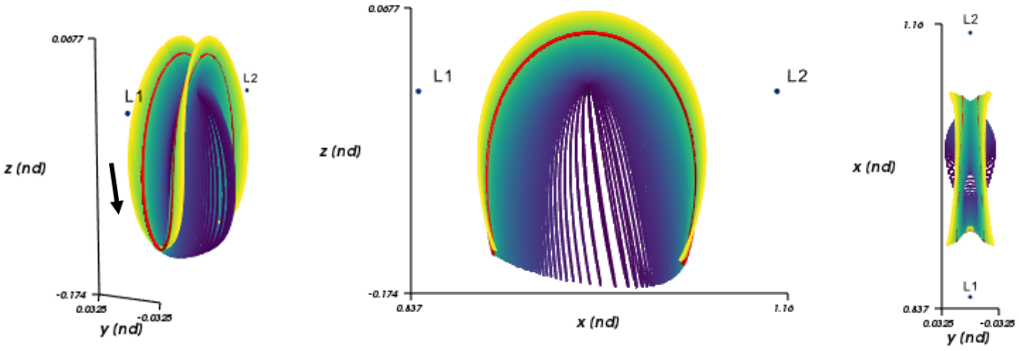

(a) (b) x-z plane (c) y-x plane

Figure 5.9. Members of the L_2 southern butterfly family up to and including the end of subset 2, denoted by box 2 in Figure 5.5 and Figure 5.6(b). The orbit at bifurcation 1 is highlighted in red.

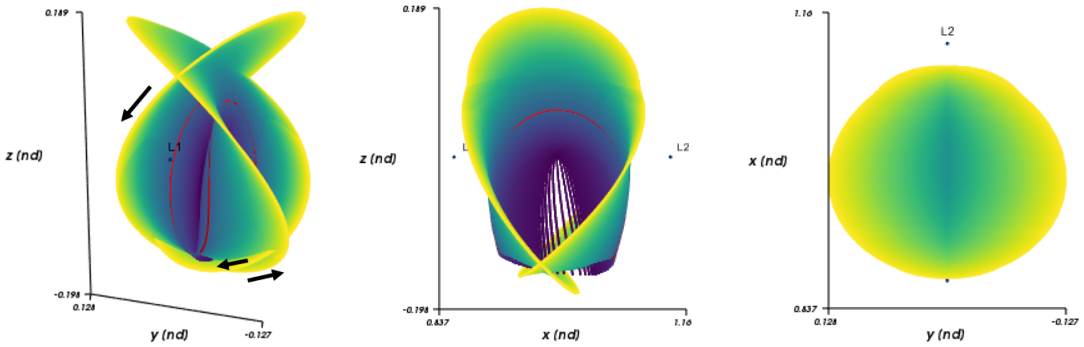

(a) (b) x-z plane (c) y-x plane

Figure 5.10. Members of the L_2 southern butterfly family up to and including the end of subset 3. The outermost orbit of subset 2 is highlighted in red.

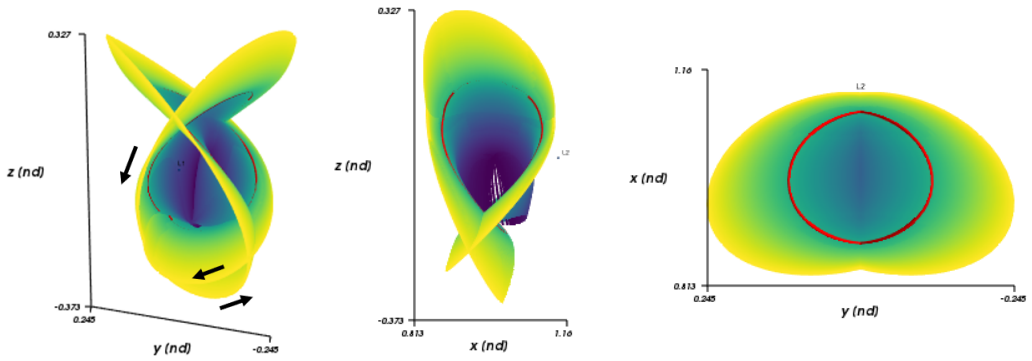

(a) (b) x-z plane (c) y-x plane

Figure 5.11. Members of the L_2 southern butterfly family up to and including the end of subset 4. The outermost orbit of subset 3 is highlighted in red.

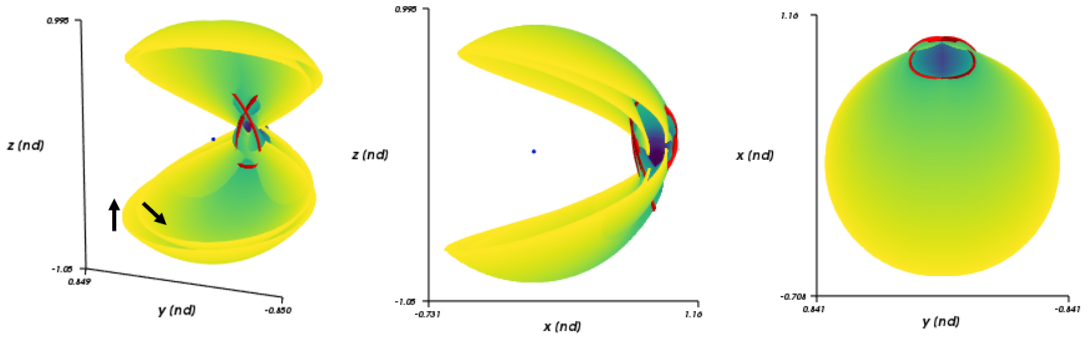

(a) (b) x-z plane (c) y-x plane

Figure 5.12. Members of the L_2 southern butterfly family up to and including the end of subset 5. The outermost orbit of subset 4 is highlighted in red. The small blue dot near the center of frame (b) represents the Earth.

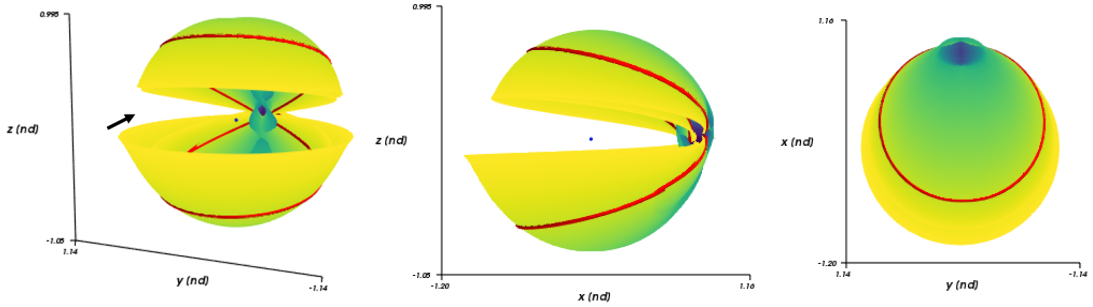

(a) (b) x-z plane (c) y-x plane

Figure 5.13. Members of the L_2 southern butterfly family up to and including bifurcation 6. The outermost orbit of subset 5 is highlighted in red. The small blue dot near the center of frame (b) represents the Earth.

6. TRANSFERS TO THE BUTTERFLY FAMILY

This chapter details the the methodology and results of designing transfers between the 9:2 resonant NRHO and members of the L_2 southern butterfly family. First, continuous families of solutions are found using two different design methodologies consisting of one-arc and two-arc transfers—denoted Type I and Type II, respectively. Some of these results are optimized to reduce total ΔV. The two-arc transfers benefit from applications of dynamical systems theory—in particular, Poincaré maps. Second, dynamical structures are leveraged to construct transfers to three different members of the butterfly family, denoted Type III transfers, each with unique stability characteristics. Each of the transfer methodologies presented in this section possess unique benefits. Finally, a small set of trajectories returning to the NRHO from members of the butterfly family is discussed.

6.1 Type I: One-Arc Transfers

It is possible to design transfers from the NRHO to members of the butterfly family utilizing a single transfer arc. Such designs are often the simplest solution and require lower times of flight, but may be more expensive in terms of propellant. These particular designs leverage the natural geometry of the NRHO and members of the butterfly family. As discussed in Section 5.2, the lobes of the butterfly family possess state vectors at perpendicular crossings of the x-z plane. The state vectors at perilune and apolune for the NRHO are also perpendicular crossings of the same plane. Because some members of the butterfly family possess lobes in the general vicinity of the NRHO's apolune state, and some of these lobes possess perpendicular crossings in the same direction as the NRHO's apolune state, transfers to such points along the butterfly orbits can leverage the natural flow of the system. However, the

evolution of the butterfly family is such that the same lobe does not represent the ideal target location across the entire family; at the beginning of the family, the apex of the lobe on the far side of the moon is in the vicinity of the NRHO apolune state. As the family continues to evolve, though, the velocity direction of the perpendicular crossing at the lobe reverses so that the velocity of the apex state is in the opposite direction as the NRHO apolune state. The butterfly orbit at which this switch occurs possesses a period of approximately 14.75 days. Conversely, as the butterfly family evolves, the apex of the lobe on the Earth-facing side of the Moon approaches the vicinity of the NRHO apolune state. The velocity direction of the perpendicular crossing at this lobe remains favorable for much of the family. Thus, a family of one-arc transfers is found for two subsets of the butterfly family where the geometry is favorable.

The design process for the Type I family of solutions is relatively simple. First, a feasible transfer solution is delivered from a targeting scheme. This targeting scheme delivers a maneuver at the perilune state of the NRHO and allows the transfer time to vary. The end state of the resulting arc is then constrained to be precisely at the apex of the lobe on the far side of the Moon of the target butterfly orbit. An example feasible solution to each of the butterfly regions discussed above is depicted in Figure 6.1. Once the feasible solution is converged, an optimizer can deliver a lower-cost transfer. The optimizer varies the departure location on the NRHO, the departure maneuver direction and magnitude, the transfer time, and the arrival location on the butterfly. The objective function to be minimized is the total transfer ΔV, that is, $\Delta V_{transfer} = \Delta V_{departure} + \Delta V_{arrival}$. A family of similar solutions can be delivered with a continuation scheme on subsequent members of the butterfly family by leveraging the optimized solution. The resulting transfer costs appear in Figure 6.2 for each of the butterfly geometries. Both figures present the results for the feasible solution and for the optimized solution. While it becomes more expensive after the geometry change, it is possible to construct one-arc transfers to a large portion of the butterfly family that are not prohibitively expensive. Recall that the perpendicular crossing

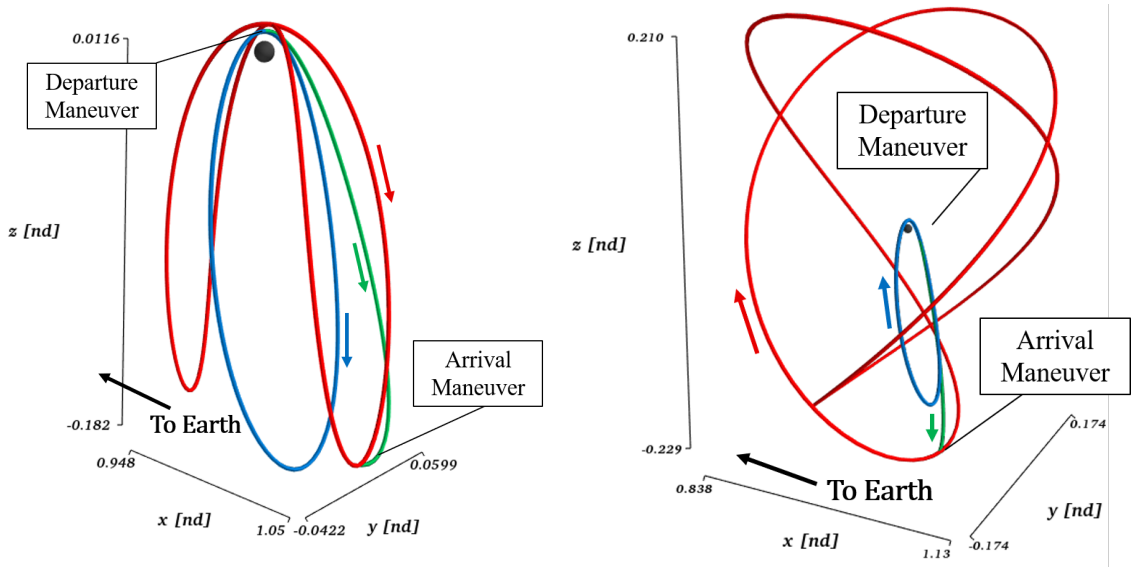

(a) Transfer to 1st perpendicular crossing (b) Transfer to 2nd perpendicular crossing

Figure 6.1. Examples of feasible Type I transfers (green) from the 9:2 NRHO (blue) to an arbitrary butterfly orbit (red). The left frame depicts a transfer to an early member of the butterfly family, before the perpendicular crossing at the lobe has switched direction. The right frame depicts a transfer to a butterfly after this switch has occurred; notice that the destination lobe has changed.

geometry change occurs along the butterfly family at an orbit period of approximately 14.75 days. Thus, a large portion of the transfers depicted in Figure 6.2(a) are subject to non-ideal geometries. The target butterfly orbits represented in Figure 6.2(b) possess a greater difference in Jacobi constant value from the NRHO than the butterflies in Figure 6.2(a), but the transfer costs are, in general, lower than those after a period of 14.75 days in Figure 6.2(a) . This lower cost is due to the more-favorable geometry, offsetting the greater difference in C. As the butterfly family continues to evolve, this type of transfer becomes less practical; the lobes of the family expand such that they are no longer in the vicinity of the NRHO apolune state.

Notice that few of the transfer costs in Figure 6.2 possess magnitudes near that of the theoretical minimum. This discrepancy is due to the formulation of the theo-

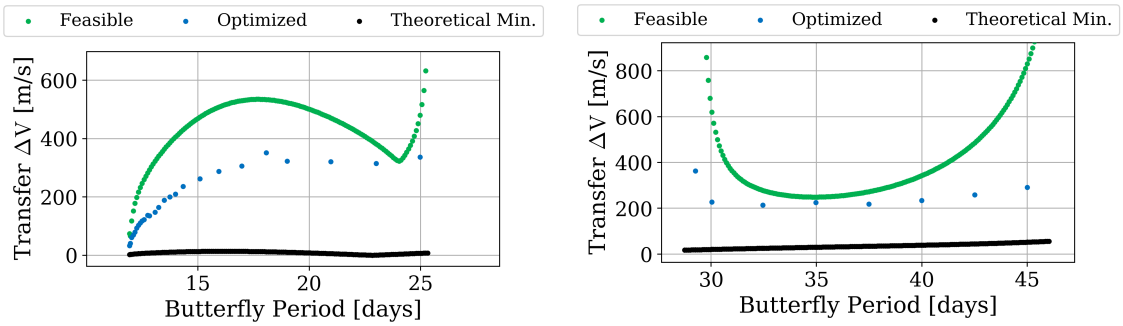

(a) Transfer to 1st perpendicular crossing

(b) Transfer to 2nd perpendicular crossing

Figure 6.2. Maneuver costs for one-arc transfers to each of the butterfly geometries. The feasible solution is colored in green, the optimized solution in blue, and the theoretical minimum in black.

retical minimum in Equation (2.41). This formulation leverages the maximum value of pseudo-potential from either of the orbits. Then, it is assumed that some arc, possessing the same Jacobi constant value as the orbit with the maximum pseudo-potential and possessing a position state with the same value of pseudo-potential as the maximum value, intersects the other orbit at a point where the velocity vectors are parallel. None of the transfer geometries corresponding to the results in Figure 6.2 meet such requirements. Thus, it is possible to design lower-cost transfers than those presented using the Type I approach, but such a process would be different than what is used in this investigation.

6.2 Type II: Two-Arc Transfers

The Type II transfer design utilizes two transfer arcs to join the 9:2 NRHO with members of the butterfly family. The first arc, denoted the departure arc, is initiated with a maneuver along the NRHO, departing its vicinity. A maneuver at the end of the departure arc puts the spacecraft onto a second arc, denoted the arrival arc. The arrival arc approaches the butterfly orbit, and ends with a third maneuver to

place the spacecraft onto the butterfly orbit. To deliver an initial guess for each arc, a range of maneuvers is applied at multiple points along both orbits. Such maneuvers range from 10 m/s to 60 m/s, applied in both the velocity and anti-velocity directions. The post-maneuver states are then propagated—with the resulting arcs from the butterfly orbit propagated in negative time—and their crossings are plotted on a Poincaré map, appearing in Figure 6.3. The glyphs in Figure 6.3(b) represent the extra dimensions of each crossing. The first vector, whose base point is the map crossing itself, represents the z and $\dot{z}$ position and velocity components by its abscissa and ordinate, respectively[1]. The abscissa and ordinate of the second vector, whose base point is the end point of the previous vector, represents $\dot{x}$ and $\dot{y}$, respectively. Glyphs with similar directions and magnitudes, whose base points are near each other in x and y position, indicate the potential existence of a low-cost transfer. Such candidates are indicated by the black boxes in Figure 6.3. Thus, one arc is selected from each of the boxes in Figure 6.3(b) to construct an initial guess. The initial guesses appear in Figure 6.4. To eliminate the position continuity between the end points of the two transfer arcs, a multiple shooter is leveraged. The shooting scheme allows the velocities to vary at the departure and arrival points of each arc while enforcing position continuity at the point where the two transfer arcs meet. The velocity discontinuity between the end points is treated as another maneuver. With a converged feasible solution, an optimizer further reduces the total ΔV, that is, $\Delta V_{total} = \Delta V_{departure} + \Delta V_{midcourse} + \Delta V_{arrival}$. Similar to the formulation of the Type I transfers, the optimizer varies the velocity directions and magnitudes of all three maneuvers, the time of flight along each maneuver, the departure location along the NRHO, and the target arrival location along the butterfly. The optimized transfer arcs are then used as the starting point in a continuation process to generate a family of similar transfers to other members of the butterfly family. This set of solutions investigates the same range of butterfly orbits that appears in Figure 6.2(a). The results of the continuation process appear in Figure 6.5. The optimized values

[1]The z position component is redundant, as the Poincaré map in this figure fixes the value of z

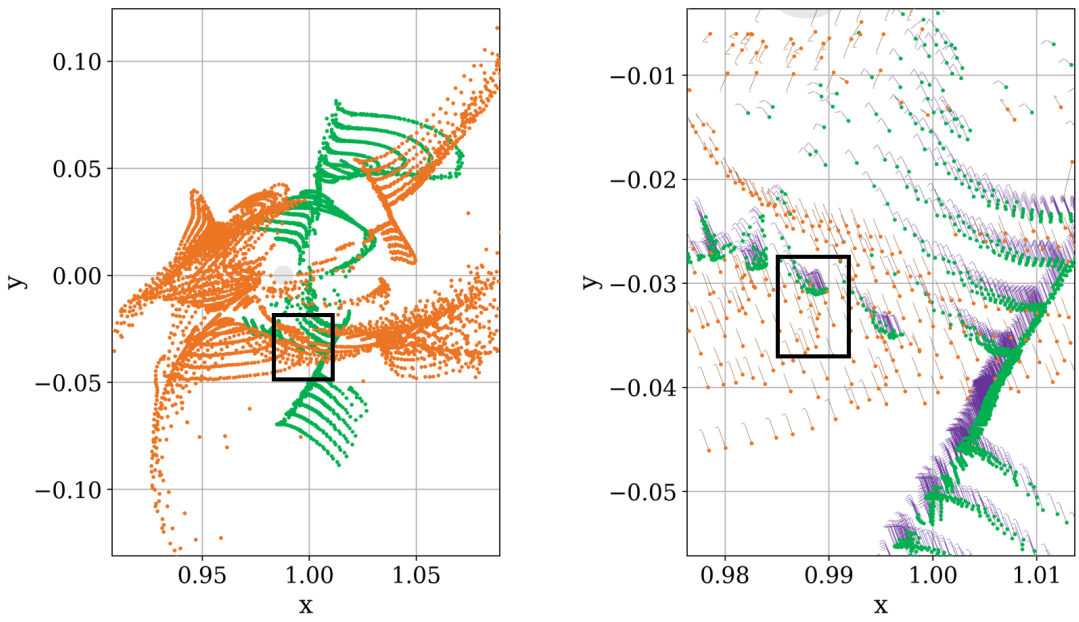

(a) (b) Zoomed near region of interest

Figure 6.3. Double-sided Poincaré map at $z = -0.11$ non-dimensional units for transfer arcs from the 9:2 NRHO (green points) to an arbitrary butterfly (orange points).

presented in this figure are commensurate with the corresponding values found by Davis et al. [21]. Similar to the Type I transfers, the optimization process yields lower-cost solutions, delivering significantly smaller transfer costs to some regions of the family. After the perpendicular crossing change, at about 14.75 days, the benefits of optimization again diminish. This behavior is expected, as the geometry leveraged for these transfers is not favorable for the entire range of the family. As for the Type I transfers, a similar design strategy, reapplied after the geometry change, would likely produce lower-cost results.

A comparison of the Type I and Type II transfer costs appears in Figure 6.6. Recall the butterfly orbit with period 14.75 days, where the direction of the perpendicular crossing becomes unfavorable. Before this change, the two-arc transfer

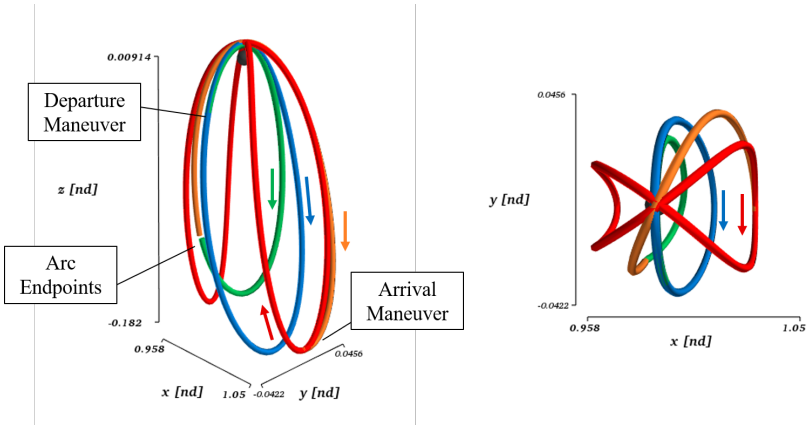

(a) (b) View along $-z$ axis

Figure 6.4. Initial guess for transfer from 9:2 NRHO (blue) to butterfly orbit (red). The arc departing the NRHO is depicted in green, and the arc approaching the butterfly is depicted in orange. The position discontinuity where the two transfer arcs is eliminated by differential corrections.

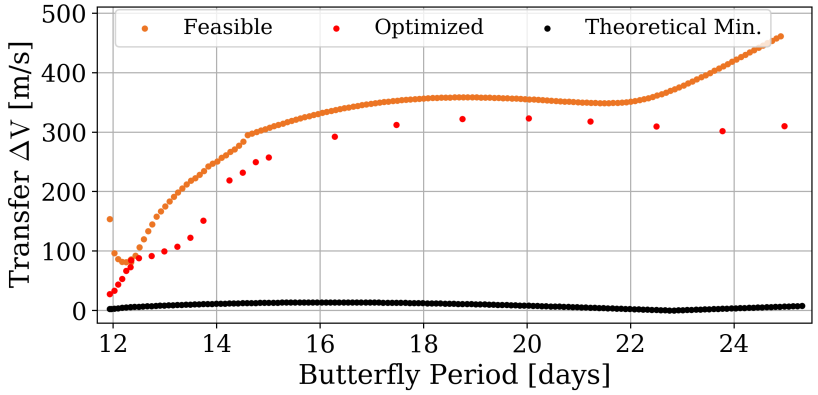

Figure 6.5. Maneuver costs for two-arc transfers. The feasible solution is colored in orange, the optimized solution in red, and the theoretical minimum in black.

costs are lower than the corresponding one-arc transfers. After this change, though, the benefits of the two-arc transfer over the one-arc transfer disappear; both transfer methodologies produce very similar results. For butterfly orbits with favorable geometry, it is clear that the two-arc transfer can deliver large fuel savings over the

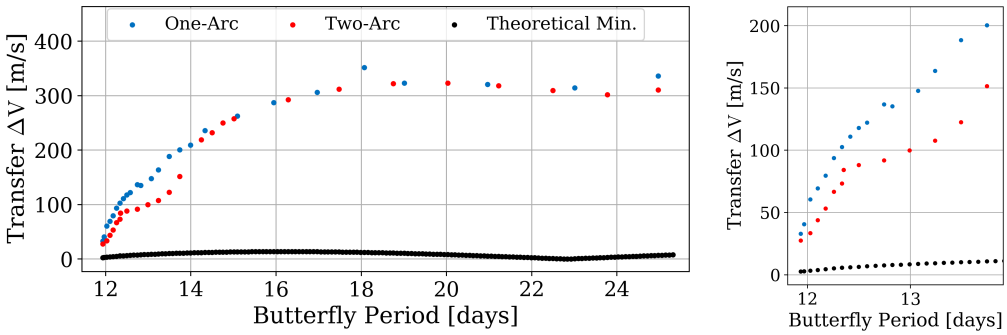

(a) (b) Favorable region

Figure 6.6. Comparison of optimized maneuver costs for one-arc transfers (blue) and two-arc transfers (red). The theoretical minimum appears again in black. Frame (b) zooms into the region of the butterfly family with favorable geometry.

one-arc transfer. Different design methodologies can deliver lower-cost maneuvers to the butterfly family, especially to regions of the family existing with orbit periods greater than 14.75 days.

6.3 Type III: Transfers Leveraging Stable Manifolds

The design process for Type III solutions leverages dynamical structures to produce low-cost transfers to members of the butterfly family. Members of the family are chosen by their stability characteristics such that they possess stable and unstable manifolds. The overarching design strategy is similar to the two-arc case. A range of maneuvers is applied along the NRHO and the resulting arcs are propagated forwards in time. However, instead of imparting a range of maneuvers along the butterfly orbit, the unstable manifold of the butterfly is leveraged for an initial guess. The stable manifold of the butterfly orbit is thus propagated backwards in time. Crossings from the NRHO departure arcs and the butterfly manifolds are recorded on a Poincaré map and a suitable initial guess if determined by searching for points on the map with commensurate position and velocity components. The initial guess is then con-

verged in a differential corrections process. The range of maneuvers applied to the NRHO depends on the theoretical minimum ΔV between the NRHO and the target butterfly; the minimum value of the range of maneuvers should be about as large as the theoretical minimum.

To illustrate the manifold-based design process, a candidate butterfly is chosen from region **II** of the Broucke stability diagram, as orbits in this region possess stable and unstable spiral manifolds. The candidate butterfly obit corresponds a perilune radius and period of approximately 43,000 km and 23 days. The 9:2 NRHO and the butterfly candidate appear in Figure 6.7. A potentially low-cost initial guess for the

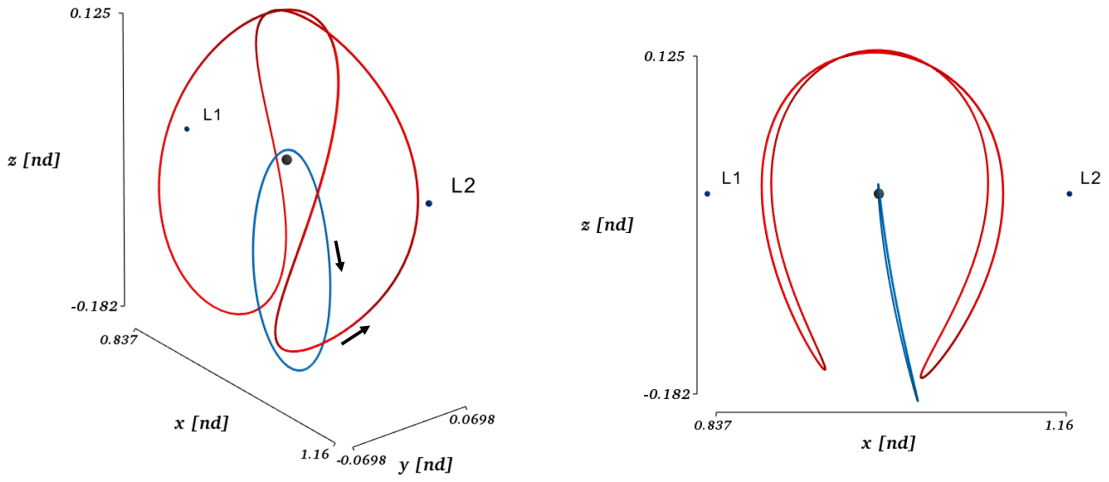

(a) (b) View along $+y$ axis

Figure 6.7. Butterfly orbit (red) and 9:2 NRHO (blue).

transfer exists where the departure arcs of the NRHO intersect the stable manifold of the butterfly orbit with similar velocity components. Such an intersection is found by recording the crossings of the NRHO departure arcs and the butterfly manifold on a Poincaré map, appearing in Figure 6.8. Using the initial guess highlighted in Figure 6.8(b), the two arcs are converged with a multiple shooter in the same

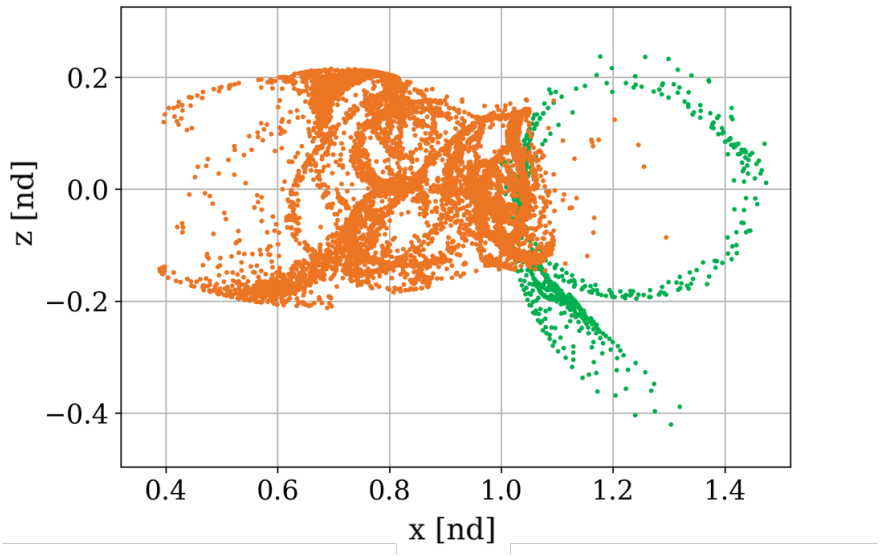

(a) Zoomed-out view

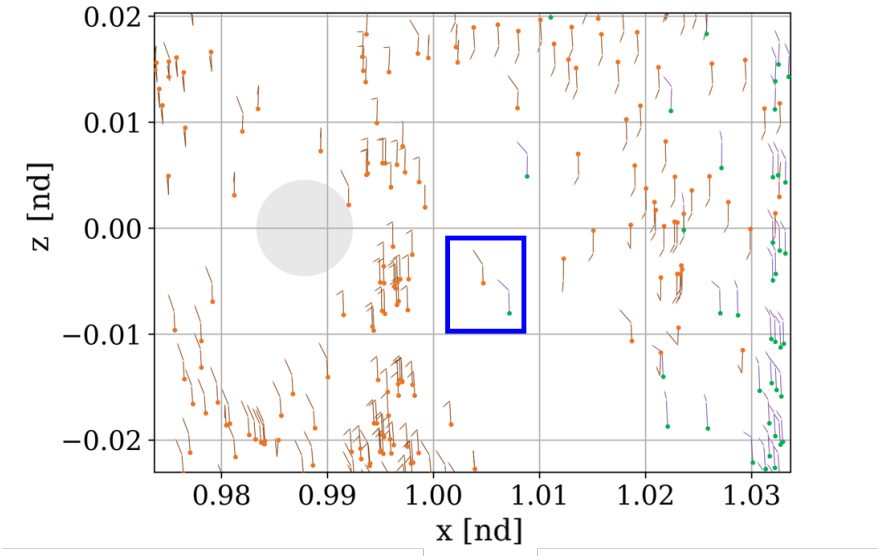

(b) Zoomed-in view with glyphs indicating extra dimensions

Figure 6.8. Poincaré map at $y = -0.10$ non-dimensional units for departures from 9:2 NRHO and a butterfly orbit possessing a spiral manifold. The piercings from the butterfly orbit's stable manifold are colored in orange, while the piercings from the NRHO departure arcs are colored in green. The Moon appears to scale as the light gray circle. The points used for the initial guess are highlighted by the blue box in frame (b).

fashion as the two-arc transfers. The targeter enforces position continuity between the endpoint of the NRHO departure arc and the entrance onto the butterfly manifold, allowing for a maneuver at this location. The departure maneuver magnitude and direction, arrival maneuver magnitude and direction, and times of flight along each arc are allowed to vary as well. The targeter delivers a feasible transfer with a total $\Delta V$from all three maneuvers equal to $\Delta V_{total} = 116.73$ m/s. The time of flight totals to 73.89 days, split between 18.23 days on the NRHO departure arc and 55.66 days on the butterfly manifold. The transfer is depicted in Figure 6.9. Notice that the arrival arc appears to asymptotically approach the butterfly orbit for a significant duration of its time of flight. This reflects the asymptotic nature of the stable manifold.

The manifold-based design process is repeated for transfers to multiple members of the butterfly family possessing stable manifolds. One candidate butterfly orbit is chosen from subset 4, denoted by box 4 in Figure 5.5 and Figure 5.6. Orbits in this subset possess eigenvalues that are all real; the resulting stable and unstable manifolds exhibit saddle behavior instead of spiral behavior. A third candidate butterfly orbit is chosen from the apex of the stability index plot in Figure 5.5, that is, the butterfly orbit with the largest stability index magnitudes between boxes 4 and 6 in Figure 5.5 and a period of approximately 53.76 days. The design process to each of these candidate butterfly orbits is the same; the transfer times and costs are summarized in Table 6.1, compared to the corresponding Type I and Type II transfers to the same butterfly orbits. The transfers produced by this methodology are significantly lower in terms of fuel than the Type I and Type II transfers detailed in the previous section. The lower ΔV transfer costs, though, require grater times of flight. Such a trade-off may not be feasible for a crewed mission, where time of flight considerations are more critical, but robotic missions with less stringent restrictions on transfer time could greatly benefit from the reduced transfer cost. These manifold-based transfers could be further improved by optimization.

Table 6.1. Comparison of Type I, Type II, and Type III transfer results. The Type III transfers represent only the feasible solution, while the results for the Type I and Type II transfers are the optimized solutions.

			Butterfly Period [days]		
			23.84	**47.48**	**53.76**
Transfer Type	**Type I**	Maneuver Cost [m/s]	314.39	336.35	2,236.65
		Time of Flight [days]	2.59	6.87	15.38
	Type II	Maneuver Cost [m/s]	301.64	-	-
		Time of Flight [days]	4.63	-	-
	Type III	Maneuver Cost [m/s]	116.73	265.37	541.48
		Time of Flight [days]	72.89	93.39	71.71

6.4 Return Transfers

While most of the designs in this investigation depart the NRHO and arrive at a butterfly orbit, the inverse is also a possible mission scenario. Thus, a family of solutions is delivered that departs from members of the butterfly family and arrives at the 9:2 NRHO. The design strategy for these orbits reflects that of the Type II transfer in reverse: a range of maneuvers is applied to both the NRHO and the butterfly orbit, and the resulting arcs are propagated. The butterfly departure arcs are propagated in forward time, while the NRHO arrival arcs are propagated in reverse time. A Poincaré map is leveraged to determine a potentially low-cost initial guess. The initial guess is converged with a differential corrections process, then optimized using the same approach as the Type II transfers. An example transfer is depicted in Figure 6.11. The optimized results, presented in Figure 6.10, exhibit similar behavior to the Type II NRHO-to-butterfly transfers in the same range of butterfly orbits. Thus, it is likely that these results could be further improved by leveraging Type III manifold-based design strategies.

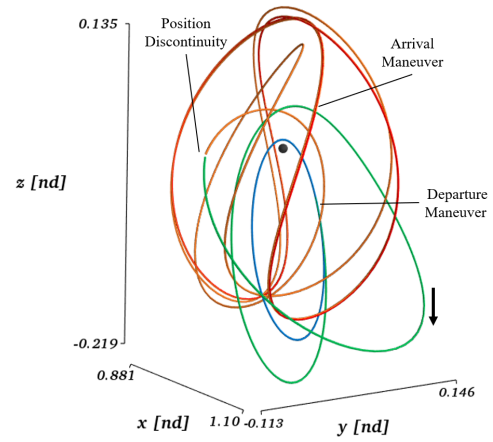

(a) Initial guess arcs

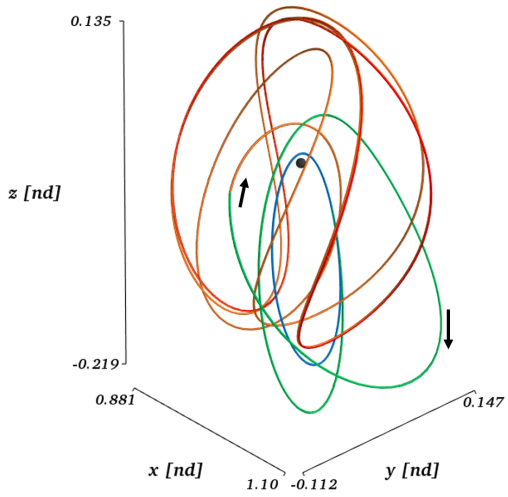

(b) Converged arcs

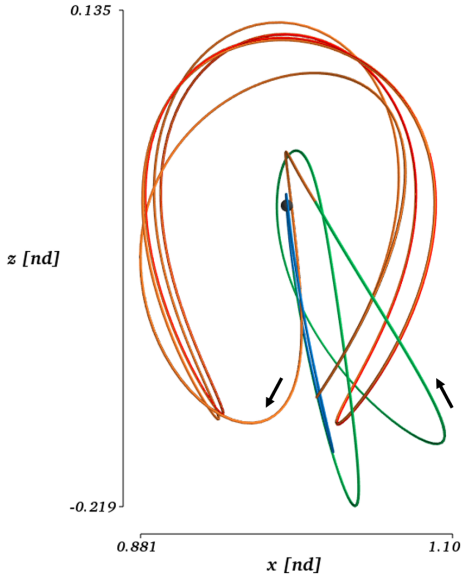

(c) Converged arcs, view along $+y$ axis

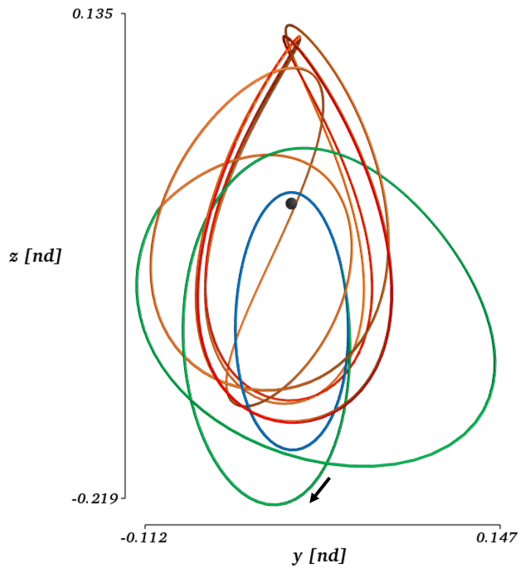

(d) Converged arcs, view along $-x$ axis

Figure 6.9. Initial guess arcs and converged arcs for a transfer from the 9:2 NRHO to the butterfly orbit. The NRHO appears in blue, the NRHO departure arc in green, the butterfly arrival arc in orange, and the butterfly orbit in red.

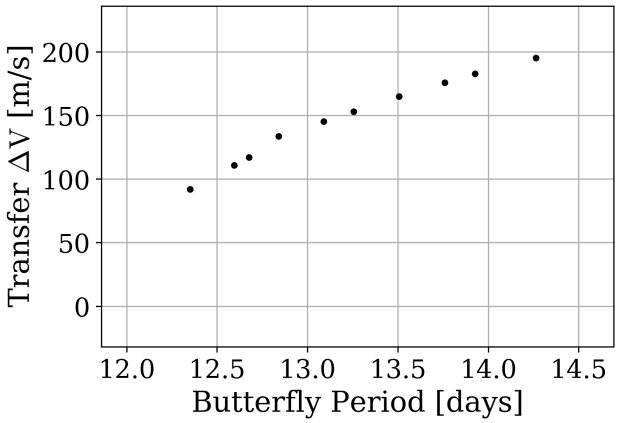

Figure 6.10. Maneuver costs for two-arc return transfers.

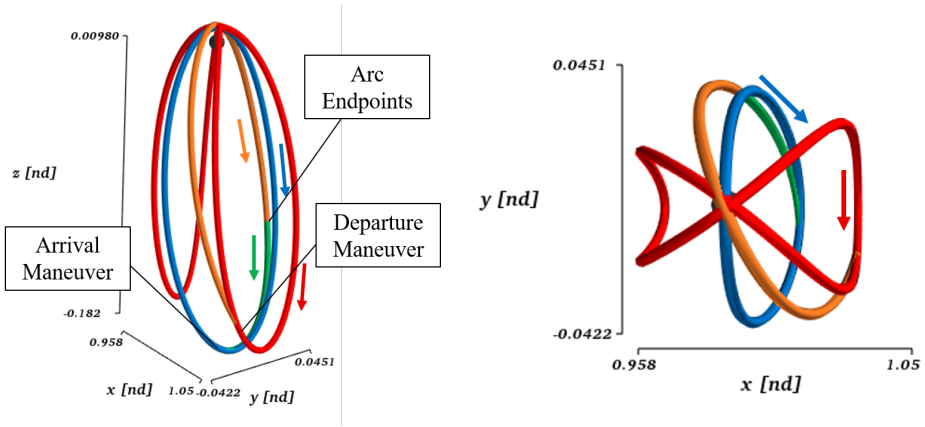

(a) (b) View along $-z$ axis

Figure 6.11. Example return transfer from a butterfly orbit (red) to the 9:2 NRHO (blue). The butterfly departure arc is colored in orange and the NRHO arrival arc is colored in green.

7. SUMMARY AND FUTURE WORK

7.1 Summary

The overarching goal of this work supports renewed interest in cislunar space; a sustained infrastructure in cislunar space is integral to NASA's vision in the coming years. The baseline orbit of this infrastructure is a Near Rectilinear Halo Orbit and one of the goals of the facility is to serve as a proving ground for deep space operations. As such, it is vital to understand the regions of space, and the types of destinations, available from an NRHO. One such destination of interest is the butterfly family of orbits—a family arising from a period-doubling bifurcation along the halo family. To that end, this work details the evolution of the butterfly family itself in the Earth-Moon system, as well as multi-body orbit design strategies linking the family with NRHOs. To begin, the Circular Restricted Three-Body Problem (CRTBP) is defined. All of the orbits in this investigation reside in the CRTBP. Various aspects supporting analysis in the CRTBP are discussed, including the rotating reference frame, nondimensionalization, equilibrium points, integrals of the motion, and zero-velocity surfaces. Next, concepts from differential corrections, which are vital to developing orbits and transfers in the CRTBP, are introduced. These concepts include the State Transition Matrix, targeters, and continuation schemes. Concepts from dynamical system theory are discussed: stability, invariant manifolds, Poincaré maps, and bifurcation theory. Such concepts serve as the basis of many of the initial transfer designs in this work and are integral to understanding the evolution of the butterfly family. By applying all of these concepts, the two primary objectives of this work are the characterization of the butterfly family and transfers linking the butterfly family to NRHOs.

The evolution of the butterfly family, in terms of its geometry, stability, and energy, is complex. The early evolution of the butterfly family results in orbits that are similar to the NRHOs with respect to stability. In this region, members of the family possess two distinct lobes, one on either side of the Moon. The period of such orbits are, thus, approximately double that of the corresponding NRHOs. As the butterfly family continues to evolve, it becomes more complex. The stability modes change such that the eigenvalues of the monodromy matrix become complex and leave the unit circle, corresponding to complex instability. The two distinct lobes also expand in size. As the family evolves, its eigenstructure undergoes numerous changes. The two distinct lobes gradually become four distinct lobes. Eventually, the family grows to encompass the entirety of the Earth-Moon system. The energy levels and periods of such members of the family becomes prohibitively large for useful transfers.

Various transfer methodologies are available to link the butterfly family to the NRHOs. Initially, transfers are designed to early members of the butterfly family—those that are similar to the NRHOs. Such transfers are designed in multiple fashions, including one-arc and two-arc transfers. Further, transfers are found that leverage dynamical structures, i.e., manifolds, to produce lower ΔV costs. These transfers have been demonstrated for multiple members of the family. Transfers leveraging these manifolds result in lower costs when compared to the one-arc and two-arc transfers, but the process requires greater computational and direct design effort.

7.2 Recommendations for Future Work

There are many potential areas for future study. First, as this work focused on feasible transfers, a more directed effort toward low-cost maneuvers can likely produce cheaper transfers than have been presented in this investigation. Further, transfers from the butterflies to other families of orbits in cislunar space would expand the possible destinations available to the planned cislunar facility. Similarly, this

investigation explored only one possible scenario of return transfers from butterflies to the NRHOs. Expanding this set of solutions, and finding alternative transfers, is desirable. Also of great importance is the transition from the CRTBP to the ephemeris model. Such an investigation is vital for understanding how butterfly orbits may be used in an operational sense, especially with regard to station-keeping and disposal. With respect to operational considerations, it would be worthwhile to characterize the butterfly family's eclipsing properties, especially since one of the benefits of NRHOs is their ability to avoid eclipses. Previous authors have studied Earth-to-butterfly and butterfly-to-lunar surface transfers for a small portion of the butterfly family; a similar investigation of transfers using a larger portion of the butterfly family would be beneficial for characterizing the family to a greater extent.

REFERENCES

[1] National Aeronautics and Space Administration. *NASA Strategic Plan 2018*. Technical report, NASA Headquarters, 2018.

[2] M. Raftery. ISS exploration platform concept, November 2011.

[3] W. Gerstenmaier and J. Crusan. *Cislunar and Gateway Overview*. Technical report, NASA Headquarters, September 2018.

[4] E. M. Zimovan, K. C. Howell, and D. C. Davis. Near rectilinear halo orbits and their application in cis-lunar space. In *Advances in the Astronautical Sciences*, volume 161, pages 209–228, Moscow, Russia, 2017. Univelt Inc.

[5] J. Williams, D. E. Lee, R. J. Whitley, K. A. Bokelmann, D. C. Davis, and C. F. Berry. Targeting cislunar near rectilinear halo orbits for human space exploration. In *Advances in the Astronautical Sciences*, volume 160, pages 3125–3144, San Antonio, TX, USA, 2017. Univelt Inc.

[6] R. Martinez and R. Whitley. Options for staging orbits in cis-lunar space. In *2016 IEEE Aerospace Conference*, Big Sky, MT, USA, 2016. IEEE.

[7] D. Grebow. Generating periodic orbits in the circular restricted three-body problem with applications to lunar south pole coverage. Master's thesis, Purdue University, West Lafayette, IN, USA, 2006.

[8] I. Newton. *The Principia: mathematical principles of natural philosophy*. Univ of California Press, 1999.

[9] L. Euler. *Theoria motuum lunae nova methodo pertractata*, volume 22. Springer Science & Business Media, 1772.

[10] J. Lagrange. Essai sur le probleme des trois corps. *Prix de lacadémie royale des Sciences de paris*, 9:292, 1772.

[11] C. G. J. Jacobi. Sur le mouvement dun point et sur un cas particulier du probleme des trois corps. *Compt. Rend*, 3:59–61, 1836.

[12] G. W. Hill. Researches in the lunar theory. *American journal of Mathematics*, 1(1):5–26, 1878.

[13] H. Poincaré. Sur le problème des trois corps et les équations de la dynamique. *Acta mathematica*, 13(1):A3–A270, 1890.

[14] V. Szebehely. Theory of orbits: the restricted problem of three bodies. Technical report, Yale univ New Haven CT, 1967.

[15] G. H. Darwin. Periodic orbits. *Acta mathematica*, 21(1):99–242, 1897.

[16] R. W. Farquhar. The control and use of libration-point satellites. Technical report, Stanford University, July 1968.

[17] J. V. Breakwell and J. V. Brown. The halofamily of 3-dimensional periodic orbits in the earth-moon restricted 3-body problem. *Celestial mechanics*, 20(4):389–404, 1979.

[18] K. C. Howell and J. V. Breakwell. Almost rectilinear halo orbits. *Celestial mechanics*, 32(1):29–52, 1984.

[19] E. M. Zimovan. Characteristics and design strategies for near rectilinear halo orbits within the earth-moon system. Master's thesis, Purdue University, West Lafayette, IN, USA, August 2017.

[20] L. Capdevila, D. Guzzetti, and K. C. Howell. Various transfer options from earth into distant retrograde orbits in the vicinity of the moon. In *AAS/AIAA Space Flight Mechanics Meeting*, volume 118, Santa Fe, NM, USA, 2014.

[21] D. C Davis, S. M. Phillips, K. C. Howell, S. Vutukuri, and B. P. McCarthy. Stationkeeping and transfer trajectory design for spacecraft in cislunar space. In *AAS/AIAA Astrodynamics Specialist Conference*, Stevenson, WA, USA, 2017.

[22] D. Guzzetti, E. M. Zimovan, K. C. Howell, and D. C. Davis. Stationkeeping analysis for spacecraft in lunar near rectilinear halo orbits. In *27th AAS/AIAA Space Flight Mechanics Meeting*, pages 1–20, San Antonio, TX, USA, 2017.

[23] R. J. Whitley, D. C. Davis, M. L. McGuire, L. M. Burke, B. P. McCarthy, R. J. Power, and K. C Howell. Earth-moon near rectilinear halo and butterfly orbits for lunar surface exploration. In *AAS/AIAA Astrodynamics Specialists Conference*, Snowbird, UT, USA, 2018.

[24] J. S. Parker. *Low-energy Ballistic Lunar Transfers*. Ph.D. dissertation, University of Colorado at Boulder, Boulder, CO, USA, 2007.

[25] J. S. Parker and G. H. Born. Modeling a low-energy ballistic lunar transfer using dynamical systems theory. *Journal of Spacecraft and Rockets*, 45(6):1269–1281, 2008.

[26] J. S. Parker. Monthly variations of low-energy ballistic transfers to lunar halo orbits. In *AIAA/AAS Astrodynamics Specialist Conference*, page 7963, 2010.

[27] K. K. Boudad. Disposal dynamics from the vicinity of near rectilinear halo orbits in the earth-moon-sun system. Master's thesis, Purdue University, West Lafayette, IN, USA, December 2018.

[28] K. K. Boudad, D. C. Davis, and K. C. Howell. Disposal trajectories from near rectilinear halo orbits. In *AAS/AIAA Astrodynamics Specialist Conference*, Snowbird, UT, USA, August 2018.

[29] D. C. Davis, K. K. Boudad, S. M. Phillips, and K. C. Howell. Disposal, deployment, and debris in near rectilinear halo orbits. In *29th AAS/AIAA Space Flight Mechanics Meeting*, Ka'anapali, Maui, HI, USA, January 2019.

[30] I. A. Robin and V. V. Markellos. Numerical determination of three-dimensional periodic orbits generated from vertical self-resonant satellite orbits. *Celestial Mechanics*, 21(4):395–434, 1980.

[31] D. J. Grebow, M. T. Ozimek, K. C. Howell, and D. C. Folta. Multibody orbit architectures for lunar south pole coverage. *Journal of Spacecraft and Rockets*, 45(2):344–358, 2008.

[32] E. T. Whittaker. A treatise on the analytical dynamics of particles and rigid bodies (cambridge up, cambridge, 1937). *Google Scholar H. Goldstein, Classical Mechanics*, 1937.

[33] J. Barrow-Green. *Poincaré and the Three Body Problem*, volume 11 of *History of Mathematics*. American Mathematical Soc., 1997.

[34] A. D. Cox. Transfers to a gravitational saddle point: An extended mission design option for lisa pathfinder. Master's thesis, Purdue University, West Lafayette, IN, USA, May 2016.

[35] A. E. Roy and M. W. Ovenden. On the occurrence of commensurable mean motions in the solar system: the mirror theorem. *Monthly Notices of the Royal Astronomical Society*, 115(3):296–309, 1955.

[36] V. A. IAkubovich and V. M. Starzhinskiĭ. *Linear differential equations with periodic coefficients*, volume 2. Wiley, 1975.

[37] R. Broucke. Stability of periodic orbits in the elliptic, restricted three-body problem. *AIAA journal*, 7(6):1003–1009, 1969.

[38] D. J. Grebow. *Trajectory design in the Earth-Moon system and lunar South Pole coverage*. Ph.D. dissertation, Purdue University, West Lafayette, IN, USA, 2010.

[39] E. T. Campbell. *Bifurcations from families of periodic solutions in the circular restricted problem with application to trajectory design.* Ph.D. dissertation, Purdue University, West Lafayette, IN, USA, August 1999.

[40] B. F. Villac and D. J. Scheeres. Escaping trajectories in the hill three-body problem and applications. *Journal of Guidance, Control, and Dynamics*, 26(2):224–232, 2003.

[41] A. F. Haapala. Trajectory design using periapse maps and invariant manifolds. Master's thesis, Purdue University, West Lafayette, IN, USA, 2010.

[42] D. E. Craig-Davis. *Multi-body trajectory design strategies based on periapsis Poincaré maps*. Ph.D. dissertation, Purdue University, West Lafayette, IN, USA, 2011.

[43] A. F. Haapala and K. C. Howell. Representations of higher-dimensional poincaré maps with applications to spacecraft trajectory design. *Acta Astronautica*, 96:23–41, 2014.

[44] M. E. Paskowitz and D. J. Scheeres. Robust capture and transfer trajectories for planetary satellite orbiters. *Journal of guidance, control, and dynamics*, 29(2):342–353, 2006.

[45] J. Guckenheimer and P. Holmes. *Nonlinear Oscillations, Dynamical Systems, and Bifurcations of Vector Fields*. Applied Mathematical Sciences, 42. Springer New York : Imprint: Springer, 1983.

[46] K. C. Howell. Families of orbits in the vicinity of the collinear libration points. In *AIAA/AAS Astrodynamics Specialist Conference and Exhibit*, page 4465, Boston, MA, USA, 1998.

[47] Z. P. Olikara. Computation of quasi-periodic tori. Master's thesis, Purdue University, West Lafayette, IN, USA, 2010.

[48] B. P. McCarthy. Characterization of quasi-periodic orbits for applications in the sun-earth and earth-moon systems. Master's thesis, Purdue University, West Lafayette, IN, USA, 2019.

[49] A. Jorba and J. Masdemont. Dynamics in the center manifold of the collinear points of the restricted three body problem. *Physica D: Nonlinear Phenomena*, 132(1-2):189–213, 1999.

[50] K. C. Howell and H. J. Pernicka. Numerical determination of lissajous trajectories in the restricted three-body problem. *Celestial Mechanics*, 41(1-4):107–124, 1987.

[51] E. Kolemen, N. J. Kasdin, and P. Gurfil. Multiple poincaré sections method for finding the quasiperiodic orbits of the restricted three body problem. *Celestial Mechanics and Dynamical Astronomy*, 112(1):47–74, 2012.

[52] F. Schilder, H. M. Osinga, and W. Vogt. Continuation of quasi-periodic invariant tori. *SIAM Journal on Applied Dynamical Systems*, 4(3):459–488, 2005.

[53] Z. P. Olikara and D. J. Scheeres. Numerical method for computing quasi-periodic orbits and their stability in the restricted three-body problem. *Advances in the Astronautical Sciences*, 145(911-930), 2012.